

Dedicated to:

My lovely grandad, Derek Mason, sadly passed away this year before seeing the completion of this work. My grandad singlehandedly inspired my love for understanding the mysteries and absurdities of the universe. He spent countless hours nurturing all of my interests and making me the person I am today. I'm forever grateful for having such an inspirational and kind man as my grandad.

Also dedicated to my parents, Clare and Harry, girlfriend Tasha and wider family.

Acknowledgements:

Dr. Bahramy has encouraged my interdisciplinary interest in both Physics and Artificial Intelligence, with many fantastic discussions and advice in developing this work.

Several teachers, at Highfields School Matlock, particularly fostered and developed my curiosity in mathematics and physics including Mr. J. R. Edney, Mr. D. Moss, Mr. Hammond, Mr. M. Flett, among many others.

Developing a Robust Material Classification Dataset for Application to Machine Learning

George Bird george.bird@student.manchester.ac.uk

Supervisor: Dr. Mohammad Saeed Bahramy

*Department of Physics and Astronomy
University of Manchester*

November 2022

Abstract

In this project, a large dataset is generated with the intention of training machine learning models to replicate its mappings. The crystal Bismuth-Tellurium-Iodide was selected as it exhibits a wide range of emergent quantum phenomena, including topologically non-trivial states, under specific deformations. Furthermore, the categorisation of these phenomena can be determined analytically. Therefore, this dataset enables systematic comparisons of quantum and classical machine learning techniques to modelling condensed matter systems. Techniques proven using this dataset can then be applied to an expanded set of crystals to streamline research in material development.

To develop this dataset required efficient and robust methods of classifying Bismuth-Tellurium-Iodide states such that many samples can be generated. To achieve this required novel implementation of condensed matter models which can be computed in parallel using GPU-acceleration to generate many samples. Furthermore, we used a novel application of the gradient descent algorithm to determine key features in the material's dispersion relations which aid in this classification process. Several methods of enlarging the dataset are also presented, such that the machine learning approach can better model the system. The condensed matter models and assumptions used to develop the procedures are derived and discussed, alongside the characteristic behaviours of several topologically trivial and non-trivial material states. The resultant classification procedures are shown to be successful and offer insight into the studied materials.

Contents

1	Introduction: Quantum Mechanical Analysis of Crystals	3
1.1	Many-body Schrödinger Equation	3
1.2	Crystal Lattices	3
1.3	Bloch Wavefunctions	4
1.4	Condensed Matter Models and Assumptions	4
1.4.1	Born-Oppenheimer Approximation	4
1.4.2	Linear Combination of Atomic Orbitals	5
1.4.3	Nth Nearest Neighbour Cutoff Assumption	5
1.4.4	Tight-Binding Model	6
2	Classification of Materials	6
2.1	Classical Materials	7
2.1.1	Conductors	7
2.1.2	(Trivial) Insulators	7
2.1.3	Semiconductors	7
2.1.4	(Weyl & Dirac) Semimetals	8
2.2	Overview of Topology and its Connection to Material Classification	9
2.3	Topological Insulators	9
2.3.1	Rashba Effect	10
3	Methodology and Results of Classifying Topological States for Application to Machine Learning	11
3.1	Novel Approach to Highly Parallelised Tight-Binding Equation Solvers	12
3.2	Material Classification Procedure	14
3.2.1	Determining Minimum Bandgap by Grid Search and Random Sampling	14
3.2.2	Gradient descent - A Novel Approach for Determining the Bandgap Minima	15
3.3	Dataset Expansion	16
3.3.1	Interpolation	16
3.3.2	Random Noise	16
3.4	Energy Eigenvalue Analysis	18
3.5	Eigenvector Analysis and Spin Behaviour	19
3.6	Analysis of Spin-Orbit Terms	23
4	Conclusion	23
4.1	Outlook of Work	24
4.1.1	Benchmarking Supervised Learning Models	24
4.1.2	Quantum Machine Learning Approach	24
4.1.3	Generalising for Many Crystalline Materials	24

1 Introduction: Quantum Mechanical Analysis of Crystals

1.1 Many-body Schrödinger Equation

Arguably the single most insightful and defining equation of modern physics is the Schrödinger equation, shown in its time-dependent form in *Eqn. 1*. It describes the nature, evolution and interaction of waves defining matter. The equation follows from the Hamiltonian approach to classical mechanics, where classical terms are replaced with quantum operators. There are a multitude of cases for which the Schrödinger equation can be solved analytically, such as atomic orbitals.

$$\hat{H}\Psi(\vec{x}, t) = \frac{-\hbar^2}{2m} \nabla^2 \Psi(\vec{x}, t) + V(\vec{x}, t) \Psi(\vec{x}, t) = -i\hbar \frac{\partial}{\partial t} \Psi(\vec{x}, t) \quad (1)$$

However, analytical solutions of the schrödinger equation become intractable in many-body scenarios, due to the growing number of pair-wise interactions [1]. The many nuclei and electron interactions involved in macroscopic materials make their analytical analysis prohibitive to compute. This is demonstrated in *Eqn. 2* where the pairwise-interactions needing consideration grows quadratically with the number of particles, alongside a linear growth in the dimension of the hilbert space. Thus, several simplifying assumptions have been developed to yield insight. Particularly the tight-binding equation is utilised in this project, as it captures the quantum behaviour of interest whilst having reasonable computational cost. Therefore, this model, its associated assumptions and prerequisite models are outlined in this introduction.

$$\hat{H} = \underbrace{\sum_{i=0}^{N_{\text{nuc.}}} \frac{-\hbar^2}{2m_i} \nabla_i^2}_{\text{Nuclei Kinetic Term}} + \underbrace{\sum_{j=0}^{N_{\text{elec.}}} \frac{-\hbar^2}{2m_j} \nabla_j^2}_{\text{Electron Kinetic Term}} + \underbrace{\sum_{k=0}^{N_{\text{nuc.}}} \sum_{l=0}^{k-1} \frac{Z_k Z_l e^2}{4\pi\epsilon_0 |\vec{x}_k - \vec{x}_l|}}_{\text{Nuclei-Nuclei Interaction}} + \underbrace{\sum_{p=0}^{N_{\text{nuc.}}} \sum_{q=0}^{N_{\text{elec.}}} \frac{-Z_p e^2}{4\pi\epsilon_0 |\vec{x}_p - \vec{x}_q|}}_{\text{Nuclei-Electron Interaction}} + \underbrace{\sum_{m=0}^{N_{\text{elec.}}} \sum_{n=0}^{m-1} \frac{e^2}{4\pi\epsilon_0 |\vec{x}_m - \vec{x}_n|}}_{\text{Electron-Electron Interaction}} \quad (2)$$

These streamlined models have shown quantum mechanics to be an effective descriptor for many of the characteristics of bulk materials [2]. A variety of material classifications can be understood through the resultant quantum dispersion relations, detailed in *Sec. 2.1*. Moreover, some materials classifications are realised uniquely through this approach, including topological insulators which are emergent quantum phenomena. The identification of these emergent materials form the basis of this project. To begin analysing material properties requires a schema to represent the materials of interest, this is discussed in the following section.

1.2 Crystal Lattices

The most elementary material is a perfect crystal, without impurities or defects, as any additional disorder adds complexity. These crystalline materials are described through the tessellation of a base object, a unit cell, depicted in *Fig. 1*. Unit-cells are characterised by their constituent atoms and their relative positions. These cells are offset by integer multiples of lattice-vectors described in *Eqn. 3*. This formulation of the unit-cell and its associated lattice-vectors is the minimal, complete description for these materials.

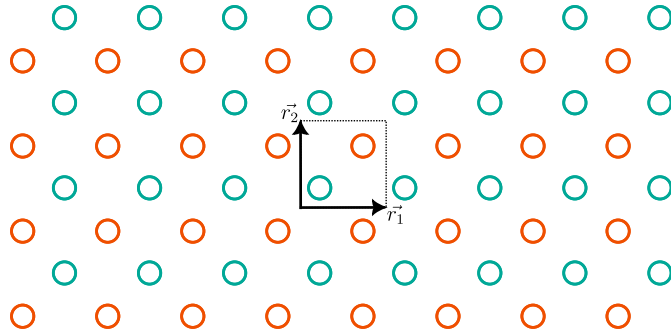


Figure 1: Depicts how a unit cell, outlined with a dashed box and containing two atoms of orange and blue type, is tiled by integer multiples of the lattice vectors \vec{a}_1 and \vec{a}_2 to produce the crystal.

$$\vec{R} = \sum_{i=0}^m n_i \vec{r}_i \quad (3)$$

Where $n_i \in \mathbb{Z}$ giving each of the integer factors for the offsets, and $\vec{r}_i \in \mathbb{R}^m$ are each of the lattice vectors. These vectors should be assumed to be mutually independent and span an m dimensional space. It is further assumed that the crystal is infinite in extent or abides by some periodic boundary condition.

As a consequence of tessellation, perfect crystalline materials feature at least discrete translational symmetry. If electron-electron interactions are also neglected, which would otherwise develop the problem into a many-body dynamic with its associated complexity, then a periodic potential arises that incurs constraints on the wavefunction. Thus, the wavefunction must also exhibit the same discrete translational symmetry which is described by the Bloch-theorem.

1.3 Bloch Wavefunctions

The coordinate system's origin can be arbitrarily shifted by the vector in *Eqn. 3*. Consequently, the local environment experienced by the electron is independent of which cell is defined as the centre. Therefore, it is expected that observable properties of the wavefunction vary within the unit cell, but repeat with the same discrete translations, resulting in periodic observable properties of the wavefunction. Complex, global phase of the wavefunction is unobservable, so it can evolve through the crystal without being constrained by the symmetry. This leads to the Bloch wavefunction [3] shown in *Eqn. 4*.

$$\Psi(\vec{x}) = e^{i\vec{k} \cdot \vec{x}} u(\vec{x}) \cap u(\vec{x} + \vec{R}) = u(\vec{x}) \quad (4)$$

The function $u(\vec{x})$ results from the specific periodic potential involved, modulating the plane-wave solution. A position dependent phase, characterised by the quantum number \vec{k} , enters through the plane-wave term. This parameter can be associated to the crystal-momentum, in analogy to the standard plane wave [4]. Thus Bloch's theorem indicates that electrons are distributed as modulated waves, with various crystal momenta, within the crystalline material.

1.4 Condensed Matter Models and Assumptions

As mentioned, a range of simplifying assumptions to the many-body Schrödinger description are employed to make it computationally feasible to model wavefunctions within a material. The aim is to capture all the dynamics of interest, contributing to the emergent material properties, whilst jettisoning any redundant information. This reduction in the degrees of freedom results in a smaller search-space for solutions and hence a quantum description becomes computationally attainable. A broad range of techniques have been developed to express different emergent features of a material. In this work the tight-binding model is extensively used. A general progression of models up to the tight-binding model, alongside contributing assumptions, are detailed below.

1.4.1 Born-Oppenheimer Approximation

A large relative mass difference between the nuclei and electron makes it practical to model their dynamics separately, since their time-evolution's occur at vastly differing rates, as seen in *Eqn. 1*. This separable approach is known as the Born-Oppenheimer approximation [5] and it has wide application in physics and chemistry. In *Eqn. 5*, the many-body Schrödinger equation is separated into a nuclear and electronic hamiltonian, which act on their respective separated wavefunctions.

$$\hat{H}\Psi(\{\vec{r}_i\}, \{\vec{r}_j\}) \approx (\hat{H}_{\text{nucl}} + \hat{H}_{\text{elec}}) \psi(\{\vec{r}_i\}) \phi(\{\vec{r}_j\}) \approx \hat{H}_{\text{nucl}}\psi(\{\vec{r}_i\}) + \hat{H}_{\text{elec}}\phi(\{\vec{r}_j\}) \quad (5)$$

The semi-independent modelling of both these systems has given insight into material behaviour. For example, the displacement of the nuclei from their equilibrium position describes the mechanism of both heat [6] and sound transmittance [7, 8] throughout a crystalline solid. These quantised vibrational modes give rise to the phonon quasiparticle, a type of emergent boson that can distribute energy throughout the crystal [9]. Due to a large time-scale difference between the two, it is typical to neglect the nuclei wavefunction entirely in an extension to the Born-Oppenheimer approximation. This is

an appropriate measure to uphold the crystal's discrete translational symmetry. In addition, it is often the general time-independent electronic states which are of interest, so only time-averaged nuclear wavefunctions are sufficient to provide solutions.

However, this simplification can lead to deficits in a material's electronic description. Despite the differing time-scales for motion, the separated systems have been shown to have important interplay producing emergent quantum behaviour [10–12]. A further composite boson quasiparticle, the cooper pair [13], can arise from many electron-phonon interactions within a crystal. The condensation of these bound states has been demonstrated to be an effective description for superconductivity [14]. Thus, some emergent phenomena cannot be modelled from analysis of the electronic system alone.

However, with just the extended Born-Oppenheimer approximation, the degrees of freedom representing the electronic system remain in excess of what is needed to explain many of the observed material properties. With just this assumption the modelling remains inviable. The transition away from the position basis to describe wavefunctions, reduces the number of degrees of freedom. In the following section the linear combination of atomic orbitals is used to approximately represent the wavefunction, further simplifying the many-body dynamics.

1.4.2 Linear Combination of Atomic Orbitals

Interactions between electrons and neighbouring nuclei tend to zero as the nuclei are infinitely separated. This results in the electronic wavefunctions tending towards their independent atomic wavefunction solutions. At finite separation these atomic wavefunctions are increasingly perturbed. However, if this process is considered insignificant, the resultant crystal wavefunction can be represented using a linear combination of these atomic orbitals [15]. This assumption offers a greatly simplified, approximate basis for solving the wavefunctions of a crystal lattice. This superposition of atomic orbitals, to describe the electron wavefunction, is shown in *Eqn. 6*.

$$\Psi_n(\vec{x}) = \sum_{\vec{R}} \sum_a C_{n,a,\vec{R}} \psi_a(\vec{x} - \vec{R}) \quad (6)$$

Individual normalised atomic orbitals are given by ψ_a centred on each of their respective nuclei. These orbitals can also include electron spin to account for the pauli-exclusion principle [16]. Each of these orbitals are then displaced by vector \vec{R} , producing the full extent of the crystal. The resultant electron wavefunction Ψ should also be normalised to one. Therefore, *Eqn. 6* can be used to describe the single electron wavefunction in a crystal. The many-body schrödinger equation in the position basis can be represented in the atomic basis, for a single electron, as shown in *Eqn. 7*. Thus, the hamiltonian is represented as a matrix, enabling the matrix-mechanics approach. Where i and j go through all atomic orbital permutations from *Eqn. 6*. This equation can interpreted as a stochastic matrix for continuous-time, discrete-space markovian dynamics.

$$\hat{H}_{ij\vec{R}} = \langle \psi_i | \hat{H} | \psi_j \rangle = \int d\vec{x} \psi_i^*(\vec{x}) \hat{H}(\vec{x}) \psi_j(\vec{x} - \vec{R}) \quad (7)$$

The elements can be determine using Hartree-Fock method [17, 18] or density-functional theory [19]. These techniques address the electron-electron interaction terms using an electron mean-field, this decouples the individual electron in the Hamiltonian allowing each nuclei and electron equation to be approximated separately. Finally, the energy eigenvalues and mixing coefficients $C_{a,\vec{R}} \in \mathbb{C}$ are deduced such that they fulfill the time-independent schrödinger relation $\hat{H}\Psi_n \approx E_n\Psi_n$.

It is apparent from this description that when superposing the wavefunctions, the corresponding energy eigenvalues can combine to form a wider range of energies than the original quantised ones from the atomic orbitals. This begins a trend of quasi-continuous energy bands for large crystals. To ascertain better understanding of crystal properties, a dependence between the energy value and crystal-momenta must be found. To achieve this requires the Tight-Binding equation and a truncation to the atomic orbitals being considered.

1.4.3 Nth Nearest Neighbour Cutoff Assumption

For a given infinitely extending crystal, a finite number of \vec{R} are sampled. These are chosen in order of proximity ($|\vec{R}|$). It is expected that long-range interactions become negligible. Thus, a cutoff number is chosen for how many neighbouring cells

are evaluated. The distance cutoff used depends on the crystal being studied. The term "nth-next nearest neighbours" is used to describe an equidistant set of cells from the central cell.

1.4.4 Tight-Binding Model

The Tight-Binding model [20] can be interpreted as the application of Bloch-wavefunctions to the linear combination of atomic orbitals (LCAO), using the Born-Oppenheimer and N^{th} nearest neighbour cutoff assumptions. The term tight-binding arises from the atomic orbital basis used, as tightly bound electrons will have minimally perturbed atomic orbitals as described in the LCAO technique. The tight-binding technique can be viewed as a further simplification to LCAO method, by utilising the discrete translational symmetry to relate displaced atomic orbitals through the Bloch-theorem.

In *Eqn. 7*, each of the diagonal terms ($i = j \cap \vec{R} = \vec{0}$) represents the energy eigenvalues for the atomic orbitals, which take on their usual discrete values. Meanwhile all other terms represent the likelihood of an electron hopping from one orbital to another. These hopping terms represent the bond-energies between neighbouring orbitals. Now orbitals displaced by \vec{R} must be related using *Eqn. 4*. This requires a contraction of $H_{ij\vec{R}}$ with the phase acquired from the Bloch theorem ($\phi_{\vec{R}} = e^{i\vec{k}\cdot\vec{R}}$). The resultant expression is shown in *Eqn 8*.

$$\hat{H}(\vec{k}) = \hat{H}_{ij}(\vec{k}) = \sum_{\forall \vec{R}} e^{i\vec{k}\cdot\vec{R}} \hat{H}_{ij\vec{R}} \quad (8)$$

This hamiltonian is trivially Hermitian if the n-nearest neighbour approach is used for sampling \vec{R} . Using the time-independent schrödinger equation, shown in *Eqn. 1*, it can be seen that the energy-band structure is related to the crystal-momenta. This relation is demonstrated in *Eqn. 9*.

$$\hat{H}(\vec{k}) \Psi_{n\vec{k}} = E_n(\vec{k}) \Psi_{n\vec{k}} \quad (9)$$

Where $\Psi_{n\vec{k}}$ represents a vector of mixing coefficients for the various atomic orbitals. These coefficients, similar to those in *Eqn. 6*, and energy eigenvalues can be found by diagonalisation of the hamiltonian H_{ij} . These represent stationary states for the electrons in the crystal, so called "Bloch-electrons" characterised by the crystal momenta \vec{k} describing their phase evolution through the crystal. In addition, for each wavevector \vec{k} , the Bloch-electron can also exist in several excited states, indicated by the several energy eigenvalues, these correspond to various complex hybridisations of the atomic orbitals. Since the energy is a function of the crystal momenta, and multiple excited states exist for each momenta, then continuous energy bands form. A direct consequence of the periodicity in position, a discrete translational symmetry is also exhibited in the wavevectors \vec{k} , seen in the phase factor of *Eqn. 8*, this results in the "reciprocal lattice". Reciprocal-lattice vectors (\vec{G}) characterises this discrete translational symmetry as demonstrated in *Eqn. 10*.

$$e^{2\pi i \vec{G} \cdot \vec{R}} = 1 \quad (10)$$

The individual vectors b_j are combined to make $\vec{G} = \sum_{j=0}^m p_j \vec{b}_j$ where $p_j \in \mathbb{Z}$, analogous to *Eqn. 3*. These are related by $\vec{r}_i \cdot \vec{b}_j = 2\pi\delta_{ij}$. Thus, the full electron dynamics, up to the given assumptions, are summarised in a finite region called the Brillouin zone [21]. This Brillouin zone is tiled by the reciprocal lattice vectors to make the full \vec{k} -space. As the Tight-binding equation is a bijective map, there is a unique correspondence between the unit-cell for the real space crystal being studied and the Brillouin-zone's energy-momentum relations. Consequently, all arrangements of crystals have unique Brillouin zones and therefore unique energy band structures and orbital hybridisations. Since these characterise material properties, it is clear that every type of crystal has unique behaviours. However, these material properties can be classified under general categories, discussed in the next section.

2 Classification of Materials

Using the energy band structure, it is possible to group many materials into distinct categories based on their overall electronic behaviour. Historically, many of these general classifications existed prior to discovery of the energy band structure for

electrons and instead relied upon experimental observations. However, the electronic band structure was found to effectively describe the various material properties [2] and offered a rigorous criteria to classify them. In addition, it created a theoretical framework to discover more exotic emergent quantum properties within the preexisting classifications leading to further subdivisions being defined.

2.1 Classical Materials

For any given material, the constituent atoms will possess a specific number of electrons. At absolute zero, these electrons occupy the wavefunctions corresponding to the minimum possible energy for the material. This leads to a distinct cutoff, known as the fermi-energy (E_f), where available states above this energy value are unoccupied and states below are fully occupied. At temperatures higher than absolute zero, thermal fluctuations can excite a number of electrons into higher energy states, through phonon-electron interactions. These excited electrons tend to originate from around the fermi-energy since less energy is needed to excite them. After excitation, unoccupied states can remain which may act as quasiparticles, for example a "hole" quasiparticle has analogous properties to a positron [22, 23]. The allowed excitations of electrons and properties of any resultant quasiparticles directly influence material properties and are determined by the energy-momentum defined by the band structure. In the following sections a brief overview is given on how to classify common materials from their band structure.

2.1.1 Conductors

In conductors the fermi-energy lies within the continuous energy-band. As a consequence, electrons at the fermi-energy have no threshold of energy required to excite them and this leads to a mix of occupied and unoccupied states around the fermi-energy. As a result, due to the presence of many unoccupied states, electrons can easily redistribute even under the application of weaker electric fields. This can incur a bias in which crystal-momenta states are occupied and this leads to a net total momenta of the electrons. Consequently, electric current is easily produced under an applied electric field, characterising conductors.

In addition, the gradient of the band structure is proportional to the group velocity of the Bloch-electrons as shown in *Eqn. 11*. This group-velocity indicates the transport properties of electrons which affects electrical conductivity (σ). So, if the fermi-energy lies in a steep region of the energy-momenta relation the electrical conductivity of the material is greater.

$$\vec{v} = \hbar^{-1} \nabla_{\vec{k}} E(\vec{k}) \quad (11)$$

2.1.2 (Trivial) Insulators

Insulators have their fermi-energy outside the energy-band. In this case, the fermi-energy lies in a region absent of allowed energy states, known as an "energy bandgap". As a result a substantial threshold energy is required to excite an electron. This results in the electrons occupying all available groundstate, filling the energy bands below the fermi-energy. Hence, insulators are poor at conducting electricity as very large electric fields are required to setup a net momentum bias. Dielectric breakdown gives an indication of how large this electric field must be to make the material conductive.

2.1.3 Semiconductors

Semiconductors can be interpreted as the middle ground between conductors and insulators. Like insulators, the fermi-energy is situated within a bandgap but this bandgap is substantially smaller. Thus a threshold energy exists, but is not insurmountable at room-temperatures, resulting in some electrical conductivity. Defining semiconductors explicitly from their bandgap can be somewhat arbitrary depending on the degree of splitting in the energy bands. Therefore, semiconductors can instead be characterised by the ability to dope the material with impurities, altering the fermi-energy.

The doping of semiconductors is one of the greatest applications of condensed matter physics, enabling the wide variety of electronics [24]. Introducing impurities controls conductivity by either increases the number of unoccupied states below the fermi-energy (p-type) or increases the number of electrons (n-type).

Unlike conductors, the group-velocity is smaller in the fermi-energy region due to flatter band structure. This results in poorer conductivity of semiconductors. However, the energy-bands close to the fermi-energy are also approximately parabolic. Consequently, the energy-momentum relation is similar to that of classical massive particles, though it can be anisotropic, as shown in *Eqn. 12*. C is a constant added to reach the top or bottom of the band.

$$E_{\text{total}}(\vec{k}) = C + \sum_i \frac{\hbar^2 k_i^2}{2m_i} \quad (12)$$

Extending this principle outside of semiconductors, it can be found that many band structures, near the fermi-energy, are better approximated using the relativistic energy [25–27] shown in *Eqn. 13*, with fitting constants M and the fermi-velocity v_{F_i} . This indicates that the electrons and holes can travel through the crystal in a way analogous to relativistic particles.

$$E_{\text{total}}(\vec{k}) = \pm \sqrt{M^2 + \hbar^2 \sum_i v_{F_i}^2 k_i^2} \quad (13)$$

In the next section, some semimetals are shown to have band structures which approximate the dispersion relation of ultra-relativistic particles.

2.1.4 (Weyl & Dirac) Semimetals

Semimetals occur when the energy bandgap closes and the respective bands may begin to overlap at the fermi-energy [28]. This can be used as a classification criteria if a material's bandgap reduces to zero under deformation. Semimetals are conductive since there is no energy-threshold for excitation. Furthermore, both the electrons and quasiparticles are responsible for their conductive properties. Particularly, weyl-semimetals and dirac-semimetals [29] are sub-classifications which we will focus on in this description, since these semimetal states arise in our crystal of study: Bismuth-Tellurium-Iodide (BiTeI).

These semimetals are characterised by a linear dispersion relation about the fermi-energy, appearing as dirac-cones [25, 30] in the Brillouin zone. As a consequence, quasiparticles emerge which can be described by the dirac equation, shown in *Eqn. 14*. The energy dispersion of these solutions corresponds to *Eqn. 13* where M is the quasiparticle's rest energy. However, these quasiparticles are massless if dirac-cones are present in the Brillouin zone. Specifically, at least two possible solutions are exhibited which define the distinction between dirac-semimetals and weyl-semimetals.

$$(i\hbar\gamma^\mu\partial_\mu - m_{\text{eff}}v_D)\Psi(x) = 0 \quad (14)$$

Dirac-semimetals require time-reversal (shown in *Eqn. 15*) and spatial-inversion (shown in *Eqn. 16*) symmetry to be upheld in the crystal. As a consequence of this, the spin-up and spin-down states are degenerate. Thus, any crossing of previously distinct bands, defining a semimetal state, actually includes the crossing of four bands due to the spin-degeneracy. Therefore, the quasiparticles which form are massless dirac fermions.

$$\hat{T}\Psi_{\vec{k},\uparrow} = \Psi_{-\vec{k},\downarrow} = \Psi_{\vec{k},\uparrow} \quad (15)$$

$$\hat{I}\Psi_{\vec{k},\uparrow(\downarrow)} = \Psi_{-\vec{k},\uparrow(\downarrow)} = \Psi_{\vec{k},\uparrow(\downarrow)} \quad (16)$$

Weyl-semimetals occur when either of these symmetries are broken. Spatial-inversion symmetry is broken via spin-orbit interactions, such as the Rashba effect discussed in *Sec. 2.3.1*, resulting in non-degenerate spin states. The presence of spin-orbit interaction is used as a method of distinguishing the semimetal states of BiTeI and is discussed further in *Sec. 3.6*. Due to the splitting of the spin states, the previous dirac-cone involving four band crossings, divides into two weyl-cones with just two band crossings at each. The respective weyl-cones are crossings of exclusively spin-up or spin-down bands. Consequently, emergent quasiparticles are formed known as weyl-monopoles which are a previously unobserved solution to the Dirac equation [31–33]. These pairs of monopoles and antimonopoles can only be created and annihilated along specific symmetry lines of the crystal, thus are protected states and migrate through the crystal symmetrically according to time-reversal symmetry. The monopoles carry the resultant charge from a local $U(1)$ gauge invariance of the quantum state [34, 35]

shown in *Eqn.* 17, where $|u(\vec{k})\rangle$ is described in *Eqn.* 4.

$$|u'(\vec{k})\rangle = e^{i\phi(\vec{k})} |u(\vec{k})\rangle \quad (17)$$

Since this is a $U(1)$ gauge symmetry, a vector potential can be defined as shown in *Eqn.* 18.

$$\vec{A}(\vec{k}) = -i\langle u(\vec{k}) | \nabla_{\vec{k}} | u(\vec{k}) \rangle \quad (18)$$

The curl ($\vec{B}(\vec{k}) = \nabla \times \vec{A}(\vec{k})$), known as berry connection can be integrated across a closed surface to produce the geometric phase [36], also known as the berry phase [37]. This has an associated charge, shown in *Eqn.* 19, which is the charge of the monopoles.

$$\varrho(\vec{k}) = \frac{\nabla_{\vec{k}} \cdot \vec{B}(\vec{k})}{2\pi} = \sum_i q_i \delta(\vec{k} - \vec{k}_i) \quad (19)$$

Where $q_i = \pm 1$, whilst $\delta(\vec{k})$ represents the dirac-delta function. These dirac delta functions are centred on the band crossing points [38] (\vec{k}_i) as expected. These weyl-monopoles have either left-handed ($q_i = -1$) or right-handed ($q_i = +1$) chiralities, dependent on the weyl-cone being considered [39]. These weyl-monopoles are more stable, as they do not rely on the symmetries involved in the dirac-semimetals. Due to the spin-orbit splitting, the opposite chiral-charge monopoles are separated in momentum-space by the position of the weyl-cones but join to form characteristic fermi-arcs at the surface [40–42]. These weyl-monopoles are effective charge carriers behaving as massless, ultra-relativistic and therefore highly mobile particles. These can find applications requiring faster conduction in electronics, have many applications in spintronics and can also elucidate the nature of the Higgs mechanism [43]. Weyl-semimetals are considered topologically non-trivial [44] and this premise of analysing materials topologically allows for new classifications of distinct material states. These states exhibit unique, emergent quantum phenomena which will have important and widespread technological applications.

2.2 Overview of Topology and its Connection to Material Classification

Topology is the study of general classifications of shapes, which can be homeomorphically deformed into one another. Groups of homeomorphic shapes are characterised by constant topological numbers including genus, orientability and torsion. In recent years, there has been a paradigm shift to use classifications developed in topology and apply it to categorising condensed matter systems. Whereas the energy band structure is usually indicative of a material's classifications, topological insulators are instead distinguished through topological numbers [45–47]

The \mathbb{Z}_2 topological invariant can be applied to condensed matter systems with topological numbers ν_i . These represent the number of Kramer pairs [35, 48], which are pairs of degenerate energy states which are the time-reversed states of one another. The possible values of ν_i are 0 (trivial) or 1 (topological), therefore a smooth transition between these integers is not possible, resulting in distinct topological categorisations. There are four topological numbers associated with \mathbb{Z}_2 , namely $\nu_0; (\nu_1, \nu_2, \nu_3)$. Where ν_0 is the strong topological index which is resistant to impurities, specially non-magnetic impurities as magnetic fields break the time-reversal symmetry. Whilst $\nu_{1,2,3}$ are the weak topological indices and are not resilient nor significant in impure crystals.

The \mathbb{Z}_2 topological invariants cannot be changed when a bandgap exists [38]. Consequently, they can be used to further subdivide the previous states using topological categorisation. These topologically non-trivial states arise in insulators, producing topological-insulators with unique properties alongside the aforementioned weyl semimetals. The following section will overview this emergent quantum material classification.

2.3 Topological Insulators

Topological insulators are a further sub-classification of insulating materials. Despite displaying similar behaviours to trivial insulators, such as no conductivity in their bulk due to a bandgap, they are distinctly different with at least one non-zero \mathbb{Z}_2 topological number. Therefore, it is not possible to adiabatically transform, analogous to topology's homeomorphic transform, from a trivial to a topological insulator without first closing the bandgap to change the topological index.

The presence of the aforementioned monopoles and antimonopoles prevent the opening of such a bandgap, permitting the topological invariant to change. Subsequently, a semimetallic state [49] is formed between the transition of a trivial insulator to a topological insulator. This separates the two insulating states in phase space, indicating their distinctness. Therefore, the general category of insulating states can be further subdivided. These new categorisations are a result of topological analysis of condensed matter systems.

During the intermediate semimetal stage a rearrangement of the orbital and spin coefficients occur resulting in the topological insulator being a conglomerate of the previously dissimilar bands when the bandgap is formed again. This is known as band inversion [29] and represents one mode of classifying the insulating types, discussed further in *Sec. 3.5*.

At the surface of the material a transition must also occur from a topological to trivial insulator. This is because the vacuum is a trivial insulator, since there exists a bandgap of the minimum energy for particle pair-production. Hence, between the bulk of the topological insulator and the vacuum, the bandgap must close. A resultant semimetal-like gapless state, with linear dispersion, must form. This results in all topological insulators having a conducting surface, with highly mobile and spin-locked electrons, which are topologically protected under deformation. These electrons are also not easily scattered by impurities [50]. These features of topological insulators have a wealth of applications such as in pulsed laser technology [51], spintronics [52] and topological Qubits with greater stability [52,53].

In this project BiTeI is studied as it exhibits the topological insulator state under specific applied hydrostatic pressures. This crystal hosts these emergent quantum phenomena due to a broken spatial-inversion symmetry caused by spin-orbit coupling resulting from the Rashba effect [54].

2.3.1 Rashba Effect

Many crystals exhibit the time-reversal symmetry, shown in *Eqn. 15*, and spatial-inversion symmetry, shown in *Eqn. 16*. The time-reversal symmetry states that the wavefunction does not change under application of the time-reversal operator (\hat{T}) which flips the spin state and reverses the momentum direction, equivalent to a time-reversal in the evolution of the system. In addition, the spatial-inversion symmetry represents an invariance to the system when mirrored, this is described by the inversion operator (\hat{I}) and crystals with this property are labelled as centrosymmetric.

When these two transformations are composed together it is evident that the system must be spin-degenerate, as shown in *Eqn. 20*. Since, both operators commute with the Hamiltonian, they also commute with one another.

$$\hat{I}\hat{T}\Psi_{\vec{k},\uparrow(\downarrow)} = \Psi_{\vec{k},\downarrow(\uparrow)} = \Psi_{\vec{k},\uparrow(\downarrow)} \quad (20)$$

Topological insulators utilise spin-orbit interactions to produce the necessary band inversion characterising them [55]. Typically, this can be achieved by breaking time-reversal symmetry, using an external magnetic field. A resultant spin-degenerate minimum band-gap at $\vec{k} = 0$ is produced forming a topological insulator [56]. Both the Rashba effect and topological insulators involve significant spin-orbit interactions, which indicates that the Rashba effect offers alternative means for generating topological materials through breaking of spatial-inversion symmetry. These different forms of symmetry broken band structures are illustrated in *Fig. 2*.

This mode of producing a topological insulator is realised in the BiTeI crystal [54,57] used in this project. This crystal under sufficient hydrostatic pressure, exhibits the topological insulator state with topological indices $\mathbb{Z}_2 : \nu_0; (\nu_1, \nu_2, \nu_3) = 1; (0, 0, 1)$ as opposed to the trivial insulator state with $\mathbb{Z}_2 : 0; (0, 0, 0)$ [54].

The Rashba effect occurs in BiTeI crystals as Tellurium and Bismuth are heavy ions which produce a strong spin-orbit coupling, leading to band inversion without an external magnetic field. As a consequence, electron spins are no longer degenerate in the Brillouin zone leading to spin-splitting. The Rashba effect is included through a term added to the Hamiltonian shown in *Eqn. 21*. It can be seen that this effect is both spin and momentum dependent, through the pauli matrices σ_i and momentum operator \vec{p} respectively.

$$H \propto (\vec{\sigma} \times \vec{p}) \cdot \hat{z} = \alpha (\sigma_x p_y - \sigma_y p_x) \quad (21)$$

Uniquely, the Rashba effect in BiTeI leads to several energy bandgap minima, away from the centre of the Brillouin zone. Usually, in centrosymmetric crystals, the bandgap reaches a minimum at the central high-symmetry point. However, in BiTeI

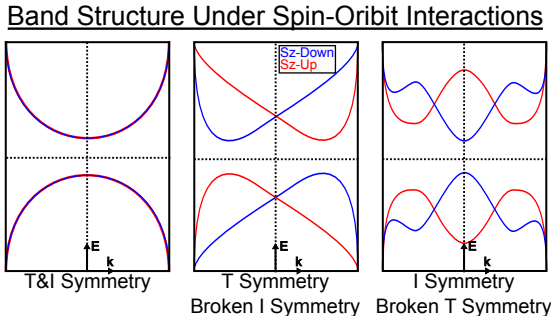


Figure 2: This is a pictorial representation of energy band structure under combinations of the time-reversal (T) and spatial-inversion (I) symmetries. The spin-states are coloured as blue for spin-down and red for spin-up. It is apparent, in the left diagram, that if both symmetries are present, the crystal is spin-degenerate. Whilst the central crystal represents a non-centrosymmetric crystal such as BiTeI with spin splitting due to a Rashba effect. The rightmost diagram indicates systems with broken time-reversal symmetry imposed by an external magnetic field.

six minima form in the direction of the A-L symmetry line [58], for the topological insulator state, and six minima along the A-H symmetry line for the trivial insulating state. Due to these multiple off-centre bandgap minima, novel properties and applications may be possible for BiTeI, including further spintronic applications [57, 59].

Furthermore, the Rashba effect results in BiTeI becoming a weyl semimetal under lesser pressure due to the spin splitting. However, since the band-crossing points occur away from the symmetry point A , this poses a problem for identifying the \vec{k}_i position of the crossing. These crossings are the positions of the monopoles and antimonopoles, as previously discussed. Under time-reversal symmetry the berry curvature is odd, $\vec{B}(\vec{k}) = -\vec{B}(-\vec{k})$ and therefore the monopoles and antimonopoles are distributed symmetrically about the origin: $\varrho(\vec{k}) = -\varrho(-\vec{k})$ [38]. After creation on A-H symmetry line, they dissociate and recombine symmetrically towards the A-L symmetry line. In the following sections, methods to identify these bandgap closing points through both grid-search and a novel application of gradient descent are described.

3 Methodology and Results of Classifying Topological States for Application to Machine Learning

The possible arrangements for crystals is near infinite, so there likely exists many undiscovered crystalline materials with desirable behaviours allowing for novel technologies. Material development and classification is a time consuming process requiring extensive experimental tests. Due to the vast number of candidate materials to be trialled, it is impractical to naively probe for useful materials without a method of refining the search space to fewer, more promising candidates for experimental verification. Machine learning, and more specifically artificial neural networks, has already been shown to be an effective tool is analogous regimes such as drug discovery [60–64]. The principle is that learned associations from a known subset of crystals can be developed and then applied to the remaining space. Therefore, it is likely that a machine learning approach can suitably, and efficiently, predict the properties of theoretical crystals [65]. As a result, the process of material development would be streamlined. With sufficiently accurate modelling, it may even be possible to specify desirable properties and develop a matching crystal structure from the specification. This is amble motivation to apply similar techniques to condensed matter systems.

This work aims to systematically prove the machine learning approach of modelling condensed matter systems. Particularly, prospective models must be verified against well-studied analytical systems before applying them to the wider unknown search space. Therefore, in this project, we curate a large analytical dataset for properties of Bismuth-Tellurium-Iodide crystals, specifically the classifications of material states, under various deformations to the crystal. Notably, BiTeI crystals exhibits a variety of such states, including the weyl semimetal and topological insulator emergent quantum states. Due to presence of these uniquely quantum mechanical phenomena, this dataset serves as the optimum platform to compare quantum machine learning against classical machine learning techniques in modelling condensed matter systems. As only quantum machine learning may be positioned to appropriately model these systems because of the shared quantum behaviour.

This dataset should consist of atomic orbital hopping coefficients for BiTeI, described in *Eqn. 7*, paired with their resultant material classification, such that a classification neural network can learn mapping relations between the two. This requires a sufficiently large dataset, due to the complicated system dynamics, so that the network can learn good approximate relations. The dataset can be expanded through crystal deformations, discussed in *Sec. 3.3*. Deformations to the crystal manifest in changes in the value of such hopping coefficients and this may result in a change of state. The quality of the trained neural network is limited by the accuracy of the dataset. Therefore, it is desirable to minimise any assumptions to produce a robust dataset which will not impede network generality. The following procedures are performed on every sample in the training dataset. Hence, it is imperative that efficient and accurate classification algorithms are implemented. The development of such methods is the central aim of this project. In the following sections, the algorithms developed to classify materials are motivated, discussed and implemented.

3.1 Novel Approach to Highly Parallelised Tight-Binding Equation Solvers

As discussed, in this project we will be using the tight-binding equation to model the BiTeI condensed matter system to develop an analytic dataset. The initial information provided is the hopping coefficients between neighbouring atomic orbitals, generated using density-functional-theory (DFT). Two samples of these hopping coefficients are provided, one when the BiTeI is known to be in a trivial insulating state and one when it is in a topological insulating state. These represent the crystal at two different hydrostatic pressures [54] and it is expected that these are separated by a weyl semimetal, and maybe also a dirac semimetal state. Therefore, classification of the four involved states is desired.

The DFT algorithm produces hopping coefficients for the electron originating in an atomic orbital, in the central unit cell, and transitioning to itself or other neighbouring atomic orbitals for all cells up to a cutoff distance. Hence, it is assumed that long-range interactions offer negligible corrections to the electronic band structure. Specifically, for BiTeI the cutoff is defined such that 1155 cells, closest to the central unit cell, are considered.

Within each cell the P_x , P_y and P_z orbitals for Bismuth ($6P$), Tellurium ($5P$) and Iodide ($5P$) significantly contribute so are considered alongside the electron's 2-component spin. This results in 18 atomic orbitals for every combination. Therefore, the electron can originate in one of 18 initial orbitals and jump to one of 18 final state orbitals, yielding a total of 324 permutations per cell. Further, considering the 1155 neighbouring cells produces 374420 complex hopping coefficients contributing to the electronic band structure.

Using *Eqn. 3*, the vector $\vec{a} \in \mathbb{Z}^3$ takes values $\alpha \equiv a_x \in [-6, 6]$, $\beta \equiv a_y \in [-5, 5]$, $\gamma \equiv a_z \in [-5, 5]$ in the DFT calculation, representing each neighbouring cell's displacement from the central cell at $\vec{a} = \vec{0}$. Not all these combinations of \vec{a} exist due to the neighbour cutoff. Furthermore, $P_i \in ([0, 18] \cap \mathbb{Z})$ and $P_f \in ([0, 18] \cap \mathbb{Z})$ denote the initial state and final state atomic orbital, where the orbitals are enumerated as shown in *Tab. 1*. Finally, for every permutation there is a complex-valued hopping term. These parameters can act as indices for an array representation of the hopping coefficients ($T \in \mathbb{C}^{6 \times 5 \times 5 \times 18 \times 18}$ and indexed $T_{a_1, a_2, a_3, P_i, P_j}$) with unknown hopping coefficients set to 0. Using an array structure enables repurposing of array-optimised machine learning libraries.

0 Te- $P_{x\uparrow}$	1 Te- $P_{y\uparrow}$	2 Te- $P_{z\uparrow}$	3 Bi- $P_{x\uparrow}$	4 Bi- $P_{y\uparrow}$	5 Bi- $P_{z\uparrow}$	6 I- $P_{x\uparrow}$	7 I- $P_{y\uparrow}$	8 I- $P_{z\uparrow}$
9 Te- $P_{x\downarrow}$	10 Te- $P_{y\downarrow}$	11 Te- $P_{z\downarrow}$	12 Bi- $P_{x\downarrow}$	13 Bi- $P_{y\downarrow}$	14 Bi- $P_{z\downarrow}$	15 I- $P_{x\downarrow}$	16 I- $P_{y\downarrow}$	17 I- $P_{z\downarrow}$

Table 1: Orbital Enumeration

Using this, various means of computing the tight-binding equation, shown in *Eqn. 8*, can be implemented. Although Python, considered as a slow computing language, is used in the project, it is merely for the accessing the front-end of the PyTorch library which utilises the graphics processing unit (GPU) for optimisation. Consequently, the following approach is executed in back-end CUDA code ran on the GPU. This allows very fast computation of array operations. Thus, we leverage this to compute the energy band structure in an efficient and novel manner.

Due to the array being discretised and unable to store functions, it is not possible to generate a closed form solution for the band structure at continuous crystal momentum values. Therefore, in the initial formulation of this procedure, the band

structure is sampled at a single value for \vec{k} . This is a direct implementation of *Eqn.* 8, where singular value decomposition is used to determine the n eigenvalues (E_n) and eigenvectors (ψ_i^n) for the resultant 2D hamiltonian. The energy eigenvalues are then sorted in increasing order ($E_0 \leq E_1 \dots \leq E_n$), for each value of \vec{k} . This produces a sampling of the desired energy band structure and dispersion relations. Moreover, the Einstein summation convention [66] can be used to directly specify efficient array operations to be executed on a GPU. Therefore, for convenience of implementation, the convention will be used in all following algebra. This is demonstrated in *Eqn.* 22 describing this implementation of the tight-binding equation.

$$\hat{H}_{ij}\psi_{nj} = (e^{ia_{\alpha\beta\gamma l}r_{lm}k_m} T_{\alpha\beta\gamma ij}) \psi_{nj} = E_n \psi_{ni} \quad (22)$$

Where r_{ij} is the array of lattice vectors stacked row-wise and $a_{\alpha\beta\gamma l}$ is an array lookup of considered cell offsets, such that $a_{\alpha\beta\gamma} = (\alpha, \beta, \gamma)$. The full singular value decomposition of the hamiltonian into the energy eigenvalues and eigenvectors is shown in *Eqn.* 23, where δ_{ij} is the kronecker delta.

$$(e^{ia_{\alpha\beta\gamma l}r_{lm}k_m} T_{\alpha\beta\gamma ij} - E_n \delta_{ij}) \psi_{nj} = 0_{ni} \quad (23)$$

Furthermore, it was essential to make this calculation fully differentiable to enable a novel technique of locating bandgap minima in the Brillouin zone, discussed further in *Sec. 3.2.2*. The jacobian representing the derivative of the tight binding equation is shown in *Eqn.* 24 and is also proportional to the direction dependent group velocity of *Eqn.* 11.

$$\frac{\partial E_n}{\partial k_\varrho} = ia_{\alpha\beta\gamma l} r_{l\varrho} e^{ia_{\alpha\beta\gamma l} r_{l\varrho} k_\varrho} \psi_{ni}^* T_{\alpha\beta\gamma ij} \psi_{nj} \quad (24)$$

Despite the GPU optimisation, this method remains relatively slow as the computation needs to be calculated sequentially for small interval sampling of \vec{k} to appropriately resolve the continuous behaviour of the band structure. This sequential processing is an inefficient use of the large number of GPU cores. If sufficient video-RAM is accessible, then this process should be parallelised in \vec{k} . The implementation of multiple parallel computations of the tight binding model made up a significant proportion of this project. The parallelisation of *Eqn.* 22 in \vec{k} is shown in *Eqn.* 25. Where p discrete samples of the Brillouin zone are stacked row-wise to form the matrix k_{pm} . Thus, the tight-binding equation can be calculated for a large number of \vec{k} samples at once, by exploiting the GPU optimisation of array operations, making this method exceedingly efficient.

$$E_{pn}\psi_{pni} = e^{ia_{\alpha\beta\gamma l}r_{lm}k_{pm}} T_{\alpha\beta\gamma ij} \psi_{pnj} \quad (25)$$

Finally, it is intended that multiple hamiltonians will be evaluated to show the various material classifications which BiTeI can exhibit. If an adiabatic transformation is performed between the two DFT datasets, then a large set of hamiltonians will be generated. In a similar way to how the discrete \vec{k} samples were computed in parallel, this procedure can be repeated for the various hamiltonians stacked in their first index: q hamiltonians ($T_{\alpha\beta\gamma ij}$) produce a six-dimensional array ($T_{q\alpha\beta\gamma ij}$). However, to make each hamiltonian independent under gradient descent update by $\partial E_n / \partial k_{pm}$ requires the array k_{pm} to be tiled q times producing k_{qpm} . This leads to the final einstein summation expression for a highly-parallelised approach to computing the tight-binding equation, as shown in *Eqn.* 26.

$$E_{qpn}\psi_{qpn} = e^{ia_{\alpha\beta\gamma l}r_{lm}k_{qpm}} T_{q\alpha\beta\gamma ij} \psi_{qpnj} \quad (26)$$

The respective derivative for this equation is required for later gradient analysis of the energy band structure. This derivative is shown in *Eqn.* 27 and represents the local evaluation of electronic band structures gradients.

$$\frac{\partial E_{qpn}}{\partial k_{sh\varrho}} = i(\delta_{qs}\delta_{ph})(a_{\alpha\beta\gamma l}r_{l\varrho}) (\psi_{qpn}^* T_{q\alpha\beta\gamma ij} \psi_{qpnj}) e^{ia_{\alpha\beta\gamma l}r_{l\varrho}k_{qpe}} \quad (27)$$

The independence of the hamiltonians and discrete \vec{k} samples is shown through the two kronecker deltas in *Eqn.* 27.

Overall, this approach effectively leverages GPU acceleration by computing the desired tight-binding equations in parallel. This novel technique offers a large improvement in computation time compared to similar approaches. However, it is limited

by the video-RAM capacity, since all the arrays must be loaded into the memory. Yet with new, purpose-built GPU's for machine learning, this constraint is not a impediment to the method. The implementation of this technique was shared with our group, to allow the efficient calculation of the required tight-binding results. This work made up a substantial backbone for further calculations in the project. An example of the BiTeI band structure produced using this technique is shown in *Fig. 3*.

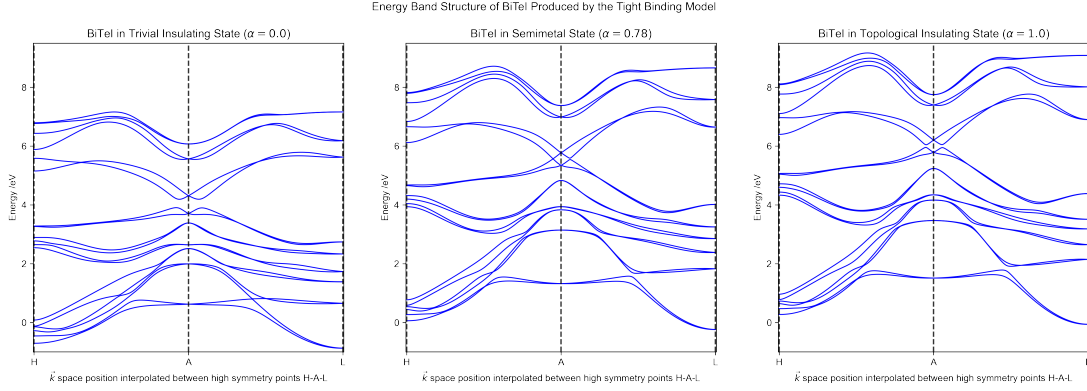


Figure 3: The energy band structures for BiTeI in three different states are shown, generated using the tight-binding equation. Left to right are the trivial insulating, semimetal and topological insulating states respectively, all evaluated along the H-A-L symmetry lines [58]. As expected 18 continuous bands are formed.

3.2 Material Classification Procedure

Using the parallel tight-binding equation solver, the nature of the Brillouin zone can now be determined for specific values of \vec{k} . With this, the various hamiltonians can be categorised into disjoint sets for trivial insulators, topological insulators and semimetals states of BiTeI. To distinguish between insulating and semimetallic states requires determination of the minimum bandgap between the valence and conduction bands. The fermi-energy level for BiTeI lies between the 12th and 13th bands, making these the valence and conduction bands respectively.

Therefore, the location corresponding to their closest approach (\vec{k}_{\min}), in the Brillouin zone, is desired to separate the two states. Further splitting of trivial and topological insulating states can also be achieved through the associated eigenvectors at this minima. The details of this classification procedure are outlined in *Secs. 3.4* and *3.5*. In either case, the determination of the bandgap minima is required. Grid-search is a common technique [67,68] to determine parameters such a \vec{k}_{\min} , however we also present a novel application of the gradient descent algorithm to determine the bandgap minima.

3.2.1 Determining Minimum Bandgap by Grid Search and Random Sampling

Grid search can be described as a brute-force search technique for determining the Brillouin zone position of the minimum bandgap energy (\vec{k}_{\min}) between the valence and conduction bands. It involves discretising the Brillouin zone up to a specified resolution, then applying the tight-binding equation at each \vec{k} value to determine the 12th and 13th energy eigenvalues. These are then subtracted from one another, shown in *Eqn. 28*, and the position of the minima is determined to be the value of \vec{k} corresponding to the smallest value of E_{BG} . For higher precision on \vec{k}_{\min} , a further sampling can be performed on a subspace surrounding the previously found minima. Though this makes the technique vulnerable to anomalous local minima. An analogous procedure can be used with a point cloud, of randomly sampled \vec{k} values within the Brillouin zone.

$$E_{BG}(\vec{k}) = E_{13}(\vec{k}) - E_{12}(\vec{k}) \quad (28)$$

Using the parallelised tight-binding equation, this method is reasonably efficient due to bulk computation of \vec{k} samples. However, the number of \vec{k} samples grows cubically with increased resolution. If repeated sequential sampling is performed, then on order of one hundred samples must be computed for each order-of-magnitude improvement in precise. It is preferable

to minimise any sequential computation performed in determining the minima for efficiency. Instead an application of the gradient descent algorithm, in finding \vec{k}_{\min} , is expected to have faster and more accurate convergence.

3.2.2 Gradient descent - A Novel Approach for Determining the Bandgap Minima

Gradient descent has proved to be an extraordinarily effective technique for parameter optimisation [69, 70]. This technique is an improvement over grid search, especially in higher dimensional parameter-spaces. It requires less initial \vec{k} samples to converge on more accurate minima, in fewer sequential steps. In addition, it has a variety of variations in its procedure for different applications. For example, the ADAM optimiser [71] is utilised in this project for even faster convergence when the position of minima are unknown. The elementary form of gradient descent consists of the parameter update shown in *Eqn. 29* for a given cost-function C . Where η is a small value known as the learning rate. Since all prior calculations are differentiable the gradients, such as from *Eqn. 27*, are easily implemented into *Eqn. 29*.

$$\vec{k}' = \vec{k} - \eta \nabla_{\vec{k}} C \quad (29)$$

The energy bandgap itself can be directly minimised. However, it is known that a linear dispersion relation of the bands is probable near the minima, leading to poor convergence due to equal update magnitudes. Thus, the bandgap energy is squared to ensure the desired convergence by an increasingly smaller update near the minima, as shown in *Eqn. 30*. Furthermore, it is commonplace to use stochastic gradient descent to optimise a mapping. However, this is undesirable when minimising an input parameter such as \vec{k} as it leads to the updates being, incorrectly, inversely scaled by the number of \vec{k} samples.

$$k'_{sh\varrho} = k_{sh\varrho} - \eta \frac{\partial (E_{sh(n=13)} - E_{sh(n=12)})^2}{\partial k_{sh\varrho}} \quad (30)$$

Local minima are a concern when using gradient descent, since parameters can converge on incorrect \vec{k} values. The overall risk of this is minimised by using the ADAM optimiser, since it utilises a momentum term in the algorithm. In addition, by using multiple \vec{k} samples and taking the minima of these, the likelihood of a local minima being found is reduced. Moreover, since the energy band-structure is the sum of finite hopping contributions we expect it to be reasonably smooth, containing finite minima as opposed to infinite fractal minima which would disrupt the technique.

Consequently, the novel application of gradient descent has been a resounding success in our project, enabling fast determination of bandgap minima in order to classify materials, as shown in *Fig. 4*. It has been implemented using PyTorch, alongside the discussed tight-binding approach, and used in the production and analysis of all our results.

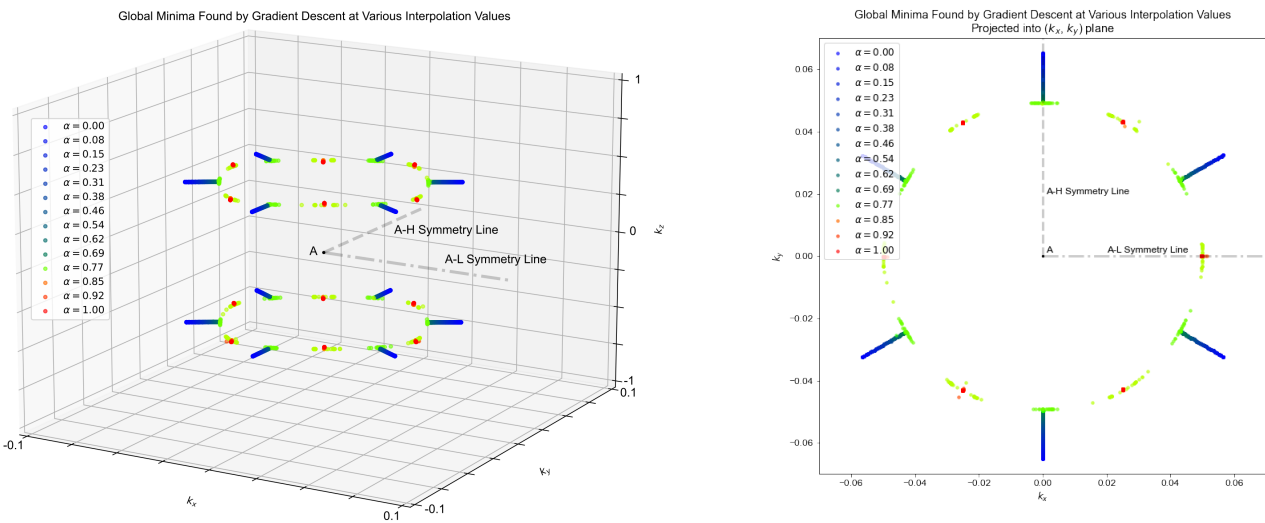


Figure 4: Plotted are the global minima found using the gradient descent procedure, at various values of the interpolation parameter α discussed in *Sec. 3.3.1*. Left shows the minima as a 3D plot, showing all global minima, whilst right shows these projected into the k_x and k_y plane. The colour corresponds to the value of α as shown in the key.

Multiple global minima are expected in the Brillouin zone for BiTeI due to the absence of spatial-inversion symmetry. Therefore, several distribution options are useful when initialising \vec{k}_{qpm} . For most data collection, a uniform random distribution across the entire Brillouin zone is desirable as it leads to better estimates of the location of the minimum energy bandgap and a larger learning rate can be used. This is the preferred method when the location of the minima is unknown. However, for later spin behaviour analysis, it is favourable to initialise all \vec{k}_{qpm} at a single point with a small learning rate. This is to encourage convergence onto specific global minima within a twelfth of the Brillouin zone. The smaller learning rate also confines the \vec{k} distribution better. Initialising \vec{k}_{qpm} in this manner allows the evolution of spin behaviour for a specific minima to be observed when varying the interpolation value. If the solutions are not confined to this region, then large shifts in spin components are observed due to spin splitting by the Rashba effect. This latter procedure was used to locate the minimas for *Fig. 11*. Checks should be done to ensure the resultant distribution of the global minima is known and ruled out as a source of drastic eigenvector changes.

3.3 Dataset Expansion

Training a neural network to model the given condensed matter system requires an extensive dataset, such that it can learn to relate the input information to the desired output. Neural networks typically learn relations better when producing a strongly abstractive map. We define abstraction as any map which lowers the intrinsic dimension of data, whilst transformative and generative¹ describe maps which keep constant or increase the intrinsic dimension respectively. The intrinsic dimension is a measure of the minimal degrees of freedom needed to span the embedded data, whilst the extrinsic dimension is the dimension of the embedding space. The dataset, so far, includes BiTeI at two different pressures corresponding to a trivial insulating state and a topological insulating state. This is insufficient to train an effective neural network, therefore the dataset should be expanded to improve the resultant model's generality.

3.3.1 Interpolation

One method to expand the dataset is linear interpolation between the two known sets of hopping parameters. This is equivalent to varying the hydrostatic pressure between the two samples and is required to produce examples of the weyl semimetal state in the dataset. This procedure is shown in *Eqn. 31* and characterised by a mixing parameter $\alpha \in (\mathbb{R} \cap [0, 1])$.

$$T'(\alpha) = T^{\text{Trivial}}(1 - \alpha) + T^{\text{Topological}}\alpha \quad (31)$$

The resultant hopping coefficients (T') can be used to generate new samples for the dataset. Furthermore, since the hamiltonians cannot be adiabatically transformed from a trivial insulating state to a topological insulating state without first crossing a semimetal state, then we would expect two critical values for α . The first is the boundary between the trivial insulator and the semimetal state, representing the monopole-antimonopole creation point, whilst the second critical value is their destruction on the semimetal to topological insulator transition. A linear dependence between the minimum bandgap energy and interpolation parameter is expected in each of the insulating states. Using samples of α a linear regression can be performed, for values in each insulating state, to find the critical values of α which are the root of each respective fit.

The dataset generated via interpolation produces a sampling of a 1D continuous manifold of input data. We categorise this into a disjoint set of 4 possible elements: trivial insulators, topological insulators, weyl semimetal and dirac semimetal. This represents 4, 0-dimensional points which can be connected using a minimum of a 1D manifold. Therefore, the network is only provided a reformative map to ascertain relations from, which is sub-optimal. Therefore, a further technique is required to expand the dataset.

3.3.2 Random Noise

Generating samples perturbed by random noise will increase the input's intrinsic dimension, depicted in *Fig. 5*. This will provide more varied samples to reduce network overfitting [72] and consequently improve the model's generality. These perturbed hamiltonians are also labelled using the same procedure as the interpolated samples. Therefore, it is not assumed

¹Due to insufficient input degrees of freedom, such a dataset requires the network to be a multi-valued function which is not possible. However, the network can still approximate this process by folding discretely sampled manifolds so that they appear to have increased in intrinsic dimension.

that a consistent classification is upheld in a localised region around a previously classified sample. This is especially important when considering any discontinuous phase change. Since a neural network is limited by the quality of the dataset, the lack of such assumptions should improve the modelling.

However, unconstrained noise can result in unphysical hamiltonians. In addition, excessive network parameters would be required to model these cases. Therefore, two forms of constrained hermitian perturbations can be produced: spatial-inversion symmetric and time-reversal symmetric. These represent a variety of deformations to, or external fields applied, to BiTeI.

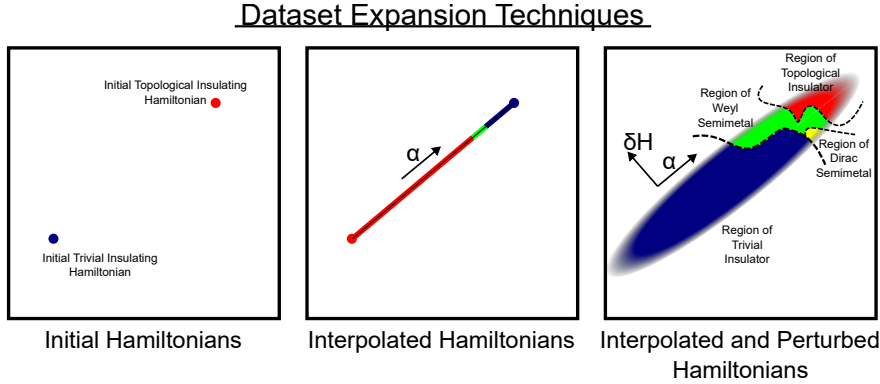


Figure 5: This illustration depicts a 2D slice of the possible hamiltonian space. Left shows the initial dataset with just two samples, thus two 0-dimensional points embedded in the space. Centre shows how the dataset can be expanded by interpolating between the initial hamiltonians, producing a sampling of a 1D continuous manifold embedded in the space. Right shows how the dataset is then further expanded using constrained perturbations producing a much higher dimensional manifold. The colours depict the disjoint material classifications and the dashed lines indicate the boundaries between these.

Spatial-inversion symmetric perturbations can be generated using the condition shown in *Eqn. 32*.

$$\delta H_I(\vec{k}) = \hat{P}(\delta H_I(-\vec{k})) \hat{P}^{-1} \quad (32)$$

Where \hat{P} is defined by $u(\vec{k}) = \hat{P}u(-\vec{k})$, from *Eqn. 4*. This corresponds to a diagonal matrix operator with elements ± 1 . In addition, time-reversal perturbations must abide by the condition shown in *Eqn. 33* [34].

$$\delta H_T(\vec{k}) = \hat{\sigma}_y (\delta H_T(\vec{k}))^T \hat{\sigma}_y \quad (33)$$

Where δH is the perturbation to the hamiltonian in the representation shown in *Eqn. 34*.

$$\delta H(\vec{k}) = \begin{pmatrix} \delta H_{\uparrow\uparrow}(\vec{k}) & \delta H_{\uparrow\downarrow}(\vec{k}) \\ \delta H_{\downarrow\uparrow}(\vec{k}) & \delta H_{\downarrow\downarrow}(\vec{k}) \end{pmatrix} \quad (34)$$

Uniform, random matrices can be drawn from distributions respecting these symmetries and then normalised. These random perturbations can be scaled and added elementwise to an interpolated hamiltonian before classification. This procedure suitably expands the dataset to have a very high intrinsic dimension, improving the neural network's performance. However, it has been shown [34] that adding inversion-symmetric perturbations changes the interpolation critical values, this is depicted in *Fig. 6*.

As a consequence, the material transitions cannot be identified using critical values of the interpolation parameter, found by aforementioned linear regression of the minimum energy bandgap. Further, generalising this to a hyperplane fit would not suitably account for a non-linear boundary and any further fitting would be needlessly contrived and overfitted. Therefore, a more robust procedure is required to generalise to the classification of randomly perturbed hamiltonians. This is achieved using a simpler approach of analysing the energy bandgap.

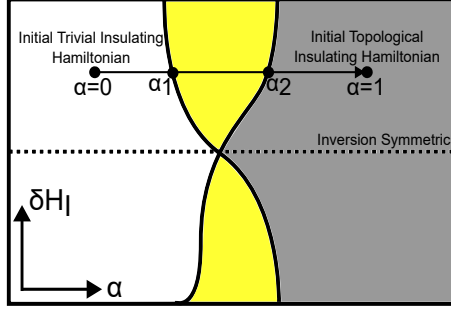


Figure 6: This diagram [34, 38] illustrates how the addition of spatial-inversion asymmetric noise alters the critical values for the interpolation parameter α . In the spatial-inversion symmetric case, it can be seen that there is a single critical value, whereas inversion-asymmetric case there are two. White shading indicates a trivial insulator, whilst grey and yellow indicate a topological insulator and semimetal states respectively. A line is drawn indicating the interpolation path between the two initial hamiltonians.

3.4 Energy Eigenvalue Analysis

By definition, the two forms of insulating states are expected to have a non-zero bulk energy bandgap between the valence and conduction bands, whilst the semimetal states are gapless. Due to this behaviour, the insulating and semimetal states are separable by measuring the minimum bandgap energy obtained using the procedure discussed in Sec. 3.2.2.

When applying increasing hydrostatic pressure, by increasing α from *Eqn. 31*, the BiTeI transitions from a trivial insulator to a semimetal, then to a topological insulator. Under this deformation the energy bandgap decreases whilst in the trivial insulating state, until the gap closes to form the gapless semimetal state at a critical value of α_1 . Since BiTeI is a non-centrosymmetric crystal, we would expect it to exist in this semimetal state for a finite range of α values, thus there exists an upper bound critical values of α_2 . This was directly observed in *Fig. 7*, with a linear fit finding values of $\alpha_1 = (0.784 \pm 0.001)$ and $\alpha_2 = (0.796 \pm 0.001)$.

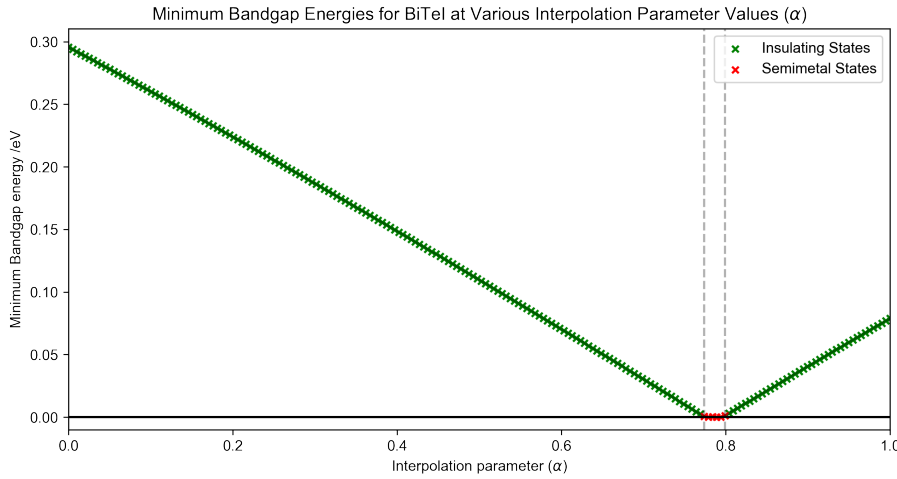


Figure 7: This shows the minimum energy bandgap ($E_{BG}(\vec{k}_0)$) between the valence and conduction bands of BiTeI at various interpolation parameter values. The samples classification as semimetals ($E_{BG}(\vec{k}_0) < \epsilon$) are shown in red whilst insulators ($E_{BG}(\vec{k}_0) \geq \epsilon$) are shown in green. The grey dashed lines indicate the critical values α_1 and α_2 .

Further hydrostatic pressure results in band inversion and the separation of the bands, producing a topological insulator. Since the tight-binding equation assumes an infinitely extending crystal, the gapless conductive boundary of this topological insulator will not be produced in the modelled band structure nor in the value of the minima, shown in *Fig. 7*. Consequently, it is possible to define a threshold energy value which distinguishes the insulating states from gapless semimetal states. Due to the imprecision of estimating the, often single point, bandgap minima alongside any floating point errors, the determined minima may sometimes be small but non-zero for the semimetal state. Therefore, a threshold value of $\epsilon = 2\text{meV}$ is used.

This procedure produces classifications for general insulating and semimetallic states. However, due to the minimum bandgap energy being a surjective but non-injective function of the interpolation parameter, there is insufficient information to produce the further sub-classifications of the semimetallic and insulating states. To determine whether the insulating states are topological or trivial requires analysis of the associated eigenvectors.

3.5 Eigenvector Analysis and Spin Behaviour

The eigenvalues and eigenvectors provide a complete basis of the hamiltonian so should be sufficient for determining further classifications. Calculating the topological numbers associated with \mathbb{Z}_2 would be a robust way to categorise the different states although it is too slow computationally. Therefore an alternative procedure is required to efficiently generate a very large dataset. We use a cosine similarity measure of the band composition to achieve this. The transition from trivial to topological insulator is characterised by a band inversion, shown in *Fig. 8*. This process can only occur in the gapless semimetal state. Therefore, we would expect the eigenvectors, indicating the orbital hybridisation of the bands, to remain roughly constant and unique for each of the trivial and topological hamiltonians with small perturbations, shown in *Fig. 9*.

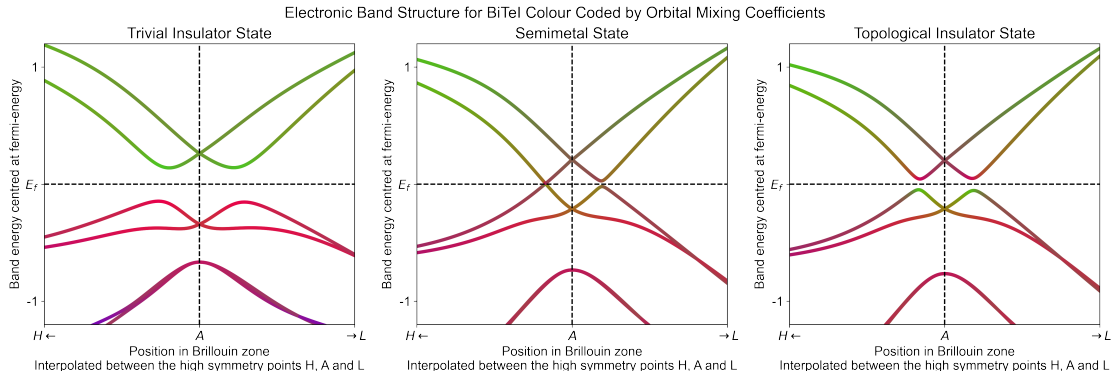


Figure 8: The valence and conduction band structure for BiTeI is shown along a section of the crystal symmetry lines H-A-L. The colours indicate the composition of each band in terms of the respective atomic orbitals, where red indicates Tellurium, green for Bismuth and blue for Iodide. The colour component represents the sum over all orbital angular momenta and spin configurations states. Left indicates the BiTeI crystal in its trivial insulating state, middle is the semimetal state and right is the topological insulator state. The band-inversion is clearly demonstrated by the mixing of the components in the semimetal and topological insulator state.

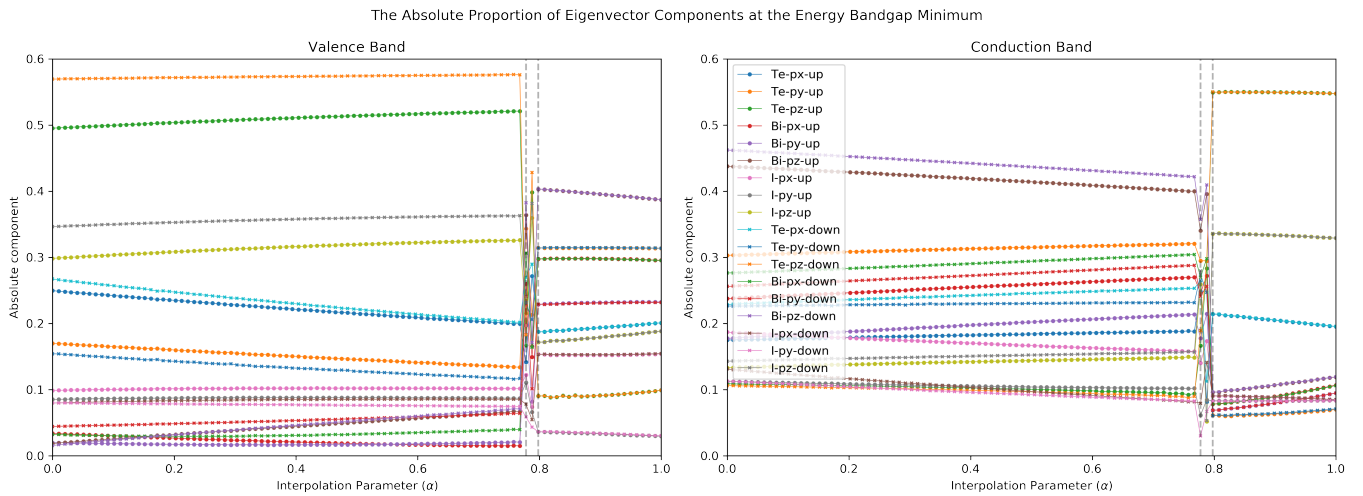


Figure 9: The absolute value of the eigenvector components is shown, taken at the energy bandgap minima for the valence band (left) and conduction band (right). It can be seen that band inversion occurs as expected, since the various components drastically change value before and after the critical values shown by the dashed, vertical grey lines. Spin-splitting is observed, as the graph represents one global minima rather than the average between a time-reversal symmetry linked pair. The idealised vectors are taken at $\alpha = 0$ and $\alpha = 1$.

Consequently, we can define two vectors representing the idealised band composition evaluated at the bandgap minima. These are taken to be the eigenvectors for the $\alpha = 0$ trivial ($|\beta_{n,\text{Tri.}}\rangle$) and $\alpha = 1$ topological ($|\beta_{n,\text{Top.}}\rangle$) insulators. Since, the global minima vary in spin properties, then the idealised vectors should be spin-independent. The components of the idealised vectors are shown in *Fig. 10*.

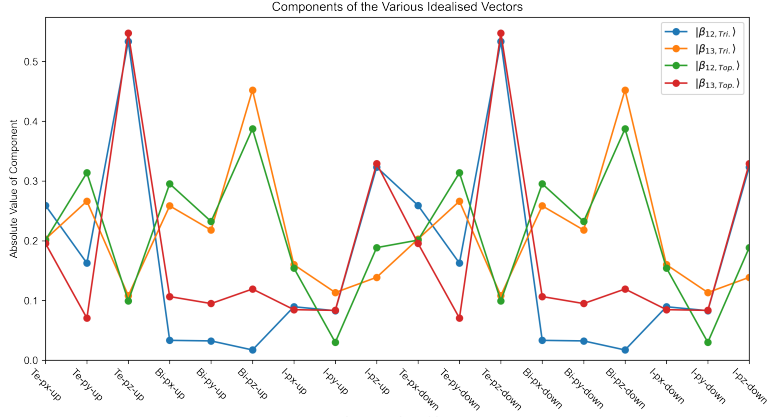


Figure 10: The components of the various idealised vectors are displayed. The spin-independence can be observed in the repetition of components for spin-up and spin-down pairs. Tellurium- P_z and Iodine- P_z have large components in $|\beta_{12,\text{Tri.}}\rangle$ and $|\beta_{13,\text{Top.}}\rangle$, whilst Bismuth- P_z is a large component in the other pair of idealised vectors. This is indicative of band-inversion and suggests the P_z orbitals are primarily involved in this state change.

The eigenvector at the energy bandgap minima ($|\phi_n\rangle$) and the idealised vectors should be absolute-valued and normalised to one. Furthermore, both valence and conduction bands contribute to the location of the bandgap minima, so both of their eigenvectors should be considered. These are bands $n = 12$ and $n = 13$ respectively for BiTeI. Using these vectors, a dot-product measures the angular separation between the measured eigenvector and the idealised state. These are used to provide two coefficients representing the trivial and topological character shown in *Eqns. 35* and *36* accordingly.

$$C_{\text{Tri.}} = \frac{\langle \beta_{12,\text{Tri.}} | \phi_{12} \rangle + \langle \beta_{13,\text{Tri.}} | \phi_{13} \rangle}{2} \quad (35)$$

$$C_{\text{Top.}} = \frac{\langle \beta_{12,\text{Top.}} | \phi_{12} \rangle + \langle \beta_{13,\text{Top.}} | \phi_{13} \rangle}{2} \quad (36)$$

The components of spin represented in the bands also drastically changes in the two insulating states due to band inversion, as shown in *Fig. 11*. These spin-components are determined by taking the expectation values of each pauli matrices with the summed, spin-up and spin-down components of the eigenvector.

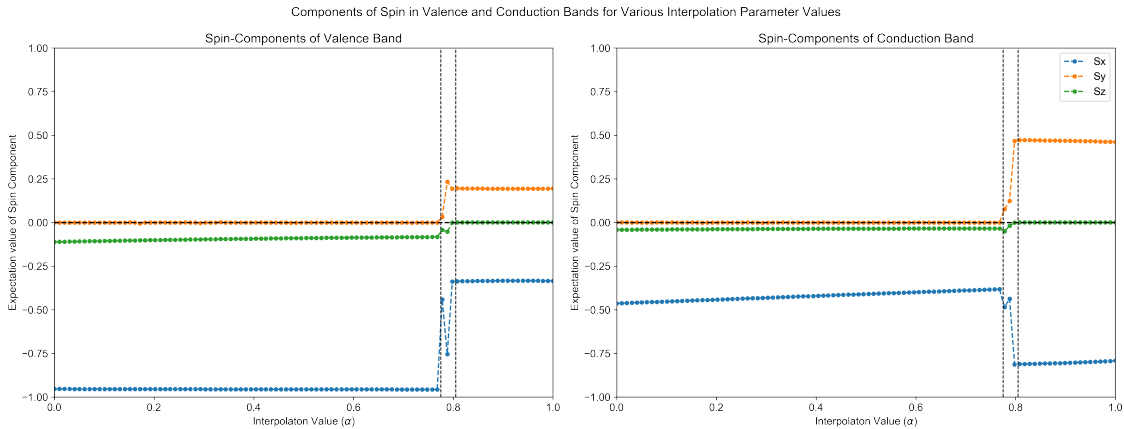


Figure 11: Shows the spin expectation values evaluated at the energy bandgap minima for various α . A distinct change in the spin-components is observed in the trivial and topological insulating states. The grey dashed lines indicate the boundaries of the semimetal state determined from eigenvalue analysis.

It can be seen that S_y is zero when BiTeI is a trivial insulator and non-zero when it is a topological insulator, whilst S_z shows the opposite behaviour. Therefore, conditions could be developed to determine the state using this spin behaviour. However, this is a potentially unreliable and more computationally intensive mode of determining the insulating state than the previous orbital components. This is because the spin depends on which minima is found by gradient descent, whilst the orbital analysis does not, so this method does not generalise well. Therefore, we proceeded with a spin-independent method of determining the insulating state. However, the time-reversal symmetric and Rashba effect properties of BiTeI are demonstrable in the spin behaviour as shown in *Fig. 12*.

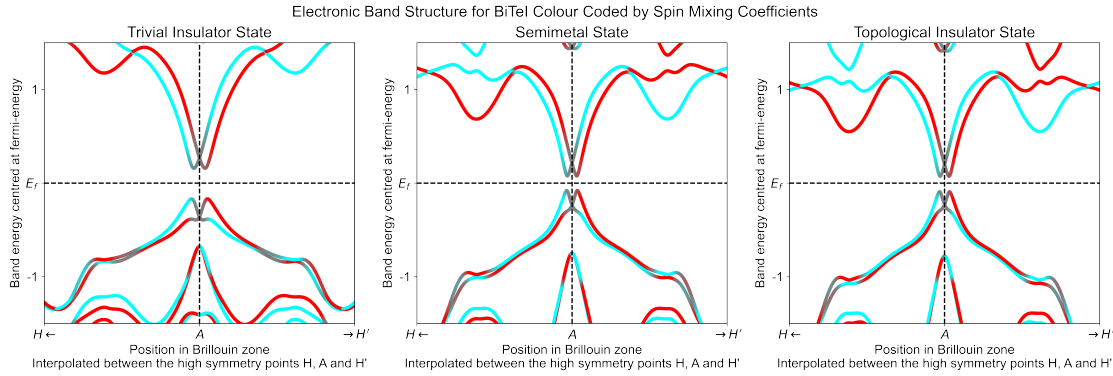


Figure 12: The valence and conduction band structure for BiTeI is shown along a section of the crystal symmetry lines H-A-H'. Red indicates the average contribution by spin-up eigenvector components whilst cyan indicates the spin-down components. Left, middle and right shows BiTeI in its trivial insulating, semimetal and topologically insulating states respectively. It can be seen that BiTeI exhibits spin-splitting through spatial-inversion symmetry breaking, caused by the Rashba effect.

Furthermore, *Fig. 13* shows the characteristic chiral monopoles and antimonopoles of a weyl semimetal and their spin properties. It can be seen that the initial six global minima of the trivial insulator state divide into twelve minima in the semimetal state, indicating the creation and location of the chiral monopoles.

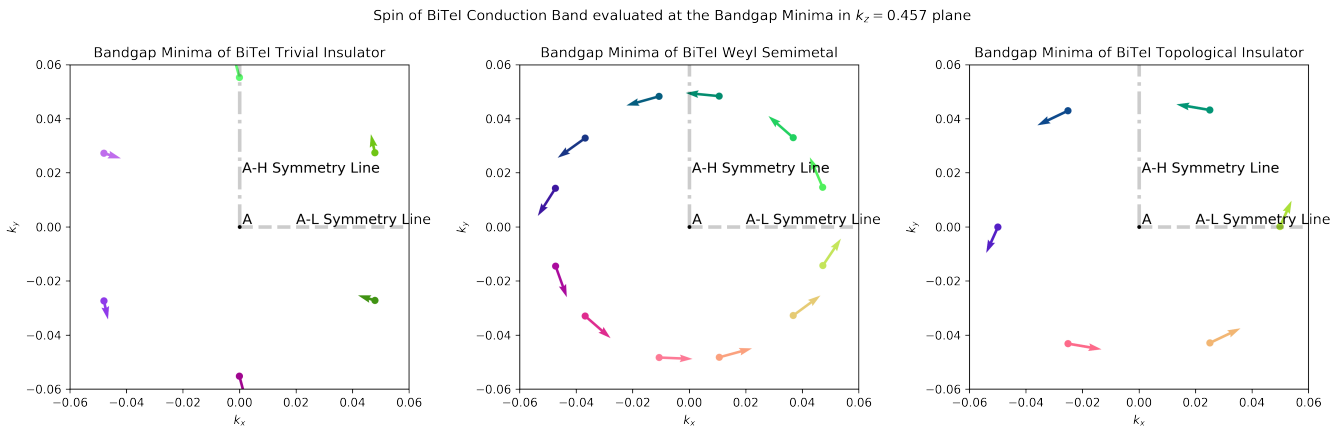


Figure 13: Shows the spins, as arrows and colours, of the conduction band eigenvectors evaluated at the bandgap minima for various values of the interpolation value $\alpha \in \{0.4, 0.786, 1\}$ corresponding to three BiTeI states. The arrows indicate the $\langle S_x \rangle$, also indicated by red colour, and $\langle S_y \rangle$, also indicated by green colour, of the spin components, whilst $\langle S_z \rangle$ is indicated by the blue colour component. In both the trivial insulator (left) and topological insulator (right) six global minima are observed near to the plane $k_z = 0.457$ along the A-H and A-L lines respectively. It can be seen that six weyl momopoles and six antimonopoles are created in the weyl semimetal state as expected (centre). It can be observed that their in-plane spins are orthogonal to their in-plane momentum. These pairs dissociate and then annihilate along the A-L symmetry line of the material to form a topological insulator state.

The behaviour of weyl monopoles trajectories within the Brillouin zone is more evident in *Fig. 14*. This shows the location where creation and annihilation of the monopoles occurs. Unexpectedly, the minima of the topological insulator are shown not to exist along the A-L and A-L' symmetry lines, but rather in the plane defined by A, L and Γ .

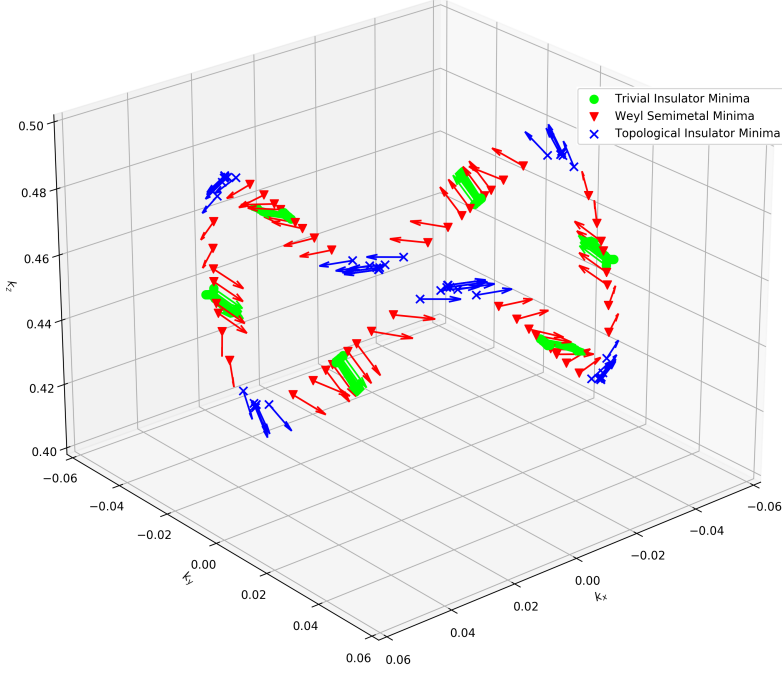


Figure 14: Shows the 3D arrangement of global minima at various values of $\alpha \in [0, 1]$, with colours indicating the classified states of the minima and arrows indicating spin expectation. It can be seen that all minima for trivial insulator states occur along $A-H$ and $A-H'$ symmetry lines. The red states indicate the centre of dirac cones in the semimetal phase, they are grouped into sets of twelve minima corresponding to the monopoles. These are shown to be created along the $A-H$ and $A-H'$ lines and then traverse through the Brillouin zone before annihilating at topological insulator minima. The topological minima are arranged out of the $k_z = 0.457$, giving a three-dimensional structure.

Returning to classification by *Eqns. 35* and *36* characters, the insulating state is determined to be the maximum value of these coefficients. This was found to be a successful strategy of classify the trivial and topological insulators, as shown in *Fig. 15*. The correct states are determined, without any outliers, at high resolution of the interpolation parameter.

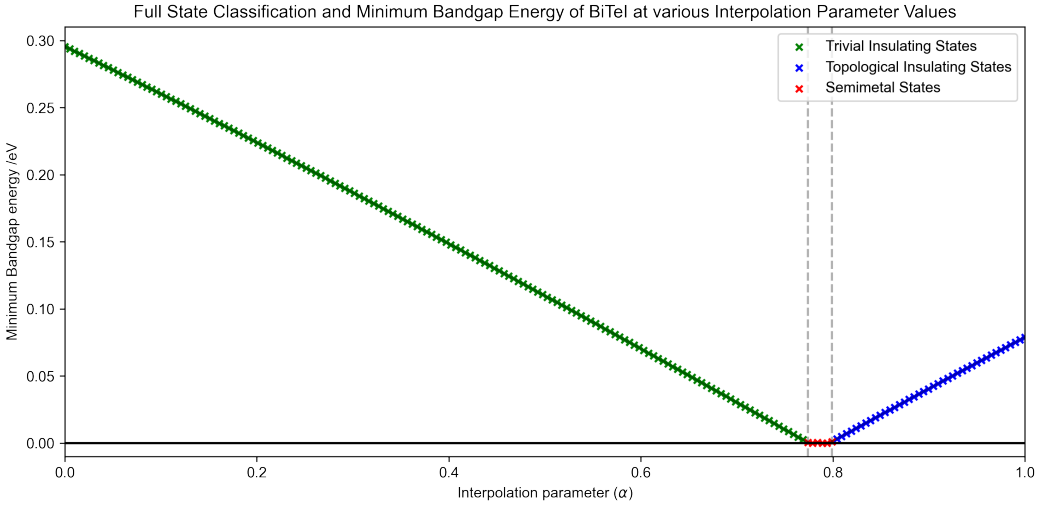


Figure 15: This shows the classifications of BiTeI states plotted in various colours. The trivial and topological insulating states are distinguished using the maximum of *Eqns. 35* and *36*. These classifications are shown on a plot of the minimum bandgap energies against the interpolation value to better illustrate the state transitions of BiTeI under hydrostatic pressure.

Therefore the classification of the semimetal, trivial insulator and topological insulator states of BiTeI has been demonstrated using the electronic band structure. However, the separation of weyl and dirac semimetals must still be implemented. It can be achieved using a analysis of the spin-orbit terms.

3.6 Analysis of Spin-Orbit Terms

To distinguish between the weyl and dirac semimetal states, requires directly analysing the hamiltonian. A dirac semimetal consists of a 4-fold degeneracy at the band crossing point. As discussed, this requires both spatial-inversion symmetry and time-reversal symmetry for dirac semimetals to arise. The Rashba effect is responsible for the spin-orbit coupling which breaks inversion symmetry. Therefore, a dirac semimetal will not be observed in the interpolated only hamiltonians, but may arise in a perturbed hamiltonian where a centrosymmetric BiTeI could occur.

Therefore, the presence of a spin-orbit interaction can be used to determine between a weyl and dirac semimetal. Once a hamiltonian is classified as a semimetal from the aforementioned procedures, then the presence of non-zero spin-orbit terms indicates it is a weyl semimetal. This is described by *Eqn. 34*, when $(H_{\uparrow\downarrow}(\vec{k}) \neq 0) \cup (H_{\downarrow\uparrow}(\vec{k}) \neq 0)$. Otherwise, it is a dirac semimetal. The implementation of this final condition concludes our classification procedure for BiTeI, allowing a dataset of BiTeI's hamiltonians and their respective classifications to be produced for application to machine learning.

4 Conclusion

The novel approaches developed to analyse Bismuth-Tellurium-Iodide crystals were successful at categorising the expected states and matched results from other analyses. Generalised techniques were developed using the energy bandgap, eigenvector components and spin-orbit interaction, to robustly classify BiTeI, under different deformations, into the four described states. The overall methodology is summarised in *Fig. 16*. The parallel tight-binding equation solver and gradient descent were very successful and pivotal in the production of all the results. These techniques utilised new developments in GPU acceleration and parameter-optimisation to efficiently perform the crucial calculations. In addition, the methods are robust to additional noise, allowing a larger and more varied analytical dataset to be developed. This preemptively reduces the neural network overfitting problem. Moreover, this approach is general, allowing a similar methodology to be easily applied to other crystalline materials with minor modifications. Therefore, it is feasible to efficiently create large datasets of many crystalline materials, enabling the development and benchmarking of models which operate upon a variety of materials. Overall, it is hoped that this will streamline research into material development by identifying more promising candidates and deformations which yield exciting properties to then experimentally verify.

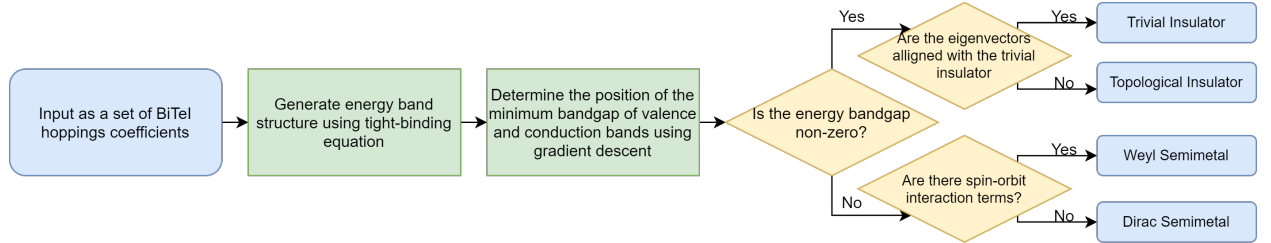


Figure 16: Shows a schematic approach to the procedure, where initial hopping coefficients are classified into the four states BiTeI is expected to exhibit.

The procedures correctly identify the weyl and dirac semimetal states as well as the trivial and topological insulating states exhibited by BiTeI. The respective gapless and gapped-bulk properties were observed in the energy band structures. These also offered insight into the process of band inversion, required to form topological insulators. Additionally, the weyl semimetal's monopole and antimonopole quasiparticles were observable as twelve global minima, demonstrating their existence between a range of hydrostatic pressures for the non-centrosymmetric BiTeI. It was shown that these are created, then migrate symmetrically through the Brillouin zone before being annihilated in different pairs to form the topological insulator. The presence of both band-inversion and Rashba spin-splitting was demonstrated in the eigenvector analysis, alongside the evolution of spin and orbital components with hydrostatic pressure. Furthermore, trivial and topological insulators were shown to be distinct states which cannot be adiabatically transformed into one another without forming a gapless weyl semimetal state. Consequently, the developed methods fulfilled our primary aim of this project to develop a standardised dataset and give insight into BiTeI under various deformations. However, there remains some caveats to the procedure, discussed below.

If sufficiently large perturbations are introduced, the fast idealised vector analysis may be ineffective as the proportions of orbitals represented in the valence and conduction band structure will begin differ without changing the material's state. Therefore, for this method to remain precise, only small perturbations should be used to expand the dataset or a re-sampling of the idealised vectors should be undertaken.

Furthermore, the classification list we developed is likely not exhaustive in multiple ways. A nodal semimetal [73] is a further semimetal classification which may occur with certain perturbations. These are characterised by lines of band crossings and would be classified as a weyl semimetal by our model. Despite this, inclusion of further divisions of the weyl semimetal state were out-of-scope for this project due to time constraints. In addition, there exists fifteen sub-classifications of the topological insulator state, characterised by combinations of the \mathbb{Z}_2 invariant topological numbers $\nu_0; (\nu_1, \nu_2, \nu_3)$. These are all grouped collectively under a single topological insulator state in our approach.

Finally, there may exist undocumented states in the possible hamiltonian phase space. By definition, these are not identifiable using our approach of developing a dataset. However, indirect evidence of these undocumented states, and further sub-classifications, may be observed in the machine learning model. The cost function of a machine learning model may grow anomalously large when one of these undocumented states are encountered. This can occur when a state is misrepresented in the dataset, so the model may struggle to classify it. If this behaviour is observed, then further investigation will be undertaken to determine the characteristics of these states and whether they are novel.

Overall, these deficiencies in the approach are acceptable for the fast and efficient classifier we required for generating a large dataset. The nodal semimetal and finer classification of topological insulators should not impede the machine learning model, as they are still represented under the broader classifications used. In addition, assumptions used in the production of the dataset are made clear. Thus, the dataset is fully documented making it a useful and standardised platform to verify future work in this area. Using this dataset we can now proceed with developing quantum machine learning and classical machine learning models in the continuation of this project.

4.1 Outlook of Work

4.1.1 Benchmarking Supervised Learning Models

This project work has enabled the development of a large analytical dataset pairing BiTeI hamiltonians to their resultant material classification, making it suitable for application to supervised learning [74]. In the immediate follow-up work to this project, the dataset will be partitioned into training and testing subsets, allowing new machine learning techniques to be proven against this well-studied system. There have been several attempts [75–77] at applying machine learning to condensed matter systems and this dataset offers a further avenue for verifying such approaches, particularly in 3D topological systems. Once a machine learning model is benchmarked using this dataset, the technique can confidently be applied to further systems which display similar characteristics. The dataset can also be used to expand the number of training samples for the model in these cases.

4.1.2 Quantum Machine Learning Approach

Quantum machine-learning is an avenue of modelling condensed matter systems which may be particularly successful due to the shared quantum nature [78]. This approach would allow faster computation of quantum behaviours, such as entanglement involved in the emergent material phenomena. The dataset produced in this project can be used to assess the effectiveness of such an approach. Therefore, it can be determined whether quantum machine learning techniques better model condensed matter systems than the classical machine learning approaches. Furthermore, this dataset includes examples of emergent quantum phenomena, so it is the perfect dataset for comparing such models.

4.1.3 Generalising for Many Crystalline Materials

When developing this approach, a universal crystal embedding procedure arose which can result in a single machine learning model being applied to a wide variety of crystalline materials. This extension of the procedure is very promising and will be explored in a follow up to this work. The general form of artificial neural networks required for property predictions are

known as classification networks. These are the most common application of neural networks. Consequently, a wide variety of preexisting neural network architectures exist for this form of problem. Benchmarking should begin on the most primitive yet general neural network techniques, such as fully-connected neural networks, before testing more advanced architectures with narrower applications, such as convolution or transformer networks. However, these more advanced architectures are purpose-built for their respective tasks such as computer vision or natural language processing. Therefore, to achieve the optimal results might require novel neural network architectures designed specifically for condensed matter system. The combination of a universal crystal embedding and purpose-built neural networks would enable mappings learnt from one material to be usefully applied to another, including those without analytical solutions. This approach, if proved successful on well-studied materials, could streamline development of new materials. Moreover, if it becomes sufficiently well-trained, the model could be used to specify desirable properties and deduce a physical crystal featuring these properties. The prospects of this extended approach are exciting with potentially many applications.

References

- [1] A. Bolotin, “Computational complexity and the interpretation of a quantum state vector,” 2013.
- [2] N. W. Ashcroft and N. D. Mermin, *Solid state physics*. Cengage, 2021.
- [3] F. Bloch, “Über die quantenmechanik der elektronen in kristallgittern,” *Zeitschrift für Physik*, vol. 52, pp. 555–600, Jul 1929.
- [4] V. L. Gurevich and A. Thellung, “Quasimomentum in the theory of elasticity and its conservation,” *Phys. Rev. B*, vol. 42, pp. 7345–7349, Oct 1990.
- [5] M. Born and R. Oppenheimer, “Zur quantentheorie der moleküle,” *Annalen der Physik*, vol. 389, no. 20, pp. 457–484, 1927.
- [6] P. Debye, “Zur theorie der spezifischen wärmen,” *Annalen der Physik*, vol. 344, no. 14, pp. 789–839, 1912.
- [7] A. V. Anda, S. S. Makler, R. G. Barrera, and H. M. Pastawski, “Electron - phonon effects on transport in mesoscopic heterostructures,” *Brazilian Journal of Physics*, vol. 24, pp. 330–336, 1994.
- [8] P. Babilotte, E. Morozov, P. Ruello, D. Mounier, M. Edely, J.-M. Breteau, A. Bulou, and V. Gusev, “Physical mechanism of coherent acoustic phonons generation and detection in gaas semiconductor,” *Journal of Physics: Conference Series*, vol. 92, p. 012019, dec 2007.
- [9] I. E. Tamm, “The electrodynamics of anisotropic media in the special theory of relativity,” 1923.
- [10] F. Giustino, “Electron-phonon interactions from first principles,” *Rev. Mod. Phys.*, vol. 89, p. 015003, Feb 2017.
- [11] J. Zhou, H. D. Shin, K. Chen, B. Song, R. A. Duncan, Q. Xu, A. A. Maznev, K. A. Nelson, and G. Chen, “Direct observation of large electron-phonon interaction effect on phonon heat transport,” *Nature Communications*, vol. 11, p. 6040, Nov 2020.
- [12] J. L. Mañes, “Symmetry-based approach to electron-phonon interactions in graphene,” *Phys. Rev. B*, vol. 76, p. 045430, Jul 2007.
- [13] L. N. Cooper, “Bound electron pairs in a degenerate fermi gas,” *Phys. Rev.*, vol. 104, pp. 1189–1190, Nov 1956.
- [14] J. Bardeen, L. N. Cooper, and J. R. Schrieffer, “Microscopic theory of superconductivity,” *Phys. Rev.*, vol. 106, pp. 162–164, Apr 1957.
- [15] J. E. Lennard-Jones, “The electronic structure of some diatomic molecules,” *Trans. Faraday Soc.*, vol. 25, pp. 668–686, 1929.

- [16] I. G. Kaplan, “Pauli exclusion principle and its theoretical foundation,” 2019.
- [17] D. Rayner and W. Hartree, “Self-consistent field, with exchange, for beryllium,” *Proceedings of the Royal Society of London. Series A - Mathematical and Physical Sciences*, vol. 150, no. 869, pp. 9–33, 1935.
- [18] J. C. Slater, “A simplification of the hartree-fock method,” *Phys. Rev.*, vol. 81, pp. 385–390, Feb 1951.
- [19] P. Hohenberg and W. Kohn, “Inhomogeneous electron gas,” *Phys. Rev.*, vol. 136, pp. B864–B871, Nov 1964.
- [20] J. C. Slater and G. F. Koster, “Simplified lcao method for the periodic potential problem,” *Phys. Rev.*, vol. 94, pp. 1498–1524, Jun 1954.
- [21] Brillouin, L., “Les électrons libres dans les métaux et le rôle des réflexions de bragg,” *J. Phys. Radium*, vol. 1, no. 11, pp. 377–400, 1930.
- [22] W. Kohn, “Electrons, positrons and holes,” *Materials Research Bulletin*, vol. 5, no. 8, pp. 641–654, 1970.
- [23] M. Rohlfing and S. G. Louie, “Electron-hole excitations and optical spectra from first principles,” *Phys. Rev. B*, vol. 62, pp. 4927–4944, Aug 2000.
- [24] S. S. Li, *Semiconductor physical electronics*, pp. 247–503. Springer Science & Business Media, 2012.
- [25] A. K. Geim and K. S. Novoselov, “The rise of graphene,” *Nature Materials*, vol. 6, pp. 183–191, Mar 2007.
- [26] W. Zawadzki, “Semirelativity in semiconductors: A review,” *Journal of Physics: Condensed Matter*, vol. 29, no. 37, p. 373004, 2017.
- [27] L. Hrivnák, “Relativistic analogies in direct-gap semiconductors,” *Progress in Quantum Electronics*, vol. 17, no. 3, pp. 235–271, 1993.
- [28] N. Armitage, E. Mele, and A. Vishwanath, “Weyl and dirac semimetals in three dimensional solids,” *Reviews of Modern Physics*, vol. 90, 05 2017.
- [29] A. Bansil, H. Lin, and T. Das, “Colloquium: Topological band theory,” *Reviews of Modern Physics*, vol. 88, jun 2016.
- [30] J. Wang, S. Deng, Z. Liu, and Z. Liu, “The rare two-dimensional materials with Dirac cones,” *National Science Review*, vol. 2, pp. 22–39, 01 2015.
- [31] H. Weyl, “Elektron und gravitation. i,” *Zeitschrift für Physik*, vol. 56, pp. 330–352, May 1929.
- [32] S.-Y. Xu, I. Belopolski, N. Alidoust, M. Neupane, G. Bian, C. Zhang, R. Sankar, G. Chang, Z. Yuan, C.-C. Lee, S.-M. Huang, H. Zheng, J. Ma, D. S. Sanchez, B. Wang, A. Bansil, F. Chou, P. P. Shibayev, H. Lin, S. Jia, and M. Z. Hasan, “Discovery of a weyl fermion semimetal and topological fermi arcs,” *Science*, vol. 349, pp. 613–617, aug 2015.
- [33] L. Lu, Z. Wang, D. Ye, L. Ran, L. Fu, J. D. Joannopoulos, and M. Soljačić, “Experimental observation of weyl points,” *Science*, vol. 349, pp. 622–624, aug 2015.
- [34] S. Murakami, “Phase transition between the quantum spin hall and insulator phases in 3d: emergence of a topological gapless phase,” *New Journal of Physics*, vol. 9, pp. 356–356, sep 2007.
- [35] C. Kane, “Chapter 1 - topological band theory and the z2 invariant,” in *Topological Insulators* (M. Franz and L. Molenkamp, eds.), vol. 6 of *Contemporary Concepts of Condensed Matter Science*, pp. 3–34, Elsevier, 2013.
- [36] S. Pancharatnam, “Generalized theory of interference, and its applications,” *Proceedings of the Indian Academy of Sciences - Section A*, vol. 44, pp. 247–262, Nov 1956.
- [37] M. V. Berry, “Quantal phase factors accompanying adiabatic changes,” *Proceedings of the Royal Society of London. A. Mathematical and Physical Sciences*, vol. 392, no. 1802, pp. 45–57, 1984.

- [38] S. Murakami and S. ichi Kuga, “Universal phase diagrams for the quantum spin hall systems,” *Physical Review B*, vol. 78, oct 2008.
- [39] M. Z. Hasan, G. Chang, I. Belopolski, G. Bian, S.-Y. Xu, and J.-X. Yin, “Weyl, dirac and high-fold chiral fermions in topological quantum matter,” *Nature Reviews Materials*, vol. 6, pp. 784–803, apr 2021.
- [40] A. P. Sakhy, C.-Y. Huang, G. Dhakal, X.-J. Gao, S. Regmi, X. Yao, R. Smith, M. Sprague, B. Singh, H. Lin, S.-Y. Xu, F. Tafti, A. Bansil, and M. Neupane, “Observation of fermi arcs and weyl nodes in a non-centrosymmetric magnetic weyl semimetal,” 2022.
- [41] S. Jia, S.-Y. Xu, and M. Z. Hasan, “Weyl semimetals, fermi arcs and chiral anomalies,” *Nature Materials*, vol. 15, pp. 1140–1144, oct 2016.
- [42] K. Deng, G. Wan, P. Deng, K. Zhang, S. Ding, E. Wang, M. Yan, H. Huang, H. Zhang, Z. Xu, J. Denlinger, A. Fedorov, H. Yang, W. Duan, H. Yao, Y. Wu, S. Fan, H. Zhang, X. Chen, and S. Zhou, “Experimental observation of topological fermi arcs in type-ii weyl semimetal mote2,” *Nature Physics*, vol. 12, pp. 1105–1110, Dec 2016.
- [43] Z. Hasan, “What can you do with a weyl semimetal?,” Oct 2016.
- [44] B. Yan and C. Felser, “Topological materials: Weyl semimetals,” *Annual Review of Condensed Matter Physics*, vol. 8, no. 1, pp. 337–354, 2017.
- [45] A. A. Soluyanov and D. Vanderbilt, “Computing topological invariants without inversion symmetry,” *Phys. Rev. B*, vol. 83, p. 235401, Jun 2011.
- [46] L. Fu and C. L. Kane, “Topological insulators with inversion symmetry,” *Phys. Rev. B*, vol. 76, p. 045302, Jul 2007.
- [47] A. Tanaka and S. Takayoshi, “A short guide to topological terms in the effective theories of condensed matter,” *Science and Technology of Advanced Materials*, vol. 16, p. 014404, feb 2015.
- [48] H. A. Kramers, “Théorie générale de la rotation paramagnétique dans les cristaux,” *Proc. Acad. Amst*, vol. 33, no. 6, 1930.
- [49] S.-Q. SHEN, W.-Y. SHAN, and H.-Z. LU, “TOPOLOGICAL INSULATOR AND THE DIRAC EQUATION,” *SPIN*, vol. 01, pp. 33–44, jun 2011.
- [50] P. Roushan, J. Seo, C. V. Parker, Y. S. Hor, D. Hsieh, D. Qian, A. Richardella, M. Z. Hasan, R. J. Cava, and A. Yazdani, “Topological surface states protected from backscattering by chiral spin texture,” *Nature*, vol. 460, pp. 1106–1109, Aug 2009.
- [51] C.-K. Lee, J. H. Lee, B.-T. Zhang, and J.-L. He, “Chapter 2 - topological insulators and applications,” in *2D Materials for Nanophotonics* (Y. M. Jhon and J. H. Lee, eds.), Nanophotonics, pp. 81–138, Elsevier, 2021.
- [52] J. E. Moore, “The birth of topological insulators,” *Nature*, vol. 464, pp. 194–198, Mar 2010.
- [53] T. W. Schmitt, M. R. Connolly, M. Schleenvoigt, C. Liu, O. Kennedy, J. M. Chávez-Garcia, A. R. Jalil, B. Bennemann, S. Trellenkamp, F. Lentz, E. Neumann, T. Lindström, S. E. de Graaf, E. Berenschot, N. Tas, G. Mussler, K. D. Petersson, D. Grützmacher, and P. Schüffelgen, “Integration of topological insulator josephson junctions in superconducting qubit circuits,” *Nano Letters*, vol. 22, pp. 2595–2602, mar 2022.
- [54] M. S. Bahramy, B.-J. Yang, R. Arita, and N. Nagaosa, “Emergence of non-centrosymmetric topological insulating phase in bitei under pressure,” *Nature Communications*, vol. 3, p. 679, Feb 2012.
- [55] C. L. Kane and E. J. Mele, “Quantum spin hall effect in graphene,” *Phys. Rev. Lett.*, vol. 95, p. 226801, Nov 2005.
- [56] J. S. Lee, A. Richardella, R. D. Fraleigh, C.-x. Liu, W. Zhao, and N. Samarth, “Engineering the breaking of time-reversal symmetry in gate-tunable hybrid ferromagnet/topological insulator heterostructures,” *npj Quantum Materials*, vol. 3, p. 51, Oct 2018.

- [57] K. Ishizaka, M. S. Bahramy, H. Murakawa, M. Sakano, T. Shimojima, T. Sonobe, K. Koizumi, S. Shin, H. Miyahara, A. Kimura, K. Miyamoto, T. Okuda, H. Namatame, M. Taniguchi, R. Arita, N. Nagaosa, K. Kobayashi, Y. Murakami, R. Kumai, Y. Kaneko, Y. Onose, and Y. Tokura, “Giant rashba-type spin splitting in bulk bsite,” *Nature Materials*, vol. 10, pp. 521–526, Jul 2011.
- [58] C. Bradley and A. Cracknell, *The mathematical theory of symmetry in solids: representation theory for point groups and space groups*, pp. 95–119. Oxford University Press, 2010.
- [59] S. Datta and B. Das, “Electronic analog of the electro-optic modulator,” *Applied Physics Letters*, vol. 56, no. 7, pp. 665–667, 1990.
- [60] J. Vamathevan, D. Clark, P. Czodrowski, I. Dunham, E. Ferran, G. Lee, B. Li, A. Madabhushi, P. Shah, M. Spitzer, and S. Zhao, “Applications of machine learning in drug discovery and development,” *Nature Reviews Drug Discovery*, vol. 18, pp. 463–477, Jun 2019.
- [61] H. Gerdes, P. Casado, A. Dokal, M. Hijazi, N. Akhtar, R. Osuntola, V. Rajeeve, J. Fitzgibbon, J. Travers, D. Britton, S. Khorsandi, and P. R. Cutillas, “Drug ranking using machine learning systematically predicts the efficacy of anti-cancer drugs,” *Nature Communications*, vol. 12, p. 1850, Mar 2021.
- [62] A. Lavecchia, “Machine-learning approaches in drug discovery: methods and applications,” *Drug Discovery Today*, vol. 20, no. 3, pp. 318–331, 2015.
- [63] S. Dara, S. Dhamercherla, S. S. Jadav, C. M. Babu, and M. J. Ahsan, “Machine learning in drug discovery: A review,” *Artificial Intelligence Review*, vol. 55, pp. 1947–1999, Mar 2022.
- [64] S. Hochreiter, G. Klambauer, and M. Rarey, “Machine learning in drug discovery,” *Journal of Chemical Information and Modeling*, vol. 58, no. 9, pp. 1723–1724, 2018. PMID: 30109927.
- [65] V. Stanev, K. Choudhary, A. G. Kusne, J. Paglione, and I. Takeuchi, “Artificial intelligence for search and discovery of quantum materials,” *Communications Materials*, vol. 2, p. 105, Oct 2021.
- [66] A. Einstein, “The Foundation of the General Theory of Relativity,” *Annalen Phys.*, vol. 49, no. 7, pp. 769–822, 1916.
- [67] P. Liashchynskyi and P. Liashchynskyi, “Grid search, random search, genetic algorithm: A big comparison for nas,” 2019.
- [68] J. Bergstra and Y. Bengio, “Random search for hyper-parameter optimization.,” *Journal of machine learning research*, vol. 13, no. 2, 2012.
- [69] M. del Rosario, “An overview of stochastic gradient descent in machine learning,” 2019.
- [70] S. Ruder, “An overview of gradient descent optimization algorithms,” 2016.
- [71] D. P. Kingma and J. Ba, “Adam: A method for stochastic optimization,” 2014.
- [72] S. Salman and X. Liu, “Overfitting mechanism and avoidance in deep neural networks,” 2019.
- [73] A. A. Burkov, M. D. Hook, and L. Balents, “Topological nodal semimetals,” *Physical Review B*, vol. 84, dec 2011.
- [74] V. Nasteski, “An overview of the supervised machine learning methods,” *HORIZONS.B*, vol. 4, pp. 51–62, 12 2017.
- [75] Y. Zhang and E.-A. Kim, “Quantum loop topography for machine learning,” *Physical Review Letters*, vol. 118, may 2017.
- [76] P. Zhang, H. Shen, and H. Zhai, “Machine learning topological invariants with neural networks,” *Physical Review Letters*, vol. 120, feb 2018.

- [77] G. Pilania, C. Wang, X. Jiang, S. Rajasekaran, and R. Ramprasad, “Accelerating materials property predictions using machine learning,” *Scientific Reports*, vol. 3, p. 2810, Sep 2013.
- [78] S. Stanisic, J. L. Bosse, F. M. Gambetta, R. A. Santos, W. Mruczkiewicz, T. E. O’Brien, E. Ostby, and A. Montanaro, “Observing ground-state properties of the fermi-hubbard model using a scalable algorithm on a quantum computer,” *Nature Communications*, vol. 13, p. 5743, Oct 2022.

Developing Machine Learning Architectures Purpose-Built for Condensed Matter Physics

George Bird george.bird@student.manchester.ac.uk
Supervisor: Dr. Mohammad Saeed Bahramy

*Department of Physics and Astronomy
University of Manchester*

March 2023

Abstract

Machine learning has already been shown to be an effective tool in modelling the properties of crystalline systems. However, most approaches to date can be considered as a repurposing of computer vision architectures. We posit that a form of neural network which is purpose-built for condensed matter physics, by considering and leveraging important symmetries, maybe even more effective than these prior approaches.

To achieve this, a ground-up review of deep learning methods is undertaken, with a substantial emphasis on the symmetry behaviours of common functions. Features which are advantageous to condensed matter modelling are highlighted. In this, several deficits of existing models are defined, with proven resolutions.

The project concludes with a machine learning model which can be applied universally to all crystalline systems and is able to predict a wide repertoire of properties, by making use of the reciprocal-space. Models which analyse the orbital overlaps of the crystal Bismuth-Telluride-Iodide are also conducted, and shown to have some success in predicting emergent quantum states such as topological insulators. Some of the proposed models, and newly identified problems, may also have a wider impact on other applications of machine learning.

Contents

1	Introduction	3
1.1	Project Overview and Prior Work	3
1.2	The Potential of Machine Learning for Condensed Matter Applications	3
2	Background and Methodology	4
2.1	Symmetries of Brillouin Zones	4
2.1.1	Novel Rotational Symmetry Encoding	5
2.1.2	Hermitian Symmetry	6
2.1.3	Time-Reversal and Spatial-Inversion	6
2.1.4	Discrete Translational Symmetry	7
2.2	Novel Crystalline Material Optimising Through Gradient Descent	8
2.3	Overview of Fully-Connected Approach	8
2.4	Overview of Convolutional Architectures	9
2.4.1	Novel High-Dimensional Hybrid Convolutional Architecture	9
2.4.2	Spatial Equivariance and Spatial Invariance	10
2.5	Defining The Problem of Gradient Diffusion	12
2.6	Toroidal Convolutions	13
2.7	Sequential Layer's Activation Complexities	14
2.7.1	Standard Sequential and Residual Models	14
2.7.2	Defining Deficits of the Residual Models	15
2.8	The Medium Extractor - A Novel Architecture	17
2.8.1	Tuned and Free Attention	18
2.9	Generating Datasets for Benchmarking on BiTeI	20
2.10	Sample Rolling of Classical Computer Vision Tasks	20
3	Results & Discussion	21
3.1	Properties of BiTeI Dataset	21
3.2	Evaluation of Invariance on Computer Vision Datasets	22
3.3	Machine Learning applied to Condensed Matter Physics	27
4	Conclusion	29
	Appendices	32
	A Neural Architectures	32
	B BiTeI Dataset	33
	C MNIST	34
	D CIFAR10	35

1 Introduction

1.1 Project Overview and Prior Work

Both machine learning and condensed matter physics are considered among the most exciting and fruitful avenues of modern scientific research. In this thesis, the considerable overlap between these domains will be made clear. A novel interdisciplinary approach to developing new materials, defined by emergent quantum behaviours, will be demonstrated through custom-designed machine learning architectures. The term "architecture" represents the wiring pattern and overall structure of the network, independent of its training to perform a particular task. The grand aim is to develop strong computational models which can quickly predict the properties of untested materials derived from the understanding of other crystalline systems. The goal is to streamline the search for promising materials, which can then be verified experimentally. Moreover, a purpose-built machine learning approach to evaluating these systems have the unique potential to embed desirable properties into current crystal configurations [1], enabling a host of new applications in spintronics [2,3], quantum computing [3], energy storage [4], and a greater understanding of quantum field theories through exotic quasiparticles [5,6].

In the previous semester [7], analytic techniques were developed for the crystal Bismuth-Telluride-Iodide (BiTeI) to determine its state under particular mechanical distortions. This crystal was chosen as it exhibits a range of well-understood emergent quantum phenomena under various conditions, including trivial and topological insulating states alongside Weyl and Dirac semimetallic states. The Weyl-semimetal and topological insulator states result from strong spin-orbit couplings which break spatial-inversion symmetry, through the Rashba effect [8]. This causes spin-splitting of the otherwise degenerate electronic band structure, allowing an intermediate Weyl semimetal state to exist separating the trivial and topological insulating states in the phase space. A rearrangement of the band structure, known as band inversion, occurs in the Weyl-semimetal state enabling the \mathbb{Z}_2 topological invariant to change which distinguishes the trivial and topological insulating states. It was demonstrated that varying hydrostatic pressure is sufficient for BiTeI to display these emergent quantum states. A novel algorithm was then developed to determine the corresponding state from interpolated hoppings between neighbouring atoms in the lattice.

Consequently, BiTeI offered an ideal system to benchmark and compare various computational approaches to understanding and predicting the presence of these material properties. Hence, enabling a particular model's effectiveness to be determined on a well-understood system before applying it to new systems. Additionally, the pairing of atomic orbital hoppings to a resultant state enables the use of supervised machine-learning techniques. The prior work focussed on how this dataset could be produced efficiently, whereas this thesis will explore the development of novel machine-learning architectures. The intent is to develop purpose-built models which leverage crystal properties for improved accuracy in classifying states of BiTeI. Despite an analytical algorithm already existing, the aim is to generalise these architectures to allow knowledge gained on one crystalline system to be applied to another, alongside offering alternative insights into the nature and emergence of the states.

1.2 The Potential of Machine Learning for Condensed Matter Applications

Neural networks, or deep-learning, is a subset of machine learning algorithms which are widely applicable to many circumstances. Particularly, they are advantageous for problems with a large number of degrees of freedom which interact non-linearly and cannot be easily visualised or interpreted by simpler methods or humans. Predicting emergent quantum phenomena in crystalline systems falls into this category, making deep-learning a promising tool for understanding these phenomena. Moreover, if beneficial, the operations may become hermitian or unitary allowing them to closely model the quantum dynamics within the material. The exact band-structure make-up of the various material states may also be highly variable, and deep-learning's adeptness at generalising classifications is also strongly applicable.

Deep-learning models consist of stacked and optimisable linear algebra operations sandwiched between non-linear activation functions. The particular linear algebra operations and activation functions used are defined by its architecture, with the particular structure having a large impact on the success of the model on its respective task. These operations include tunable parameters (ϱ) which are optimised using a process called backpropagation and gradient-descent, the latter shown in *Eqn. 1*, to achieve increasingly better performance. Free parameters, or activations, represent the information to be processed by the model and are an encoded representation of important aspects of the crystalline system.

$$\varrho_{i+1} = \varrho_i - \eta \frac{\partial C}{\partial \varrho_i} \quad (1)$$

Where C is an error function to be minimised, known as cost, with $0 < \eta \ll 1$ being a small step, known as the learning rate.

Machine learning has already had significant in-roads in analogous search domains, such as drug discovery [9], and numerous adoptions of the technology have already been demonstrated for condensed matter systems [10–15]. However, the latter primarily feature adapted architectures from computer vision [10–13] and natural language processing [15]. These

models are not structured to exploit the features of condensed matter systems but rather their respective domains, which may result in poorer predictive performance when they are applied to crystalline systems. Often these crystalline systems are reformulated to superficially appear as a computer vision or natural-language problem, yet do not share the respective relations and symmetries that these models leverage. Additionally, the reformulation process may obfuscate important features of the system. Therefore, it is preferable to construct a custom machine-learning model which accepts the condensed matter parameters in their natural form alongside using an architecture designed to accelerate learning and boost accuracy by utilising the characteristics of the materials. This ground-up approach appears absent in the literature, so offers an exciting avenue to create more potent computer models.

A particular emphasis on generating a large, varied dataset, using the previously defined techniques, is essential such that these models learn the underlying physics as opposed to shortcircuiting the problems through simpler means. To this end, adding constrained physical noise to the dataset, and how it in turn affects the state classification, is explored in this project. This noise encourages the model to correctly approximate the physical behaviour, by penalising the unphysical shortcut approaches since they do not generalise well. It is feasible that the model will still find unexpected shortcuts, but analysis of these may instead reveal hidden physical insights. Further, only a model which has learnt the underlying physics has the capacity to reverse engineer desirable properties into a material in a physical manner.

Two primary routes of constructing condensed matter neural networks will be explored: one operating on the atomic hoppings derived from density functional theory, shown in *Eqn. 2*, and the other utilising the symmetries of the Brillouin zone, shown in *Eqn. 3*. To guarantee the symmetry leveraging characteristics of the models, a series of tests will be performed on common machine learning datasets, MNIST [16] and CIFAR10 [17], which are perturbed in equivalent symmetric ways to the BiTeI crystal. Thus, performance in these more-illustrative domains maps directly to the condensed matter applications and enables wider applicability of the architectures.

$$\hat{H}_{ij\vec{A}} = \langle \psi_i | \hat{H} | \psi_j \rangle = \int d\vec{x} \psi_i^*(\vec{x}) \hat{H}(\vec{x}) \psi_j \left(\vec{x} - \sum_k^d A_k \vec{r}_k \right) \quad (2)$$

With $\hat{H}_{ij\vec{A}}$ being the complex wavefunction overlap termed "hoppings", determined using density functional theory. Whilst \vec{r}_k are the lattice vectors for a d dimensional crystal with A_k giving a particular number of cell offsets which the orbital overlap, between wavefunctions ψ , is evaluated for. For the BiTeI system studied, A takes 1155 unique combinations, with 18 orbitals considered for all permutations of Bismuth ($6P_{\{x,y,z\}\{\uparrow,\downarrow\}}$), Tellurium ($5P_{\{x,y,z\}\{\uparrow,\downarrow\}}$) and Iodide ($5P_{\{x,y,z\}\{\uparrow,\downarrow\}}$). All of these hopping terms are used to evaluate the material state, however, as later discussed, only a truncated number is provided to the network to mitigate the network shortcircuiting the problem.

$$\hat{H}_{ij}(\vec{k}) = \mathcal{F}_{\vec{k}} [\hat{H}_{ij\vec{A}}] = \sum_{\forall \vec{A}} e^{i\vec{k} \cdot (\sum_k^d A_k \vec{r}_k)} \hat{H}_{ij\vec{A}} \quad (3)$$

The reciprocal space, or crystal-momentum (\vec{k}) space, is a Fourier transform of the hoppings and allows for a model universality to crystalline systems. Unlike hoppings, which consist of an arbitrarily chosen set of orbital overlaps, the electronic behaviour of a crystal can be interpreted through a bounded unique region known as the Brillouin zone, which is then tessellated to form the full reciprocal space. The hoppings can be thought to add corrections to this space, where more distant neighbours (large $|\vec{A}|$) typically result in smaller corrections. Therefore, the Brillouin zone generalises across all crystals and characterises their state and a sampling of this zone can be provided to machine learning models. This shared feature allows a model to transfer knowledge between crystals, for greater insight. Therefore, it is preferable for a model to operate on the Brillouin zone.

2 Background and Methodology

2.1 Symmetries of Brillouin Zones

Crystalline systems can exhibit many characteristic symmetries in their respective Brillouin zones. Primarily, discrete translational, n -fold rotational, spatial inversion and time-reversal symmetries will be focussed on, as these either lead to the emergent quantum phenomena of interest or constitute important considerations in neural network design.

The custom models will be formulated from the same linear-algebra building blocks as most neural networks, such as affine transformations, their subset known as discrete convolutions, dot-products, and various other tensor operations. Each of these operations has a particular performance optimality when operating on another tensor with a certain representational symmetry. Representational symmetries are defined as symmetries in the arrangement of elements in the tensor or their particular values. However, often in physical symmetries, it is not the value of the particular elements nor how they are arranged which indicates the symmetry, it is instead how the tensor as a whole transforms, such as invariance under a specified operation. In effect, these physical symmetries are found in linear combinations of the tensor's basis rather than

being aligned with just a single element of the basis. This important mismatch can be detrimental when applying common computer vision architectures to physical systems.

Therefore, the primary challenge is to transfer these physical symmetries into representational symmetries, such that the building blocks each function optimally as intended. For example, convolution layers, a subset of affine transforms defined by a sparse-matrix multiplication with repeated localised clusters of tunable parameters, likewise require a repeated local structure in surrounding elements, at a particular scale, to be present across the tensor for it to perform optimally. It is this representational symmetry which n -fold rotational symmetry can be converted into.

2.1.1 Novel Rotational Symmetry Encoding

The global n -fold rotational symmetry is most apparent in the reciprocal space, where the space is invariant under discrete $\frac{2\pi}{n}$ radian rotations of the space about a particular axis, shown in *Eqn. 4*. The discrete convolution operation requires a repeating structure displaced across the image, however, for optimality, this structure should remain in a similar orientation throughout the tensor, whereas the discrete rotational symmetry results in the rotated repeated structure¹.

$$\hat{H}_{ij}(\vec{k}) = \hat{H}_{ij}\left(e^{i\frac{2\pi k}{n}\hat{m}\cdot\vec{X}}\vec{k}\right) \quad (4)$$

With \vec{X} being the special-orthogonal Lie-group generators, \hat{m} the rotation axis and $k \in \mathbb{Z}$.

There are two methods which may leverage this symmetry when using discrete convolution, both are largely equivalent. The two-dimensional discrete convolution [18] is illustrated in *Fig. 1* and denoted as f_K for a particular tunable kernel \mathbf{K} .

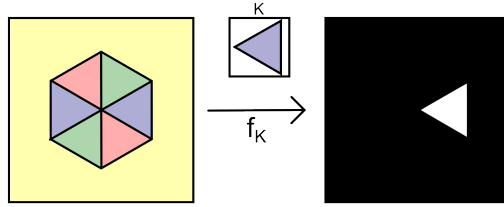


Figure 1: Depiction of how a discrete convolution might emphasise a region which has similarity to the kernel in their representations. The region represents a sampled two-dimensional slice of the Brillouin zone with 2-fold rotational symmetry. However, the convolution has not highlighted the similar rotated structure. This is suboptimal as the kernel cannot be reused; instead, two separate kernels would be required. This slows the network’s learning and produces poorer performance from a lack of generalisation.

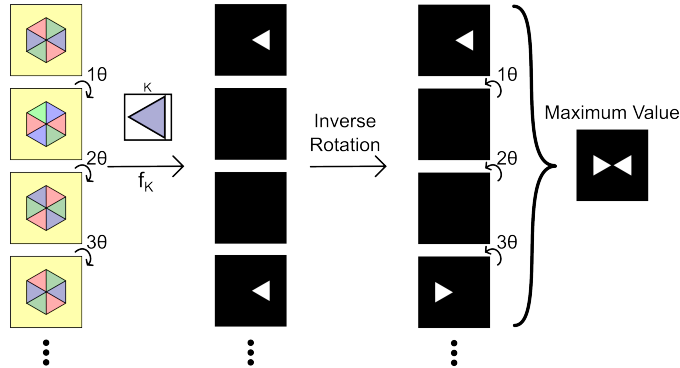


Figure 2: Illustrated is the algorithm for transferring rotational symmetries into translational symmetries, such that the problem is optimal for discrete convolution. Here $\theta = \frac{\pi}{3}$ for clarity, however, it should be considerably smaller in cases where the discrete rotation is present but for an unknown rotation.

The symmetry can then be made representational by adding additional dimensions to the input or the kernel, commonly referred to as adding new channels. These channels are created by concatenating the rotated representation, or appearance, of the kernel by interpolating bilinearly. The rotation angle is θ , defined by $(\theta \ll 2\pi) \cap (\frac{2\pi}{\theta} \in \mathbb{N})$. Equivalently, the input tensor can be rotated instead, making the operation a $(d+1)$ -dimensional convolution as demonstrated in *Fig. 2*. Then convolution can proceed as normal, with the expanded input channels or stacked kernels. The stacked dimension of the resultant tensor should then be inversely rotated by the respective angle. Finally, the maximum value should be taken across this tensor

¹ Unless it also has a corresponding local rotational invariance

axis. It may be desirable to add a depth encoding, to indicate how rotated the similar feature is, analogous to the positional encodings of a transformer [19].

Overall this series of operations make any rotational symmetry more interpretable to the machine-learning algorithm by transferring it into a translational symmetry. Therefore, the network does not need to generate approximate rotated copies of each kernel which would otherwise slow down learning and take priority over other important unique kernels.

2.1.2 Hermitian Symmetry

In the reciprocal space, the Hermitian symmetry ($\hat{H}_{ij} = \hat{H}_{ji}^*$), which ensures physical quantum measurement values due to real eigenvalues, exists already in a representational form due to the transpose. Therefore, no adjustments need to be considered. However, in the real-space hoppings, the hermitian symmetry can be detrimental to performance.

This is because the real-space hoppings follow the relation in *Eqn. 5*. These complex values are equivalent to two real-valued numbers which are the preferred input for deep-learning algorithms. There is a choice in representation between $re^{i\theta}$ and $a + bi$ with $a, b, r \in \mathbb{R}$ and $\theta \in [0, 2\pi]$. The modularity in $\theta \in (\mathbb{R} \bmod 2\pi)$ would have to be applied throughout the network with varying modulus and this would be impractical.

$$\hat{H}_{ij,\vec{A}} = \hat{H}_{ji,-\vec{A}}^* \quad (5)$$

Alternatively, the real and imaginary components can be used. However, any convolution along axis \vec{A} followed by a global operation also along \vec{A} results in a failure when tuning the convolution kernel. This is because the Hermitian symmetry results in the imaginary components forming pairs which sum to zero, this results in parameter updates, shown in *Eqn. 1*, becoming zero and slowing, or even halting, learning.

This risk is easily mitigated by cropping the input to exclude the duplicated information present due to hermitian symmetry. In effect, if hoppings from the \vec{A} neighbouring cell are included then those from $-\vec{A}$ should not be included. Removing this redundant data is highly beneficial in multiple ways. The smaller input requires less memory, less tunable parameters or calculations and therefore faster network training. In addition, the reduction in redundant parameters may encourage the network to pursue a physical understanding of the system, as opposed to an overfitted, shortcuted understanding. This should improve the generality and performance of the model.

2.1.3 Time-Reversal and Spatial-Inversion

The presence of time-reversal or spatial-inversion symmetries, shown in *Eqns. 6* and *7* respectively [20], characterise the type of topological nature of the material when under the appropriate distortion. The properties of these symmetries are explained, and their implications are discussed, in the prior project [7]. It is these symmetries which the machine learning algorithm must model to correctly classify the material's state.

$$H(\vec{k}) = \sigma_y H(-\vec{k})^T \sigma_y \quad (6) \qquad \qquad H(\vec{k}) = PH(-\vec{k})P^{-1} \quad (7)$$

With σ_y being the second Pauli matrix and $P = \text{diag}(\pm 1, \dots, \pm 1)$. Since these symmetries can be pivotal for characterising the state, such as separating Dirac and Weyl semimetal states, the neural network model will be required to interpret these physical symmetries regardless, to achieve good performance. Despite being physical symmetries, they also result in appreciable differences in the representation of the Brillouin zone by relating regions of \vec{k} to $-\vec{k}$. Therefore, no further steps need to be taken to ensure the model can analyse these symmetries optimally.

Further, creating perturbations respecting the time-reversal symmetry and breaking spatial-inversion symmetry scaling with an external parameter λ , enables more varied data to be generated to train the neural network. This has a two-fold advantage. The first is that a larger number of Weyl semimetal states are generated for the dataset, as the gapless region grows with larger $|\lambda|$ [21], therefore, there is a great likelihood that the model will learn the identifying markers of this state. Secondly, dataset expansion prevents the model from overfitting to a simpler task [22], which would be a high-dimensional embedding of a linear regression model. Instead, it must learn to approximate the true physical behaviour of the system to obtain better accuracy on this, more varied, dataset.

The time-reversal symmetric perturbations can be generated for the real-space hoppings using a series of operations on an already hermitian array, denoted $B_{ij\vec{A}}$, as described in *Sec. 2.1.2*. These operations are described in *Eqns. 8 to 11*.

$$\Delta\hat{H}_{ij\vec{A},\uparrow\downarrow} = \frac{1}{2} (B_{ij\vec{A},\uparrow\downarrow} + B_{ij\vec{A},\uparrow\downarrow}^T) \quad (8)$$

Where $\Delta\hat{H}_{ij\vec{A},\uparrow\downarrow}$ denotes the overlap between the central i^{th} orbital spin-up state to the \vec{A} displaced j^{th} orbital spin-down state. This sub-matrix of matrix $\Delta\hat{H}_{ij\vec{A}}$, describes the perturbation, and this sub-matrix is symmetrised.

$$\Delta \hat{H}_{ij\vec{A},\downarrow\uparrow} = \Delta \hat{H}_{ij\vec{A},\uparrow\downarrow}^\dagger \quad (9)$$

Here, *Eqn.* 9 describes copying the transpose-conjugate of $\hat{H}_{ij\vec{A},\uparrow\downarrow}$ to $\hat{H}_{ij\vec{A},\downarrow\uparrow}$. Then *Eqn.* 10 copies the conjugate-transpose hoppings to neighbouring cell \vec{A} to those at $-\vec{A}$.

$$\Delta \hat{H}_{ij-\vec{A}} = \Delta \hat{H}_{ij\vec{A}}^\dagger \quad (10)$$

Finally, the overlap of the spin-up states with spin-up states is made equal to those of the spin-down interaction with other spin-down states in *Eqn.* 11.

$$\Delta \hat{H}_{ij\vec{A},\downarrow\downarrow} = \Delta \hat{H}_{ij\vec{A},\uparrow\uparrow}^* \quad (11)$$

The matrix $\Delta \hat{H}$ should then be normalised by dividing through by the root-mean-squared of all the elements and then multiplying by the external parameter λ . This creates noise, of varying strengths, in the material's atomic-orbital overlaps. These perturbations correspond to various mechanical distortions which can be performed on the crystal and are able to expand the dataset such that the model is encouraged to generalise its understanding to a wider variety of crystalline material environments.

2.1.4 Discrete Translational Symmetry

A pure real-space crystal is characterised by a periodicity in integer multiples, \vec{A} , of the lattice vectors \vec{r} as shown in *Eqn.* 2. For deep-learning models which operate on these hopping coefficients, this periodicity may be leveraged to reduce the required number of tunable parameters.

This results in an assumption that like-atomic orbitals may have similar values, relative to the other orbital hoppings, across the varying displacements of \vec{A} cells. For example, we may expect the hopping of Bismuth $P_{z\uparrow}$ to Tellurium $P_{z\downarrow}$ to be more prominent than Iodine $P_{z\downarrow}$ to Iodine $P_{x\uparrow}$ when the overlap is over any number of neighbouring cells or value of \vec{A} . It is highly likely the overall magnitude of the interaction varies across \vec{A} but there may be some consistency in the relative overlaps over a constant distance $\sum_i A_i \vec{r}_i$. This periodic behaviour in \vec{A} may allow a reduction in tunable kernel parameters as a single kernel can be convolved across all \vec{A} instead of having dedicated parameters for each. This architecture is developed further in *Sec.* 2.4.1.

However, analogous considerations in the reciprocal-space are much more significant; allowing for a universal architecture across many crystalline materials. As previously stated, the Brillouin zone is a resultant finite region, common to all crystals, and defines the particular crystal's electronic behaviour. Making a consistent representation across all possible Brillouin zones enables a neural network to operate upon any given Brillouin zone using the same model. This allows for learnt behaviours from one crystalline system to be reapplied to another. This possibility allows condensed matter models to be applied and trained on a much wider domain, increasing their potential.

The discrete translational symmetry results in corresponding reciprocal space lattice vectors, \vec{b}_i , defined by $\vec{b}_i \cdot \vec{r}_j = 2\pi\delta_{ij}$. These can be used as a consistent way to span the reciprocal-space unit-cell which encompasses the full Brillouin zone for any crystal. For one-dimensional or two-dimensional lattices, $\vec{b}_{2,3} = \vec{0}$ can be used to ensure they are also interpretable by the network. Using the unit-cell approach ensures that no matter the shape of the Brillouin zone, such as a hexagonal prism or cubic, it remains a consistent representation of the network by being contained within the larger parallelepiped cell.

To preserve all information, the conversion from the real-space to reciprocal-space must be injective, which requires n sampling along each reciprocal lattice vector, respecting $n^3 \geq i * j * m$, where m counts all unique combinations of \vec{A} . The sampling can then be performed through a linear combination of the reciprocal space vectors, whilst the discrete translational symmetry can restrict the sampling region to be $a_{1,2,3} \in [-0.5, 0.5]$ for $\sum_i a_i \vec{b}_i$. This also sets the centre of the Brillouin zone, $\vec{k} = \vec{0}$, to be the centre in the representation. The discretely sampled reciprocal unit-cell, $H_{a_1 a_2 a_3 ij}$, is shown in *Eqn.* 12, for $a_k \in (\mathbb{Z} \cap [0, n - 1])$.

$$\hat{H}_{a_1 a_2 a_3 ij} = H_{ij} \left(\sum_{k=1}^3 \frac{(2a_k - n + 1) \vec{b}_k}{2n - 2} \right) \quad (12)$$

Finally, a modification of discrete convolution is discussed in *Sec.* 2.6, which acts to fold opposite edges of the discretely sampled cell, such that the periodicity is represented, in an effective discrete 3-torus space [23]. Whilst the edges or the parallelepiped cell are mapped to the edges of the representation. However, the sampling in *Eqn.* 12 causes a resultant overcounting of the edge samples when folded into a torus, thus a correction is given in *Eqn.* 13.

$$\hat{H}_{a_1 a_2 a_3 ij} = H_{ij} \left(\sum_{k=1}^3 \frac{(2a_k - n) \vec{b}_k}{2n} \right) \quad (13)$$

2.2 Novel Crystalline Material Optimising Through Gradient Descent

Before considering applications of deep-learning to classifying the BiTeI state, an approach of adapting the underlying crystal to exhibit desirable properties is possible through gradient descent. This methodology is applicable to the prior semester's analytical approach, but can also be generalised to systems modelled using deep-learning.

Since the prior analytical approach to calculating tight-binding band structure [7] involved fully differentiable operations, it is possible to perform the gradient descent algorithm, shown in *Eqn. 1*. This allows for the electronic band-structure to be tweaked to a desirable form, and small updates will alter to the hopping coefficients until the system of interest matches the modified band structure. If the algorithm for density functional theory [24] is also made differentiable, this approach can be also used to modify the underlying unit-cell.

However, this has the possibility of producing unphysical results, whereas only modifications which can be achieved through mechanical distortion are desired. A simple technique to achieve this would be to take the original relative coordinates of atoms in the basis, then premultiply these with a tunable matrix $T \in \mathbb{R}^{3 \times 3}$, before passing them to the density-functional-theory algorithm and the tight-binding algorithm. Therefore, by performing gradient descent on T , the crystal can be modified through a physical distortion which results in a close approximation to the desired band structure. Gradient-clipping [25] can also be used for a similar result.

This technique can also be generalised for external effects such as an applied magnetic field and applied to deep-learning classification algorithms for various emergent properties.

2.3 Overview of Fully-Connected Approach

A fully-connected neural network is often considered the simplest deep-learning architecture; it has no particular application and constitutes a series of affine transformations with intermediate non-linear transformations. However, with no express use case, it also does not leverage any symmetries or repeated similarities to optimise its function.

This form of architecture will be used as a control network, to compare with the latter neural networks. Fully connected networks do not constitute one architecture, but instead, a functional class characterised by the number of layers and the number of neurons in each of these layers. These choices are referred to as hyper-parameters or architectural parameters. In *Fig. 3* two fully-connected networks are depicted of different sizes.

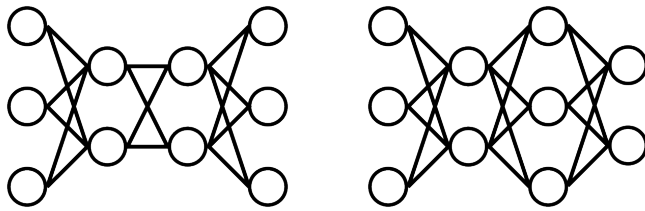


Figure 3: A pictorial representation of two fully connected neural networks, where each node is a neuron, holding activation a , and connection a function $f(x) = \sigma(wa + b)$, where σ is an activation function, and tunable parameters w and b . The particular architectures may be represented as left: [3, 2, 2, 3] and right: [3, 2, 3, 2].

Due to their general scope of application, these networks can be applied to both the real-space $\hat{H}_{ij\vec{A}}$ or sampled reciprocal-space $\hat{H}_{a_1a_2a_3ij}$. For later comparisons, two fully-connected networks for the real-space were constructed. One may be considered a small fully-connected network with structure [17496, 100, 3] and a larger network [17496, 500, 500, 500, 100, 100, 3]. Each layer is interspaced with a Leaky-ReLU activation function $f(x) = \max(0.01x, x)$. These are represented in *Fig. 4*.

In this, and the following models, the number of input hoppings is truncated to the range: $\vec{A} \in \{0, 1, 2\}^3$. This encourages the network to take a physical understanding of the system. With a larger input number, there would be insufficient samples for modelling the nature of the decision boundaries, this problem is known as the curse of dimensionality [27, 28]. This is evident when the number of samples is on the order of the number of inputs. In this scenario, an alternative basis can be constructed where each sample is represented in a single dimension with a value of one, otherwise, its absence is indicated by a zero value, known as one-hot encoding [29]. With this basis, the network can perform a very simple task of placing the respective decision boundaries between zero and one, which is not fulfilling our desired task of understanding a crystalline system. Therefore, by reducing the input dimensions, the model is motivated to learn a realistic method of obtaining its classification.

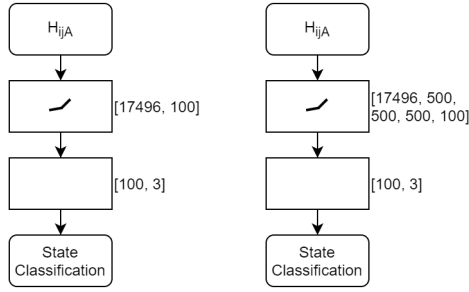


Figure 4: Left diagram depicts the small fully-connected neural network to operate on the real-hoppings, $\hat{H}_{ij\vec{A}}$. Whilst the right diagram shows a much larger network. These networks are drawn using Bird’s convention [26], which will similarly be used for all future network diagrams.

2.4 Overview of Convolutional Architectures

Tuned parameters are trained concurrently, however, with each greater degree of freedom the number of local minima is likely to increase. This may slow, or prevent, the desired learning. In addition, if similar repeated structures occur throughout the input, independent parameters will have to converge on the same configuration multiple times. This is unnecessary, increases the chance of incorrect modelling, and may lead to a reduction in model generality.

Convolutional architectures mitigate these risks by reusing tuned parameters to pick up on these repeated local structures in the tensor representation. They consist of a set of n tunable kernels which are iterated across the tensor and perform a dot product with a localised area. This small area is known as the receptive field of the respective neuron. When the local area has a similarity with the specific kernel, then the resultant dot-product is large and positive. Therefore, convolutions are highly efficient when the representation has these properties, such as in computer vision tasks where similar shapes and textures repeatedly occur.

Due to the discrete translational symmetries of the Brillouin zone, repeated structures are also expressed in the representation, so it will be beneficial to employ convolutional architectures for this task. It is also expected that smaller-scale structures may also be repeated throughout the unit-cell or differing crystals, furthering the use for convolution. Likewise, it can be applied to the assumed approximate translational symmetries throughout \vec{A} in the real-space, since it is the resonances in these values which define the resultant reciprocal-space.

Moreover, multiple convolutional operations can be applied sequentially to the data. This results in an increasingly complex conglomerate kernel operating on the results of prior simpler kernels, allowing for the recognition of progressively intricate patterns. Each component kernel can also compensate for one another in the following dot product, therefore generalising the response for a range of complex patterns. This abstraction enables increasingly complex patterns to be grouped under umbrella categories.

Abstraction is particularly important for condensed matter physics, where a range of similar Brillouin zones, across different crystals, can be grouped under an emergent state. This property is reasonably unique to convolution, whereas a fully-connected layer can be thought of as a basis change without necessarily increasing complexity. In addition, a specific hopping may take a range of values, whilst the crystal remains within a particular state. This variation results in a range of corrections to the Brillouin zone’s shape, which this sequential convolutional structure offers a generalisation to.

It is expected that the reciprocal-space has a range of defining structures across several complexity scales. This is due to the application of the Fourier transform, which indicates the length scale of patterns. It suggests multiple convolutional layers will be advantageous in solving the problem, and is discussed further in Sec. 2.7.

2.4.1 Novel High-Dimensional Hybrid Convolutional Architecture

The real-space hoppings indicate the transition probability from orbital i to j across \vec{A} cell displacements. At any particular constant \vec{A} , the respective matrix elements will have a range of possible structures. It is expected that a linear combination of these structures may persist across further values of \vec{A} , so there may be some form of repeated structure to leverage.

A novel architecture, using the repeated parameter concept of convolutions to increase performance when operating on real-space hoppings, will be demonstrated. However, unlike convolution, no striding of the input occurs. This is because no repeated structure across different hoppings, for constant \vec{A} , is expected to be present since their indexing is arbitrarily assigned when making the matrix. This results in an effective fully-connected network which operates on a matrix \hat{H}_{ij} , which is then reused across all \vec{A} , like a convolution, defining this hybrid approach.

The architecture is defined by kernels of size $K \in \mathbb{R}^{18 \times 18 \times 2}$, which are convolved across dimensions of \vec{A} . However, to detect the potentially multiple structures, it is essential that $1 \ll n$ kernels are used. Most importantly, this mitigates bottlenecks [30, 31] in the architecture, defined as important information being lost due to an insufficient number of

subsequent neurons. Despite this, a small reduction of neurons is desirable to remove any redundant information, so n is chosen to satisfy $1 \ll n < 18 \times 18 \times 2$. Therefore, the first operation in this architecture is shown in *Eqn. 14*, using Einstein's summation convention [32] and a tunable bias parameter $b^{(1)} \in \mathbb{R}^{\vec{A} \times n}$. The summation convention is also used in all the following equations.

$$a_{\vec{A}n}^{(1)} = \hat{H}_{ij\vec{A}} K_{ijn} + b_{\vec{A}n}^{(1)} \quad (14)$$

Since repeated structures were only expected across \vec{A} , only a fully-connected network should follow, as opposed to a further convolution, as it may be detrimental to assume further common structure. Therefore, the tensor $a_{\vec{A}n}^{(1)}$ is multiplied with a weight tensor $w_{\vec{A}nm}$ and summed with a bias vector $b_m^{(2)}$. The number of neurons m is also chosen from $1 \ll m \ll n$, to prevent bottlenecks whilst reducing redundancy. This is shown in *Eqn. 15*.

$$a_m^{(2)} = a_{\vec{A}n}^{(1)} w_{\vec{A}nm} + b_m^{(2)} \quad (15)$$

Finally, a large further fully-connected network operates on the vector of m neurons, completing the network. This architecture differs significantly from others in the literature, so represents a custom neural network purpose-built for condensed matter applications rather than repurposed from another application. It is symbolically depicted in *Fig. 5*, where $n = 256$ and $m = 1024$ were chosen. However, due to operating on the real-space hoppings, where a set of neighbours $\{\vec{A}\}$ are chosen specifically for BiTeI, it generalises poorly to other crystalline systems. Therefore, further architectures are designed to operate on the shared unit-cell of the reciprocal-space.

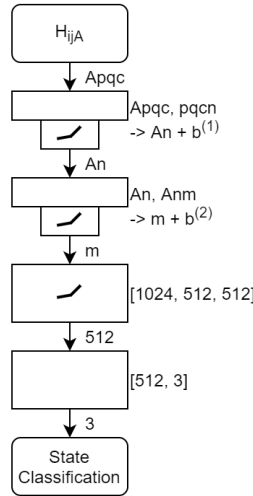


Figure 5: Depicts a novel neural network architecture for predicting material classifications from real-space orbital hopping coefficients. It is purpose-built for BiTeI crystals but can be adapted for other crystalline systems. However, it is likely each model can only be applied to a single system under various mechanical distortions.

2.4.2 Spatial Equivariance and Spatial Invariance

As discussed, the shared parameters of convolutional kernels are useful when there are repeated relations between elements, either along a tensor or throughout different samples of the dataset. This reuse of parameters is attributed to their widespread success. However, it also imparts an approximate spatial equivariance of the representation.

Spatial equivariance of a neural network layer, given in *Eqn. 16*, occurs when a transformation \hat{T} applied to the input \mathbf{X} commutes with the layer f , or the \hat{T} acting on the output is replaced, bijectively, to another transform \hat{T}' . The latter resolves the problematic occurrence of a smaller output tensor, $\text{size}(f(\mathbf{X})) \leq \text{size}(\mathbf{X})$, resulting in trivially non-commuting \hat{T} and f . However, in neural convolutional layers, this is only an approximate equivariance as it generally breaks down near the edges of the tensor. Therefore, only the subspace of central elements have true equivariance.

$$f(\hat{T}\mathbf{X}) = \hat{T}'f(\mathbf{X}) \quad (16)$$

Padding involves surrounding the tensor with constant elements, artificially increasing its size without changing the original information. This has two primary benefits: alleviating the mismatching tensor shapes, such that the stronger $\hat{T} = \hat{T}'$ equivariance is enforced, alongside ensuring all elements contribute evenly to the sum of activations of the following layer. However, the translational equivariance remains solely resolved in the centre of the tensor. In addition, the output's

edges typically have smaller magnitude activations due to the usual constant-zero padding. Both problems compound over sequential convolutions, as the edge effects begin influencing more central activations. Thus, the network is only equivariant under an increasingly small central region. Over many layers, this breaks the equivariance entirely and may contribute to poorer performance in very deep convolutional neural networks [30].

The equivariance of the layer is an important consideration when designing condensed matter neural networks, as significant features are expected to occur across most of the unit-cell. Therefore, any edge effects, whilst negligible in computer vision, may be detrimental when determining the state of the material, if they have differing treatment under convolution. Hence, it is essential that any activations affected by the arbitrary padding, and also the broken edge equivariance, are resolved such that the sub-architecture is fully equivariant².

Furthermore, the network overall needs to be spatially invariant in its representation. This is because the unit-cell can be shifted arbitrarily by any constant vector, whilst the emergent state is invariant to the choice. This is characterised by a global spatial invariance shown in *Eqn. 17*. However, it is not desirable for the convolution layers, or prior layers, to be invariant as this would destroy beneficial information about the spatial arrangement of elements. Consequently, any local structures within the unit-cell would be disrupted and thus, so is the optimality of convolution. Therefore, the proposed network as a whole must be spatially invariant, whilst containing an enclosed equivariant convolution sub-architecture. It is also crucial that this sub-architecture is equivariant, as otherwise a following invariant network cannot be constructed.

$$f(\hat{T}\mathbf{X}) = f(\mathbf{X}) \quad (17)$$

A local spatially invariant function is also desirable to reduce the tensor size in a global equivariant manner. The benefits of shrinking the tensor size include removing redundant information, improving computation times, and increasing the receptive field size for neurons deep into the sequential structure, preferably so it spans the entire input tensor by the final layer. Thus, the whole reciprocal unit-cell is considered when deciding the state. Standard convolution could be utilised to preserve the global equivariance, however, the equivariation of activations would be less predictable with \hat{T}' not resembling the transform of \hat{T} , leading to checkerboard average derivatives [33]. Therefore, convolution layers should always preserve the size of the tensor, requiring convolutional strides to be of length one. Instead, a function with local spatial invariance is needed, fulfilled by a pooling layer [34].

Pooling layers operate upon a local area, much like convolution, however, their operation belongs to the functional class \mathcal{A} , which is defined as any function whose result is invariant under the permutation of elements in the local area, ensuring the lesser spatial invariance. This removes any spatial arrangement information. The resulting layer is quasi-invariant under small shifts but is also globally equivariant. Despite, $\hat{T} \neq \hat{T}'$, the transforms are more comparable than the convolution layer. The functional class also includes functions of the form shown in *Eqn. 18*, with $a_i \in \mathcal{A}$ whilst f_i can be any function. \mathbf{S} is defined as a subspace of $\mathbf{S} \subseteq \mathbf{X}$ representing the localised nature. This stricter definition includes functions such as mean and standard deviation.

$$a_1(\mathbf{S}) = f_1 \left(\sum_i f_2(\mathbf{S}_i, a_2(\mathbf{S})) \right) \quad (18)$$

Furthermore, promoting the localised pooling operation to a global one, thus using the entire tensor, allows information to be extracted from the sequential convolutions whilst ensuring a resultant global spatial invariance - given that the convolutions have a global spatial equivariance. Overall, this novel architecture ensures the physics is unaffected by the choice of the coordinate system, whilst increasing the accuracy of the model. It also helps in maintaining a feasible computing time and memory usage for the model.

Finally, the pooling functional class also includes operations such as sorts, minimums and maximums. Notably, sorting the tensor preserves the intrinsic dimension, maximising the possible information. This can be demonstrated: if $\{a_i\}_{\forall i}$ is a list, such that $a_i \in (-\infty, \infty)$, and this is sorted with the smallest element being $a_0 \in (-\infty, \infty)$, then all greater elements can be re-parameterised as $\{a_0, a_0 + b_1, \dots, a_0 + \sum_j b_j\}$ with $b_i \in [0, \infty)$. Therefore, the spatial arrangement information is lost through a smaller resultant domain after a sort. This is an important way of maximising information, despite using a global pooling operation. Given enough computational resources, the sort followed by a fully-connected layer, to remove redundancy, would be the optimal architecture, however, this is currently computationally inivable. Therefore, a combination of maximum, minimum and averages are used.

Overall, by considering crucial symmetry features of condensed matter systems, and the general coordinate invariance of physics, a functional class has been minimised for possible architectures. This approach results in distinct architectures from the larger literature and defines a set of novel machine learning models purpose-designed to analyse crystalline materials such as BiTeI. It requires an amended convolutional layer, such that it has $\hat{T} = \hat{T}'$ global equivariance, which is then sequentially stacked. Any information is then obtained using global pooling to ensure global spatial invariance. Specific architectures

²The equivariance is intentionally absent in the hybrid network of *Sec. 2.4.1*, due to the kernel not being iterated across the tensor, as we did not expect local repeated structures for constant \tilde{A} .

which fulfil these criteria, and a methodology for proving their resultant invariance, are discussed in the following sections.

2.5 Defining The Problem of Gradient Diffusion

Vanishing and exploding gradients [35, 36] are common problems encountered when designing and training neural network models. Vanishing gradients are defined by progressively smaller gradient updates, tending to zero, for parameters far removed from the output. This results in slower learning progress and a sub-optimal model. It is attributed to the derivative of activation functions tending to zero, known as saturation, given in *Eqn. 19*. It can also occur when the gradient is less than one, such that the updates are scaled down after every layer in a large network. Introducing alternative activation functions [37] or batch normalisation [38] usually resolves the problem. Exploding gradients are characterised by the opposite behaviour of growing, unstable, and diverging gradient updates. It is also remedied by using batch normalisation.

$$\lim_{|x| \rightarrow \infty} \left(\frac{d}{ds} \sigma(s) \Big|_{s=x} \right) = 0 \quad (19)$$

However, the invariant nature of the proposed networks highlights another problem which typically co-occurs with vanishing gradients. We define this as gradient diffusion, characterised by a failure of neural differentiation³, due to gradients becoming quasi-homogenous. We theorise this often occurs in deep neural networks when successive convolutions result in a central limit theorem-like effect for gradient update values, such that neurons all learn to respond similarly as they are provided similar updates.

This is detrimental as it limits the complexity of the resultant network. Due to its association with deep networks, it may be mistakenly considered as vanishing gradients. However, it is not resolved using different activation functions or batch normalisation. It is expected to slow initial learning until a trickle-down effect from later convolution kernels correctly differentiating, begins the differentiation in the next layer. It is expected to be present in nearly every, very deep, machine learning model to date.

This problem is uniquely important when using true global equivariant convolutions with globally invariant information retrieval. For example, if the global pooling operation is chosen to be the mean, then every activation will acquire an equal gradient. This occurs when a gradient is propagated invariantly to an equivariant network, all kernels receive exactly the same update. Hence, there is no trickle-down effect to reduce the problem and the kernels fail to diversify their action. This can be alleviated by using extra, or a better choice of, pooling operations, such as the extended functional class of minimums, maximums and sorting. Despite the invariance of these functions, they result in unevenness in the activation gradients, therefore irregular updates can cause proper neuron differentiation. This is shown in *Eqn. 20*, for three global pools with functions: minimum, maximum and mean. Notationally, δ_i indicates a zero tensor of equal size to \mathbf{X} with an element of value one at index i .

$$d\mathbf{X} = \underbrace{\frac{1}{\text{size}(\mathbf{X})} dP_{mean}}_{\text{homogeneous updates}} + \underbrace{\delta_{\text{argmin}(\mathbf{X})} dP_{min} + \delta_{\text{argmax}(\mathbf{X})} dP_{max}}_{\text{inhomogeneous updates}} \quad (20)$$

The vanishing, exploding, homogeneous and inhomogeneous gradient problems are illustrated in *Fig. 6*.

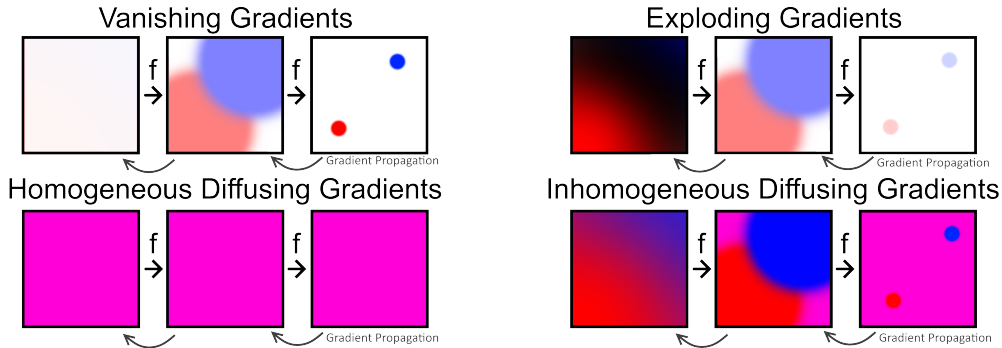


Figure 6: Displays four problems which can result from differing gradient behaviours when using a convolutional layer f . All diagrams depict the diffusing gradient problem. Top-left shows the addition of the vanishing gradient problem, whilst the top-right image shows the exploding gradient problem. If an invariant global average pool is used, it results in the homogenous diffusing problem shown at the bottom-left. The use of maximum and minimum pools results in the slightly improved problem of inhomogeneous gradients shown in the bottom-right. The colours indicate the sign and magnitude of the gradient updates being performed, with each box intended to represent a layer in a sequential convolutional architecture. The gradients are back-propagated from right to left in each series of three boxes.

³In this instance, biological differentiation.

Diffusing gradients is an essential consideration in the network design of Sec. 2.7, as these suffer minimal vanishing gradient effects, but are still prone to gradient diffusion due to the global pooling. Consequently, for the proposed networks, diffusing gradients do not coexist with vanishing gradients, isolating the problem of gradient diffusion for the first time. Therefore these networks highlight that the gradient diffusion problem is a distinct issue, which should be mitigated for network optimality.

2.6 Toroidal Convolutions

The discussion of Sec. 2.4.2 required a hypothetical architecture, containing a global spatial equivariant set of sequential convolutions, with a global spatial invariant method of extracting the information they concentrate. Edge effects were shown to break the equivariance of standard convolution, which then in turn breaks the invariance of the overall network. Therefore, a function with the characteristics of convolution, to optimally detect repeated local structure, whilst removing edge effects is desired.

A straightforward way to achieve this is to, in principle, fold the tensor into an n-torus hence removing any edges to cause edge effects. As a result, the tensor no longer features a centre of its representation, nor any special element, thus ensuring its equivariance. An illustration is shown in Fig. 23 in appendix A. This can be implemented in code by tiling the tensor \mathbf{X} in the desired directions, then cropping the tensor to a standard padding amount, to ensure the original size of \mathbf{X} is maintained when performing discrete convolution over the modified tensor. This is equivalent to folding the representation into an n-torus and the overall operation we name toroidal convolution.

This algorithm is demonstrated for a 2-torus folding of an image in Fig. 7. It can also be equivalently achieved using rolling [39] of the tensor in the desired directions. In either case, it is important to use the discrete sampling of Eqn. 13 to prevent double counting the edge, which would disrupt the equivariance. Also, a stride length as a factor of the tensor length is essential to ensure equivariance, but it is preferable to use a stride length of one and local pooling to reduce the tensor size. Toroidal convolution can be applied in all the same scenarios as typical convolution, such as sequentially stacking layers to yield more abstract observations.

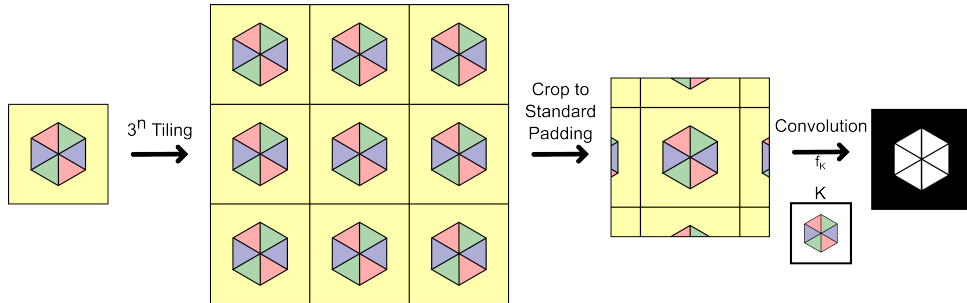


Figure 7: Shows how a standard image, with two flat rectangular spatial dimensions with one colour channel dimension, can be modified such that it behaves as a 2-torus, also retaining one rectangular channel dimension, when convolution is applied.

This is also physically significant as it correctly reproduces the discrete translational symmetry of the crystal. Therefore, it is expected that networks which feature toroidal convolution to have greater accuracy when discerning the emergent state of a material. In effect, these networks are able to represent the full reciprocal-space by using the 3-torus folding of the unit-cell. Sufficient layers should also be used to ensure information across the full space can be integrated into each activation. In combination with the spatially invariant global pooling, it generates an architecture which determines the material state independently of the chosen coordinate system.

Due to the full equivariance of the sequential convolutions, it is expected that applications outside of condensed matter physics may benefit from toroidal convolution. For example, object segmentation in self-driving cars. This is because the camera may not be able to orientate to centre the object of interest, therefore it may benefit from a toroidal convolution which does not suffer from edge effects. In addition, the proposed invariant global pooling will also be advantageous for object detection in similar circumstances. Therefore, these architectures which are purpose-built for crystalline materials, can in turn affect architectures for computer vision tasks.

Variations on the procedure can be implemented, such as an $(n+m+c)$ flat rectangular convolution, converted to an n -toroidal, m -flat rectangular convolution with c channel dimensions. Thus, the periodicity does not need to occur in every spatial dimension, much like the channel dimension treatment. Furthermore, reflections in the tiling procedure can be implemented such that they become n -dimensional analogues of the Möbius strip, which can also be physically significant in condensed matter systems [40, 41].

2.7 Sequential Layer's Activation Complexities

It is expected that the reciprocal-space has defining structures across different length scales. For example, the closing of a bandgap, which can be localised to a single point, defines the difference between insulator-like and conductor-like states. Meanwhile, the topological invariant \mathbb{Z}_2 of a material is a result of the Berry phase [42, 43] which is found through a path integral along the Brillouin zone, so consists of a large-scale structure. It is desirable that the network can interpret these different scale structures, as they are often crucial in determining the state.

Sequential convolutions can fulfil this requirement as each new layer integrates a wider receptive field to construct more complex information. This results in neurons early in the convolutional pipeline responding to smaller-scale, simplistic, but highly specific structures whilst the opposite, larger abstract structures activate neurons deeper into the stack. However, as given by the above examples, it should not be assumed that the only meaningful information is derived from only these larger-scale, most complex, structures. Instead, information from all scales should be accessible to the later invariant sub-network.

There are many possible architectures which fulfil this requirement. However, we will later propose a novel form of neural network that could be much more effective, particularly when considering the physical symmetries of the problem.

2.7.1 Standard Sequential and Residual Models

The vast majority of neural networks, particularly classification networks, can be considered as only sequential models. However, it is possible to partition these into two separate networks with distinct purposes. The first can be defined as an abstraction pipeline, which progressively removes redundancy and integrates wider information into more complex but general patterns, such as the aforementioned convolutional stack. In addition, there is an interpretive network which takes the results of the abstractive pipeline and converts them into a more meaningful form for the experimenter, typically fulfilled by a fully-connected network. In reality, these networks have an overlapping function and present as a seamless structure, but it is convenient in this work to consider them as separate.

In these models, it is assumed that all useful information is contained only within the final results of the pipeline, and it is this information to which the interpretive network has access. Yet, in crystalline state classification, it is expected that important features are distributed throughout the pipeline, due to their associated scales and complexities. Therefore, it could be detrimental to perform further abstracting operations, such as convolution, on this information as it would obfuscate it.

Residual networks [30] mitigate this issue, by adding bypass connections to each operation, which allows less complex information to propagate unhindered to the interpretive network. This results in nested functional classes, with each additional layer expanding the range of possible network functions, with more powerful networks, whilst also keeping the functionality of the prior network. The residual connection is used to recover the identity operation if the alternative operation is not desired, this is because abstraction operations struggle to recreate the identity operation but can easily converge to performing the null operation with the residual performing the identity. Overall, this can be interpreted as each layer performing perturbative corrections to the original input, if beneficial. This is summarised in *Eqn. 21*, where f_i are abstractive operations, with functional class \mathcal{F}_1 nested in \mathcal{F}_2 , as can be seen for $f_2(\mathbf{X}) \rightarrow \mathbf{0}$, which also highlights the perturbative nature.

$$(f_1(\mathbf{X}) + \mathbf{X}) \in \mathcal{F}_1 \subset \mathcal{F}_2 \ni (f_2(f_1(\mathbf{X}) + \mathbf{X}) + f_1(\mathbf{X}) + \mathbf{X}) \quad (21)$$

These networks have had widespread success in computer vision tasks, and it is expected that they offer an improvement in classifying crystalline systems since simplistic features of the reciprocal-space can be interpreted. In *Fig. 8* an architecture alongside its modification to use residual connections is shown. The residual connections do not affect the global equivariance of the pipeline. It is also important, for condensed matter applications that the information is made to be global spatially invariant after the abstraction pipeline. As mentioned, this can be fulfilled by a global pooling layer, per channel.

However, there are also several major drawbacks, which may result in sub-optimal performance, particularly for the classification of crystalline systems.

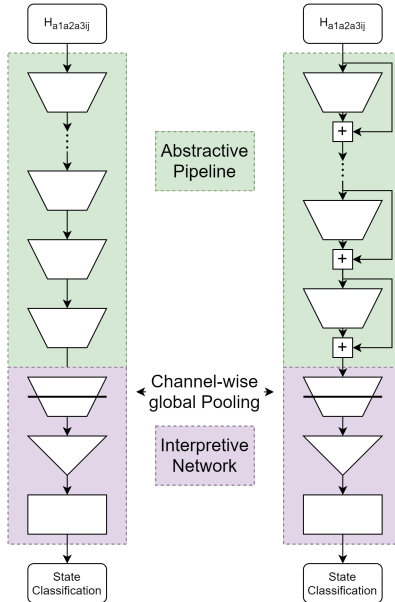


Figure 8: Left shows the standard construction of a sequential convolution model, whilst the right diagram shows the same model with additional residual connections. Each model is segmented into two sub-networks, an abstractive pipeline, in green, and an interpretive network, in purple. The global pooling per channel is also indicated.

2.7.2 Defining Deficits of the Residual Models

Despite residual models being an improvement upon the standard pipeline models, there remain four primary downsides which may severely hamper the classification of crystalline states.

1. Residual networks continue to assume that all useful information originates from a constant complexity level, even if this information stems from an earlier operation.
2. It assumes a common basis for information, throughout the structure, as can be seen by the perturbative correction interpretation.
3. A consistent basis, in turn, requires a consistent size for tensors size ($f_i(\mathbf{X})$) = size (\mathbf{X}).
4. The structure does little to reduce the gradient diffusion problem.

The first deficit is the most crucial for condensed matter networks. As previously discussed, it is expected that important information regarding structures in the crystal’s reciprocal-space is concurrently distributed across multiple layers in the pipeline, reflecting the different scales and complexities of their origin. Despite residual networks assuming important information can occur earlier in the pipeline, it is still assumed that optimal information is only found within only one layer, with all downstream layers bypassed. In effect, it continues to be a standard sequential model but can truncate itself to become a smaller pipeline model, in an optimisable manner. This is further highlighted by the nested functional classes. However, this structure can still not retrieve information from multiple layers at once, as needed for state classification.

Meanwhile, the most far-reaching problem is the assumption of a shared basis. This results from the use of an elementwise-summation in the architecture, where the same indexed elements, per layer, are assumed to represent a common quantity which can therefore be combined together⁴. This is directly contradicting the principle of progressive layers representing increasingly complex and abstract structures. This has fallen into an elementwise fallacy where common-sized tensors encode shared information, which is not true in physical scenarios such as the clear difference between information encoded by electromagnetic field tensors and stress-energy tensors, despite their common size and transform properties.

It is likely that the network will eventually converge on a quasi-common basis, allowing for the desired perturbative corrections, or bypass, but this process is inefficient, restricts the functional class of performing models, and may require significant training time for the convergence. This may also explain the success of batch normalisation, which prevents covariate shifts and brings the two bases into closer alignment for quicker convergence.

This problem can be reinforced by a common oversight when motivating residual networks. It is shown that a neural network struggles to reproduce the identity $h(X) = x$ but can converge on the null operation $h(X) = 0$ with ease. Therefore, the $h(X) = f(X) - x$ trick exploits the unevenness, resulting in a now traded bias towards a resultant identity after the

⁴This is only reasonable when the operations are presupposed to become the identity, but this does not generally apply across all prior layers.

residual connection is recombined. However, this argument crucially admits a contradiction when asserting that $h(X) = f(X) - x$ is then equally easy to converge to as $h(X) = f(X)$, requiring an evenness which the prior argument has already established is invalid. There is evidently an inequivalence in the learnable functions $h(X)$ can adopt. Therefore, it would be expected that the neural network favours an unknown particular span for $h(X)$. This difference in convergence times is established in the original paper [30].

Qualitatively a preference could be posited for $h(X) = f(X)$ as this is what the layer would optimise to when unmanipulated, being a preference for neurons representing increasingly abstract features as opposed to that of a quasi-common perturbative basis for the residual case. Though the former basis would be advantageous to having layers representing distinctly more complex features, assuming a preferred convergence for this is merely an appeal-to-natural behaviour. Overall, the determination of the preferred basis is non-trivial and experimentation should yield further insights.

Overall, this drawback does not outweigh the improvement that residual networks offer upon the standard pipeline models, but there is still certainly scope for further improvement. For example, a concatenation, either direct-sum, *Eqn. 22* showing before and after basis, or tensor-product, *Eqn. 23* likewise showing before and after basis, can combine the information whilst respecting their original basis. The latter form of concatenation may also have significance in representing quantum states since it is also required to correctly represent entanglement. However, it does result in an exponential number of neurons required at each layer, as opposed to a constant growth for direct sum.

$$\{\hat{e}_1, \hat{e}_2\} \oplus \{\hat{e}_1', \hat{e}_2', \hat{e}_3'\} = \{\hat{e}_1, \hat{e}_2, \hat{e}_1', \hat{e}_2', \hat{e}_3'\} \quad (22)$$

$$\{\hat{e}_1, \hat{e}_2\} \otimes \{\hat{e}_1', \hat{e}_2', \hat{e}_3'\} = \{\hat{e}_1\hat{e}_1', \hat{e}_1\hat{e}_2', \hat{e}_1\hat{e}_3', \hat{e}_2\hat{e}_1', \hat{e}_2\hat{e}_2', \hat{e}_2\hat{e}_3'\} \quad (23)$$

A remedy to the previous problem can also be adapted to remove the constraint of a common tensor size throughout the calculation, as highlighted in problem three. In *Sec. 2.4.2*, it was shown that a reduction in tensor size, using a localised global equivariant pooling, would be beneficial. However, in residual models, this requires a step which breaks the nested functional classes. Whenever pooling is performed in a residual model, by definition a residual connection cannot exist between the before and after tensors due to their incompatibility in elementwise summation. Therefore, the pooling is performed without a residual connection, which in turn does not ensure the prior network is in a nested functional class of the extended network with pooling. This is depicted in *Fig. 9*⁵. Allowing pooling, whilst ensuring a nested functional class is a further criterion for both a purpose-built condensed matter network and wider applications in computer vision.

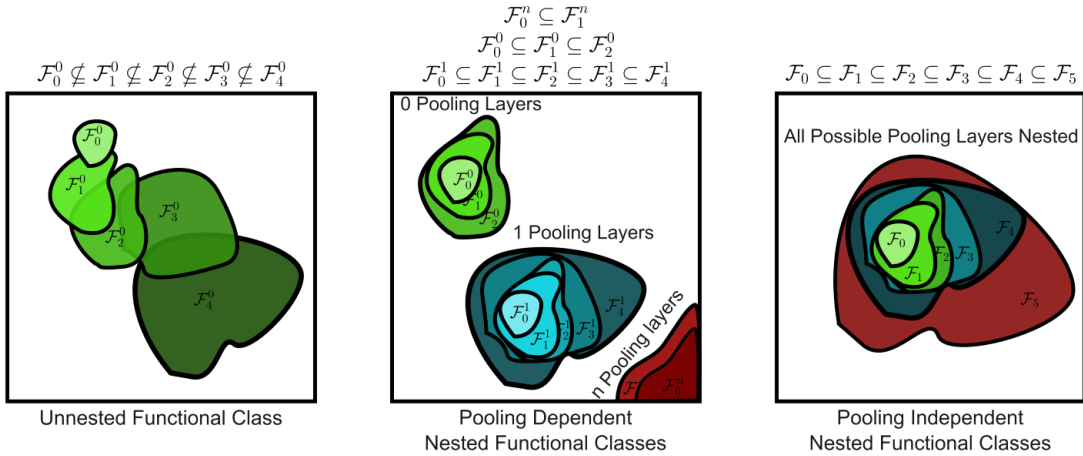


Figure 9: This illustration shows the nature of unnested functional classes (left), pooling dependent nested functional classes (centre) and full nested functional classes (right). The plot is inspired by a prior source [44]. Standard sequential convolution, with varying layers, can be considered as the functional class hierarchy of the left image. The residual network hierarchy is depicted in the central box. Each time a local pooling layer is added, a displaced nested functional class is formed. This is because padding breaks the nesting, due to being unable to reproduce the identity operation. Therefore, if the number of pooling operations is considered on equal footing to the number of convolutional layers, residual networks do not form a nested functional class. A definition of nested function classes, with variable pooling layers, is shown on the right. The upcoming medium extractor of *Sec. 2.8* falls into this definition.

The concatenations of *Eqns. 22*, but not *23* are also shown as a solution to problem four, with mismatching sizes of the original basis. The former concatenation method has already been utilised in both the Dense network [45] and Inception network [46] architectures, however, in both cases, a very large growth occurs in the number of channels, requiring a rapid

⁵Despite being unlikely, technically convolution can reproduce the identity operation making them nested. Therefore, the captioning of *Fig. 9* is incorrect. For this discussion this will be ignored.

reduction in tensor size to make it computationally feasible. In addition, they still require consistent tensor sizes, so only partially resolve problems one and two. Hence, neither is an ideal solution to a nested functional class network.

Finally, residual networks continue to suffer from gradient diffusion. This is because, in their initialisation, they continue to diffuse the gradients at each layer as the residual function takes training time to become the identity operation. The identity operation, by definition, does not compound the gradient diffusion as the jacobian is one-hot, as shown in *Eqn. 24*. So it is expected that this trickle-down effect occurs faster since the network can more easily converge on an identity operation. The convergence may be hastened by using a trainable parameter β such that the residual connection is redefined as $\beta f(\mathbf{X}) + (1 - \beta) \mathbf{X}$ so that only one parameter controls the convergence. However, the bypass only converges in the last few layers, so diffusion still occurs in all layers prior to the bypass beginning. This reduces the problem a little but it is still expected to impede performance. This is also an issue for vanishing and exploding gradients, which are likewise partially mitigated, and present as the original motivation for residual networks [30].

$$\mathcal{J} = \frac{\partial \hat{I}(\mathbf{X}_i)}{\partial \mathbf{X}_j} = \delta_{ij} \quad (24)$$

Overall, an architecture which resolves these weaknesses of residual networks would not only be singularly important for purpose-built condensed matter networks but also may have wider applications in the common domains of deep-learning such as computer vision. In the following section, network architectures of this form are defined.

2.8 The Medium Extractor - A Novel Architecture

A set of architectures is desired that mimics the residual network's nested functional class property, addresses the aforementioned four major drawbacks and is compatible with the earlier full global equivariant of the convolution sub-architecture with global invariance of the whole network. This set of features is made possible through the proposed medium extractor architecture, which is a novel architecture for machine learning and can be applied to problems using arbitrary media, such as the unit-cell, images or spectrograms, whilst extracting information from any complexity level.

Like the residual architecture, activations are drawn out after each abstraction layer, however, unlike residual networks, dense networks and inception networks, it is not recombined later in the pipeline but instead provided directly to the interpretation network in an invariant manner. This is demonstrated in *Fig. 10*. Despite the appearance of a much more complicated structure, its implementation is code is simple and straightforward.

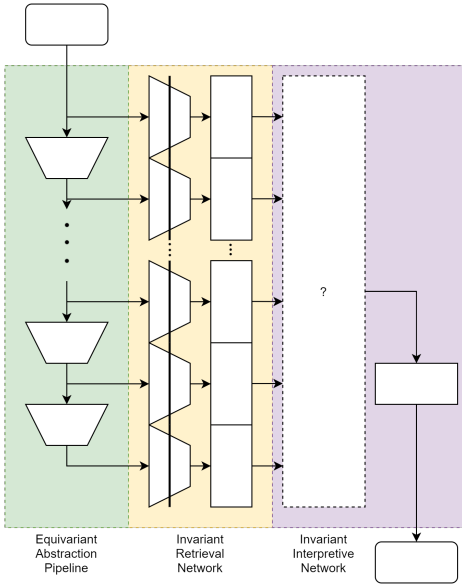


Figure 10: Shows the medium extractor architecture, with an undetermined interpretation network. It features a sequential equivariant convolution pipeline much like predecessor models and can include local pooling following the same structure. Its novelty arises from a global pool, to ensure invariance, applied per channel and per convolution layer. These are then fed into a general function defining a pre-interpretive step, followed by the interpretation network. Applying this network to non-physics tasks may require the removal of the global pooling, as the spatial invariance may not be desirable.

A separate fully-connected architecture is used between the pooling and black-box function for each information read-out, this can be combined into the black-box function using a sparse fully-connected network but is left separate for clarity. However, in either case, it is necessary as a basis transform is needed to convert from the basis used by convolution to another for the black-box function, as it may be sub-optimal to assume a common basis.

The global pooling also helps prevent massive growth in the number of neurons, such as in dense and inception networks, as each global pool retrieves only a vector with a dimension equal to the number of channels of \mathbf{X} , so it does not scale with the, per channel, size of \mathbf{X} . Hence, does not require a rapid reduction in tensor size to make model training attainable.

Alongside this fix, this general architecture meets all the predefined criteria. First, it can be shown to represent a nested functional class of architectures. This can be shown by stepwise recovering a network with one fewer convolutional layers. This is easily demonstrated, by having the fully-connected network corresponding to the last convolutional layer tending to the null operation, which is equivalent to removing the layer. The proof is shown in *Eqn. 25*, which requires direct sum concatenation and also results in a consistent growth in the number of neurons. Using this definition, a standard residual network can be recovered⁶. The nature of nested functional classes also gives a clear definition of model complexity.

$$(0 \times f_2(f_1(\mathbf{X}))) \oplus (\alpha_1 \times f_1(\mathbf{X})) \cong \alpha_1 f_1(\mathbf{X}) \in \mathcal{F}_1 \subset \mathcal{F}_2 \ni (\alpha_2 \times f_2(f_1(\mathbf{X}))) \oplus (\alpha_1 \times f_1(\mathbf{X})) \quad (25)$$

Next, it can simultaneously read out information from any given layer, so it can concurrently understand various scale features of the reciprocal-space. This can be seen by the interpretive network producing non-null operations across multiple readouts, allowing integration of all their respective information. The information from each read-out does not need to pass through any further abstraction operations, so can be directly accessed. This resolves problem one of *Sec. 2.7.2*.

Problems two and three, are satisfied by using a concatenation step, as opposed to elementwise addition, in the black-box function of *Fig. 10*. Since each readout is a vector with a number of dimensions, equal to the channels of \mathbf{X} multiplied by the number of different global pooling operations, they are most generally incompatible with elementwise addition anyway⁷.

Finally, problem four is eliminated, as the network is expected to perform a ground-up training routine rather than a trickle-down one. This is substantially different from all previous network architectures and we would expect very fast progress right from the start of training. In effect, the medium extractor is able to damp outputs from all untrained layers, whilst sending concentrated learning gradients to the earlier layer. Once this is trained, then the next layer up begins receiving meaningful inputs and can then become undamped to receive concentrated gradients and initiate its training. Therefore, the learning of the earliest layers is not rate-limited by the differentiation of the final layers. This sequential training of each layer is a signature of this model and will be confirmed through analysis of the black-box function.

Problem four can be further mitigated by using multiple different functions in the global pooling steps. If the standard global average pooling [47] is used, this continues to result in homogeneous gradients, as discussed in *Sec. 2.5*. However, there is no need to restrict to a single pooling operation, multiple can be used, with their respective vectors direct-sum concatenated together. Therefore, choices such as mean, minimum and maximum would result in inhomogeneous gradients, which is expected to improve performance. These also keep the dimensionality of vectors to scale with the channels of \mathbf{X} , not the size. However, given more computing power, sorting could instead be used which would scale with \mathbf{X} , and would lead to greater inhomogeneous gradients.

In conclusion, this design has all the major features of residual networks whilst correcting its weaknesses. The architecture can also recover a residual network, showing that the residual network's functional class is itself a subset of the medium extractor's⁸.

This architecture marks a significant departure from a standard pipeline design, much like long-short-term memory networks [48] and to some degree transformer architectures [19]. Since it is purpose designed for condensed matter applications, it is expected to have a particularly good performance in this domain, though is proposed to have wide application in many machine learning applications.

2.8.1 Tuned and Free Attention

The transformer architecture benefits from a mathematical attention function, which allows information from different sources to be combined in varying magnitudes, depending on the scenario. This definition can be generalised to the medium extractor model, allowing information from each complexity level to be read out based on its need in determining the current crystalline system's state. This can be incorporated as the black-box function of *Fig. 10*.

The base case is tuned attention, which is static per sample. In effect, the network learns which layers are on average important and emphasises these. This is simply implemented by the black-box function being a direct-sum concatenation of its inputs, then passing them through a fully-connected network. Except through parameter updates, it does not enable live rebalancing of emphasis across the complexity levels in the convolution pipeline for each sample. This simple implementation is displayed in *Fig. 11*. However, it is predicted to perform poorer than dynamically shifting attention. It is still expected that it will perform the signature ground-up training, which should be clear in the fully-connected network's weights.

⁶In its invariant form, otherwise, the global pooling step can be removed to recover its general form.

⁷Unless the fully-connected network unnecessarily reduces them to a consistent size vector.

⁸The medium extractor is also not mutually exclusive with a residual design too, since bypass connections can be added to the convolutional stack. Although there appears little point in doing this as this would reintroduce problems two and three. Though this combination will still be tested, to isolate these problems and show their detrimental effect.

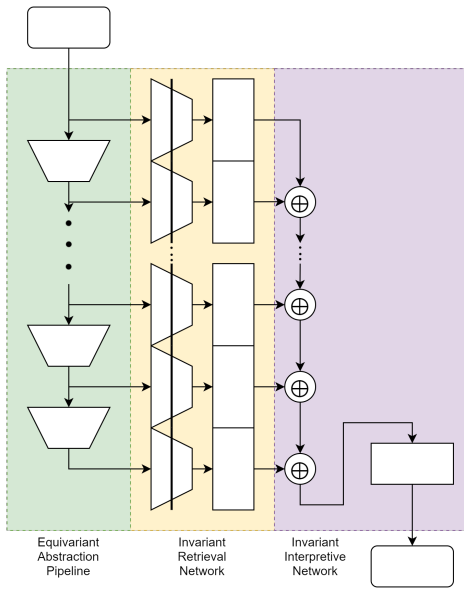


Figure 11: Shows the tuned attention form of the medium extractor. It features a direct sum of each read-out, which is then passed through a fully-connected network. This allows the network to learn which read-outs are more significant and weight these more strongly in its decision-making, such as crystalline state classification.

Free attention is more similar to that seen in transformers, with the network dynamically assigning importance to a particular read-out’s information. First, a similar construction to the tuned medium extractor is needed, but instead of a vector giving the state classification being produced, a vector representing the significance of each layer’s information is formed. Therefore, for n total convolutional and padding operations, this network should have $n + 1$ neurons for each respective read-out.

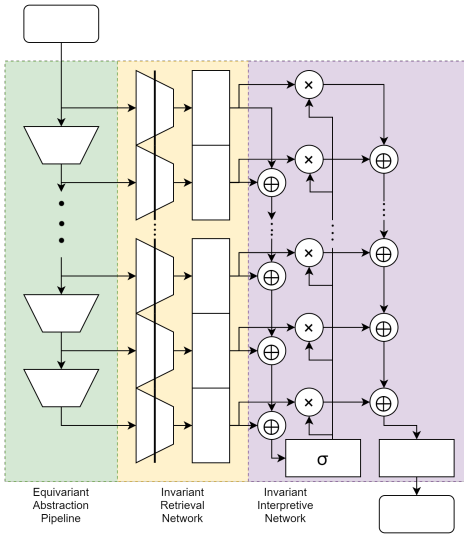


Figure 12: Shows the free attention form of the medium extractor. As opposed to the tuned form, it can dynamically redistribute its attention based on the given sample.

This vector must contain elements in the range $[0, 1]$ and can be normalised or not. Both sigmoid [49], which is unnormalised, and softmax [50], which is normalised, are activation functions that can be applied to this vector to achieve this. The normalised case results in conserved attention, so it must be redistributed across all read-outs when placing emphasis on a particular read-out. In addition, this requires a normalisation of each read-out to ensure the proper functioning of the attention mechanism, otherwise tuned parameters can compensate for the effect. This can, preferably, occur within the sequential convolution stack, or alternatively after the global pooling. Batch normalisation could be used, though this leads to inconsistent equivariance. Instead, normalising each individual tensor may be preferable, to maintain a more constant equivariance.

Each of these attention values then modulates each read-out, before direct-sum concatenating them and passing the

resultant tensor through a fully-connected architecture to determine the crystalline state. This architecture includes an activation non-linearity, due to the modulation interaction, so may benefit from a reduced learning rate to combat chaotic instabilities. This free medium extractor architecture is illustrated in *Fig. 12*. Its code implementation is also uncumbersome.

Overall, this form of neural network incorporates the spatial equivariance and overall invariance needed for representing the discrete symmetry of the reciprocal unit-cell, alongside making its state classification decision based on a range of varying complex structures throughout the unit-cell. Therefore, it constitutes a purpose-built neural network for condensed matter physics, which correctly respects, and leverages, the symmetries of the problem to its benefit. Therefore, compared to repurposed architectures from computer vision, it is expected to have improved accuracy on tasks such as material state classification, critical temperature prediction, and magnetic behaviour prediction, alongside many other crystalline system characteristics. It may also have a wider impact on other deep-learning domains, which should be explored.

2.9 Generating Datasets for Benchmarking on BiTeI

The real-space networks of *Secs. 2.4.1* and *2.3*, are to be evaluated on a dataset of hoppings from the crystal BiTeI. Four emergent states are possible for this crystal under various mechanical distortions: the trivial insulator, topological insulator, Weyl semimetal and Dirac semimetal. The Dirac semimetal only occurs when the crystal is both time-reversal and spatial-inversion symmetric, so in practice, not a single sample will occur in the dataset due to the infinitesimally small chance that sampled hoppings will have both symmetries.

As described in the prior project [7], samples will be interpolated between two instances of BiTeI under different hydrostatic pressures. One at ambient pressure, in a trivial insulating state, with the other at higher pressure, in a topological insulating state. Interpolating between these pressures produces a range of BiTeI configurations in both insulating and Weyl semimetal states, which are identified using the procedures in the prior project. A dataset will be compiled using this procedure.

Circumstances when networks are trained for a few epochs may benefit from a dataset containing an equal number of samples from each state, to avoid network bias. However, this is not necessary for the networks described in this project.

Despite each sample containing many hoppings, even after the truncation described in *Sec. 2.3*, therefore a high extrinsic dimension [7], using interpolation results in an intrinsic dimension of one. This classification of an embedded one-dimensional manifold discourages the network from understanding the physical nature of the system. The addition of noise, described in *Sec. 2.1.3*, increases the intrinsic dimension and another dataset will be assembled based upon this procedure. Again, the classification of these perturbed hoppings will be achieved using the methodology developed in the prior project.

Proving that the perturbations increase the intrinsic dimensionality can be undertaken using singular value decomposition [51] (SVD) of the dataset or visually using t-stochastic neighbour embedding [52,53] (t-SNE). The latter generalises to curved manifolds and is the one used in this experiment. For SVD, the number of non-zero singular values indicates the intrinsic dimensionality, whilst the t-SNE visualisation would show more structure than a line. A more quantitative approach could be achieved using a neural autoencoder [54], with a bottleneck layer with varying numbers of neurons. This would also generalise to curved manifolds with the number of neurons at which the network error drops would indicate the intrinsic dimension. Though this is out-of-scope for this project, as the exact intrinsic dimension is not needed, just the knowledge that it has increased.

The time-reversal and hermitian symmetries of the dataset can also be confirmed, by transforming the respective Hamiltonians and seeing if they are unchanged.

2.10 Sample Rolling of Classical Computer Vision Tasks

Proving the invariance, and thus equivariance, of the network is troublesome using a crystalline system, due to the inherent implementation complexity and very long computation times required. Therefore, to ensure the desired performance it is best to evaluate performance on existing neural network benchmarking datasets. This is made possible due to the cross-compatibility of the proposed condensed matter networks with computer vision problems.

Initial results will be gathered on the MNIST dataset [16] and then confirmed using the more demanding CIFAR10 dataset [17]. In each case the image will be rolled [39] by various amounts, allowing the invariance to be quantitatively deduced. To achieve this, a hyper-parameter, $\chi \in \mathbb{Z}^+$, named the "degree of rolling" is used to produce two uniform random integers, $\omega_x \in [-\chi, \chi]$ and $\omega_y \in [-\chi, \chi]$. The parameter ω_x defines the number of rolls in the horizontal axis, and likewise ω_y in the vertical axis. The procedure, with differing random variables ω drawn per sample and per batch, will be performed throughout the training and evaluation of the networks. Therefore, varying χ indicates the invariance, where the invariant model's accuracy will be unaffected by the change.

MNIST, though quick to train on, is not optimal to infer invariance as it contains large areas of zero-values. This offers a poor distinction between the toroidal convolution and the zero-padded convolution as equivariance is only broken for large χ . Specifically, $20 < \chi \approx 28$, where edge effects begin to occur. CIFAR is better as edge effects occur even for unrolled samples of $\chi = 0$. CIFAR also has a greater variation in object scale and absolute position, much like features in crystalline systems. However, in both cases, the object of interest is still approximately centralised to standardise the dataset. This is unrealistic

to the general applications of toroidal convolution, so an unstandardised dataset such as ImageNet may be the best domain. Unfortunately, due to its size, it is out-of-scope for our computer hardware.

Finally, these images do not feature discrete translational symmetries which define them topologically as a 2-torus. Consequently, a discontinuous border is created when the folding occurs. This does not impede the measurement of equivariance and also has a negligible effect on performance since the network will learn to ignore this feature and the images contain many discontinuous borders regardless.

3 Results & Discussion

3.1 Properties of BiTeI Dataset

Both the unperturbed and perturbed BiTeI datasets were generated with 60000 samples each. These were each partitioned into a training set of 54000 chosen samples and a testing set of 6000 samples, these datasets do not have overlapping samples and every sample is unique. The structure of each dataset is shown in *Tabs.* 1 and 2 respectively.

State Classification	Training Samples	Testing Samples	Total Samples
Trivial Insulator	42613	4697	47310
Topological Insulator	10802	1229	12031
Weyl Semimetal	585	74	659

Table 1: Number of samples representing each material state in the unperturbed dataset

State Classification	Training Samples	Testing Samples	Total Samples
Trivial Insulator	41145	4604	45749
Topological Insulator	10781	1203	11984
Weyl Semimetal	2074	193	2267

Table 2: Number of samples representing each material state in the perturbed dataset.

The number of Weyl semimetal classifications in the perturbed dataset is notably larger. This is in agreement with the expected broadening of the gapless region of the phase space, with a larger magnitude of inversion-symmetry breaking terms in the Hamiltonian [20, 21]. This is also demonstrated in *Fig. 13*, where the minimum bandgap is plotted for interpolated samples, with various magnitudes of noise added.

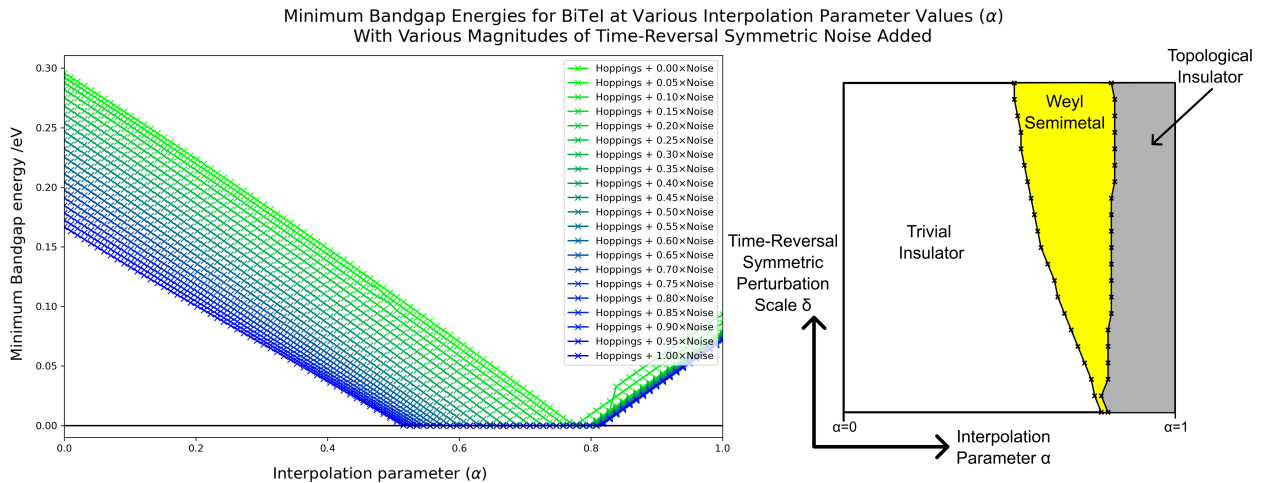


Figure 13: Left shows the minimum bandgap energies of BiTeI along an interpolation line with various magnitudes of noise added: $E_{\min} \left((1 - \alpha) \hat{H}_{\text{Tri.}} + \alpha \hat{H}_{\text{Top.}} + \delta \Delta \hat{H}_{\text{Noise}} \right)$. It can be seen that increasing the magnitude of time-reversal noise increases the range of the gapless Weyl semimetal state. On the right is a recreation of Murakami and Kuga's [21] state space plot, using real data from the BiTeI state boundaries from the left plot. This also demonstrates the broadening of the gapless state range. The noise parameter $\Delta \hat{H}_{\text{Noise}}$ is a constant throughout, with mean $(|\Delta \hat{H}_{\text{Noise}}|) = \text{mean}(|\hat{H}_{\text{Tri.}}|)$.

It was found that the addition of time-reversal symmetric noise successfully increased the intrinsic dimensionality of the dataset, as can be seen in *Fig. 14* and a t-SNE embedding image in *Fig. 24* in appendix B. The noise is also shown to be

symmetric under hermitian and time-reversal transformations in *Fig. 25* of appendix B.

Overall, this analysis has shown that time-reversal symmetric perturbations can be successfully implemented in code and added to the existing interpolated Hamiltonians. This reproduced the expected broadening of the gapless state's range along the interpolation line. In addition, the data manifold's dimension was shown to increase. This ensures that the neural network uses a physical method of solving the problem, as opposed to a shortcut which doesn't learn the nature of the crystalline system. This work enabled the compilation of two very large datasets, with and without these perturbations, for training the neural networks of *Sec. 3.3*.

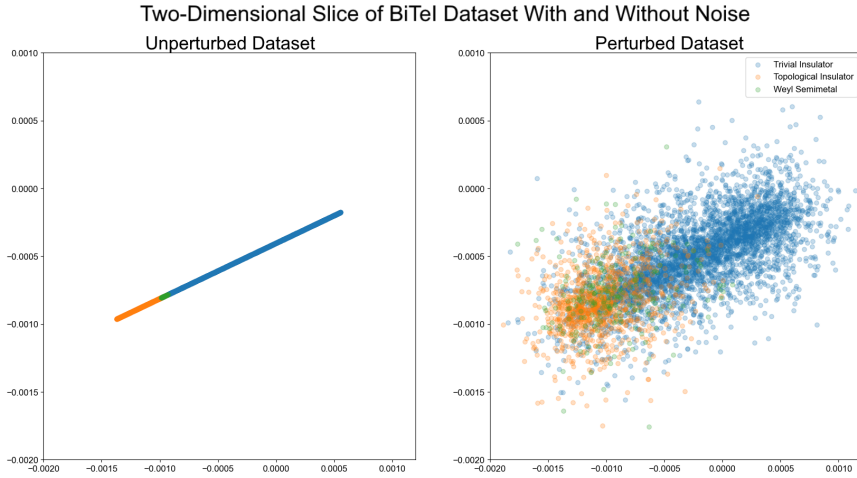


Figure 14: Shows a two-dimensional slice of Hamiltonian samples in the unperturbed (left) and perturbed (right) datasets. It can be seen that the unperturbed dataset is an embedding of a one-dimensional manifold, whereas the perturbed dataset demarcates a high-dimensional manifold's volume. The colour of the sample indicates the crystalline state.

3.2 Evaluation of Invariance on Computer Vision Datasets

Initially, results were gathered on the simpler MNIST dataset to determine if a network architecture is invariant, and if not how much it could approximate invariance. The fully-connected architecture does not have any repeated tuned parameters, so it is not expected to exhibit spatial invariance. This was confirmed in the analysis shown in *Fig. 15*, for networks of structure: small [784, 20, 10], medium [784, 512, 256, 10] and large [784, 525, 525, 525, 525, 525, 525, 10]. All networks are trained using cross-entropy loss [55] and a learning rate of 0.0001, across 10 epochs with 3 repeats, with resampled random initialisations of the networks, for each value of χ .

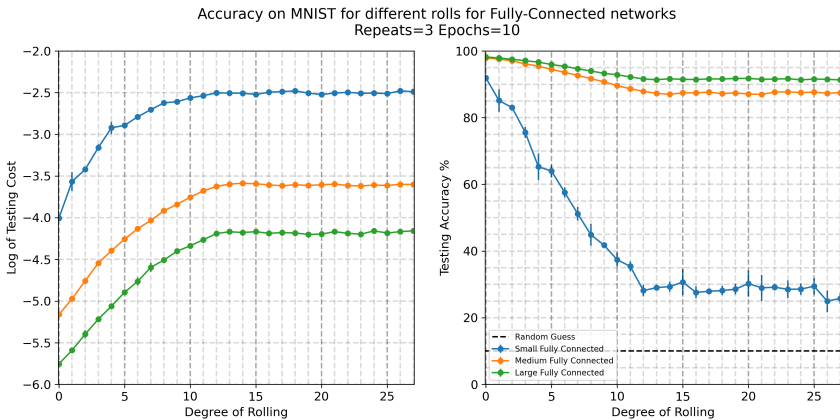


Figure 15: Shows how the performance of a network varies with increasing amounts of sample rolling. On the left is the logged cost whilst on the right is the accuracy on MNIST. Three different fully-connected networks were evaluated with various amounts of neurons. The larger networks are able to learn a better approximate spatial invariance. A total of 252 networks were trained to produce this plot.

The larger fully-connected networks appear to have the capacity to learn an approximate spatial invariance as shown by their higher accuracy at large χ , whilst the small network has the poorest performance. All networks have the highest accuracy at $\chi = 0$, as expected, and appear to stagnate in performance at larger χ . Therefore, using a fully-connected network is undesirable for condensed matter physics, due to its inherent bias towards certain coordinate systems.

In Fig. 16, the effect of reducing the tensor size using local pooling versus convolution was tested, across three variations of the networks.

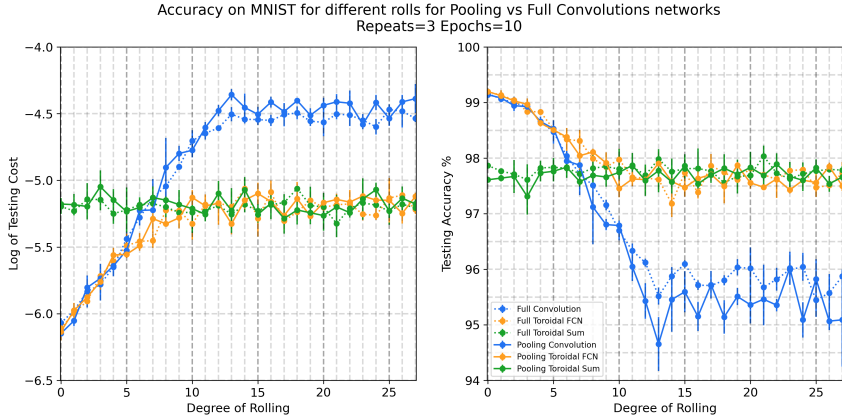


Figure 16: Likewise shows the logged cost (left) and accuracy on MNIST (right) for a range of networks. The architectures are equally structured, with "convolution" being the standard convolution, "ToroidalSUM" being all toroidal convolution layers and "ToroidalFCN" being all toroidal layers except the final one which is standard convolution, which in this case is equivalent to a Fully-Connected Network. The "Sum" suffix indicates the global average pool being used as the final pipeline layer. As expected the convolutional architectures outperform the fully-connected architectures across all χ . The network architectures are displayed in Figs. 26 and 27 of appendix C. Networks prefixed with "Pool" indicates the use of a local pooling operation to reduce tensor shape, whilst "Full" indicates a convolution is used, with stride $\neq 1$ to reduce the tensor shape. These networks have an equal number of trainable parameters and a total of 504 networks were trained to produce this plot.

It was expected that local pooling would be better since \hat{T} resembles \hat{T}' more, but this was not found as both variations resulted in statistically equal accuracy. This indicates that the network can compensate for the variability caused by the trainable convolution layer. Therefore, when constructing the condensed matter network, either can be used, however, we continue to use pooling.

The spatial invariance is clearly present in the Toroidal-Sum network, with performance independent of χ . However, the convolutional and Toroidal-FCN have better performance at small χ , indicating that some breaking of the spatial invariance was advantageous. This may be a result of insufficient convolutional layers used, so not all information from across the input was integrated into the receptive field of the final layer neurons, as well as the gradient dilution problem occurring generally. Overall, the novel Toroidal-FCN appears to be the optimal network but doesn't have the invariance needed for physics.

In the following results, CIFAR10 is used instead of the MNIST datasets, as this harder task provides a better distinction between the network's performances. The epochs are increased to 15, and the learning rate to 5×10^{-5} , due to the increased difficulty of the task. In Fig. 17, the standard pipeline networks are compared to a residual network.

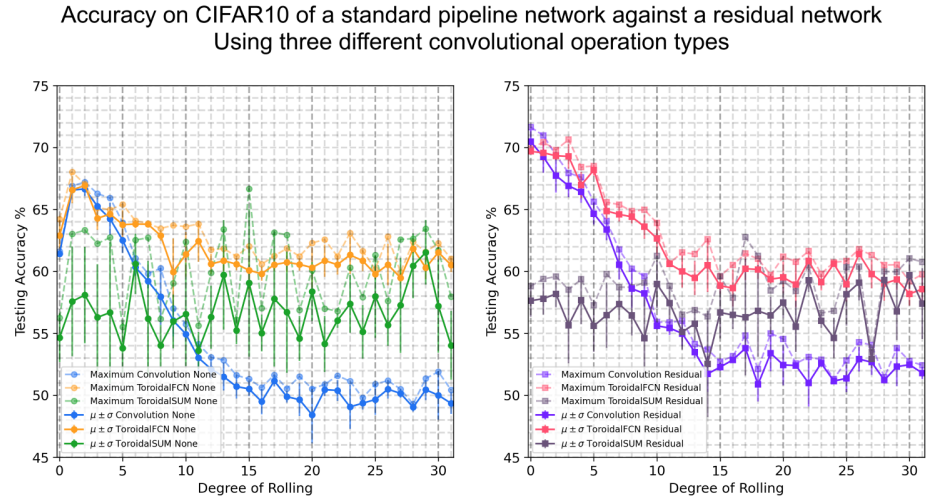


Figure 17: Left shows the accuracy on MNIST for several standard pipeline networks, whilst on the right shows their residual equivalents. An equal number of tuned parameters and kernel sizes are used in all models. The graph displays both the mean accuracy with errors, alongside the maximum accuracy across the three repeats. A total of 576 networks were trained to produce this plot.

Both residual and standard pipeline networks have similar performance except for small χ , where residual networks have a significant improvement. The standard pipeline networks reach a maximum performance $\chi \approx 2$, whilst the residual network has a much higher performance at $\chi = 0$. This is likely for two reasons. The first is that the networks are too deep, for the simplest task at $\chi = 0$, and thus the identity operation is being utilised to bypass the layers, as intended. It also may infer that there is uncertainty in the standardisation, as it is difficult to consistently centre the complex images present in the CIFAR10 dataset. This would explain the rise at $\chi \in \{2, 3\}$, as there exist more samples with the uncertainty in centring. Again, the toroidal-FCN performs the best across all χ , but the convolution is marginally more successful for $\chi = 0$, and the toroidal-sum is consistent with an invariant network. The success of convolution is likely due to the lesser impact of the gradient diffusion problem.

Moreover, the lower overall performance of toroidal-sum is likely a direct result of homogenous gradient diffusion. Therefore, these repurposed computer vision architectures, made to be invariant, appear to be sub-optimal for modelling crystalline systems. The medium extractor resolves this problem and is compared with residual networks in *Fig. 18*

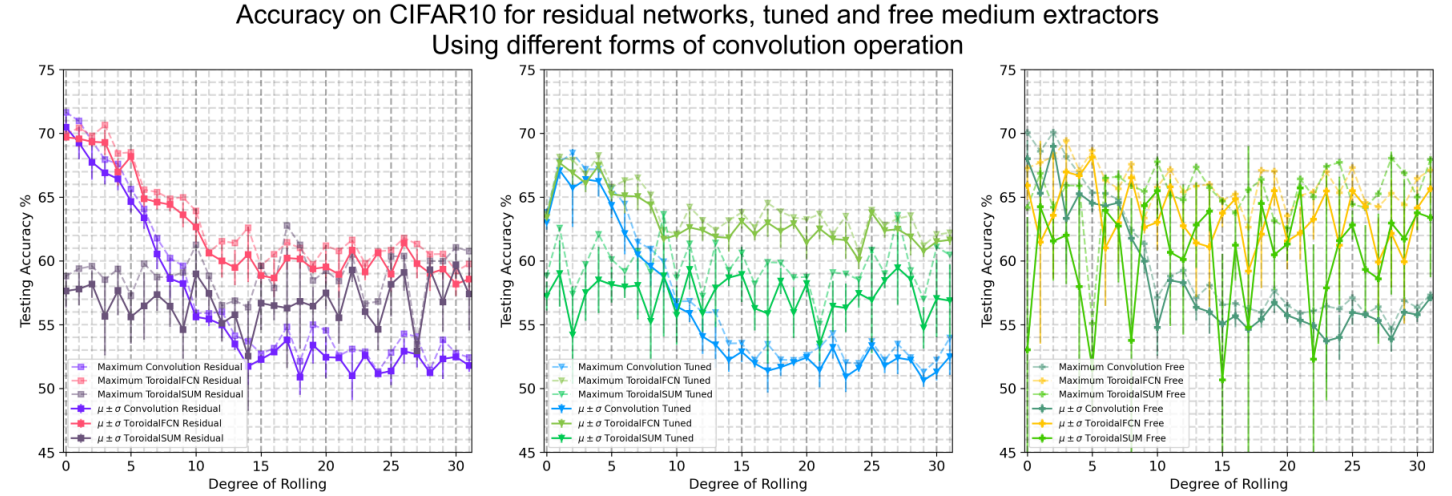


Figure 18: Shows the residual network (left), tuned attention medium extractor (centre) and free attention medium extractor (right), each with a standard convolution, toroidal-FCN convolution and toroidal-sum convolution variant of the abstraction pipeline. An additional 576 networks were trained to produce this plot. Despite the residual network, tuned and free attention medium extractors having the same number of trainable parameters in the abstraction pipeline, the free attention form has additional parameters in the interpretation networks due to its implementation. Therefore, it is important to note that it has a slight advantage, however, this does not account for the vastly improved performance of the toroidal networks. The growth in the interpretation network is also disproportionately small compared to the additional number of read-outs, therefore, the networks should remain comparable.

As before, the convolutional architecture is shown to quickly deteriorate in performance for large χ , whilst toroidal-sum is invariant and toroidal-FCN is the optimum across χ . The tuned medium extractor slightly outperforms the residual network for large χ but continues to have poorer performance for smaller degrees of rolling. This is likely due to over-abstraction and a failure of the tuned medium extractor to bypass the final layers. Though it appears the mechanism functioned as intended for larger χ since a greater performance is observed. This suggests that there is a benefit in withdrawing information from multiple layers concurrently, confirming the first problem proposed in *Sec. 2.7.2*.

The free attention medium extractor is successful across all χ , particularly for the toroidal-sum variant. This confirms that there is a large benefit in dynamically allocating attention across the various convolutional layers. In contrast with the tuned medium extractor, it indicates that each sample has important information occurring across convolution layers, but the particular layers are dependent on each sample. The common dip around $\chi = 0$ is also absent, indicating that the network successfully bypasses redundant convolution layers much like the residual network, inferring it correctly formed a nested functional class. In comparison to the tuned-attention case, it suggests that the need to bypass particular layers fluctuates with the sample, explaining the poorer performance of the tuned-attention model. The free-attention model does feature some instabilities, likely due to the activation non-linearity. A lowered learning rate should alleviate this problem, however, the primary cause is later found to be the attention mechanism.

Overall, the free attention medium extractor appears to parallel the success of the residual model for smaller χ , with growing benefits for larger χ . This implies it will be highly successful in real-world uncentered problems. Testing on ImageNet is needed to confirm this. This is an early indication that custom machine-learning algorithms for condensed matter systems are particularly successful. However, the highest performance overall was observed for the high-bandwidth medium extractors shown in *Fig. 19*.

The term "high bandwidth" is used to refer to multiple forms of global pooling being used. Namely, mean, maximum and minimum global poolings were used per layer, with the respective vectors direct-sum concatenated. This architecture

Accuracy on CIFAR10 for free and high bandwidth free medium extractors
Using different forms of convolution

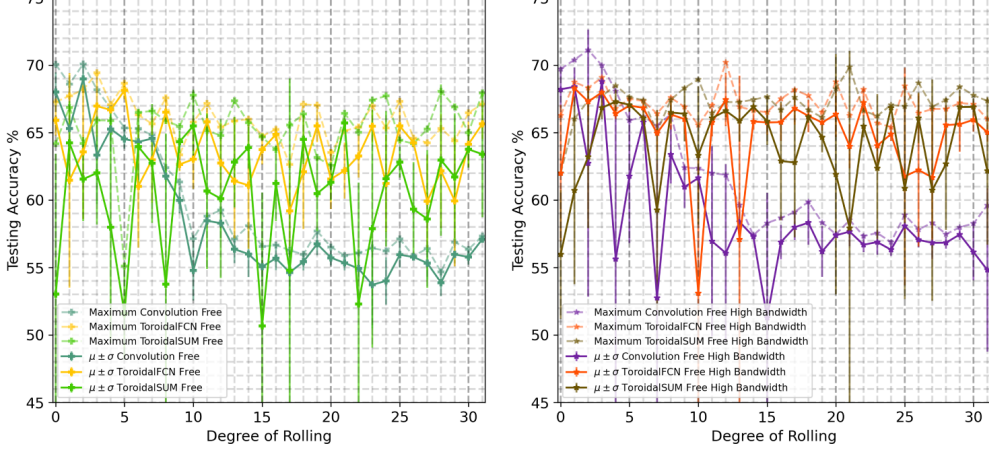


Figure 19: The standard free-medium extractor is shown on the left, using only global mean pooling, whilst the high bandwidth free medium extractor is on the right. This latter network uses mean, maximum and minimum global pools per channel per layer. An additional 288 networks were generated for this plot.

is particularly significant as it isolates the gradient diffusion problem. The greater accuracy achieved by this network corroborates the existence of the problem, as both vanishing and exploding gradients are mitigated by the use of Leaky-ReLU, batch-normalisation and dynamic attention forming a nested functional class. Reduced bottlenecking may also factor into the improvement, however, this does not explain the equalisation between the toroidal-sum and toroidal-FCN networks. Due to the toroidal-FCN containing an invariance-breaking layer, only inhomogeneous gradient diffusion occurs across its architectures. Yet inhomogeneity only occurs for toroidal-sum in the high bandwidth case. Therefore, their indistinguishable performance in the high bandwidth case, suggests it is a direct result of, particularly the homogeneous, gradient diffusion being alleviated. Although homogeneous and inhomogeneous gradient diffusion is also generally resolved by the attention mechanism. Therefore, the discrepancy in accuracy experimentally validates the presence of this problem. Consequently, this problem should always be considered in the development of spatially invariant networks, such as those required in physics applications.

Finally, the existence of problems two, and by consequence three, of Sec. 2.7.2 can be established using a hybrid architecture between residual networks and high bandwidth free attention medium extractors. The hybrid network consists of the medium extractor with residual bypass connections. This architecture selectively reintroduces these two problems, so a drop in performance would directly infer their presence. This is observed in Fig. 20.

Accuracy on CIFAR10 for residual networks, hybrid-residual high bandwidth medium extractors and standard high bandwidth medium extractors
Using different forms of convolution

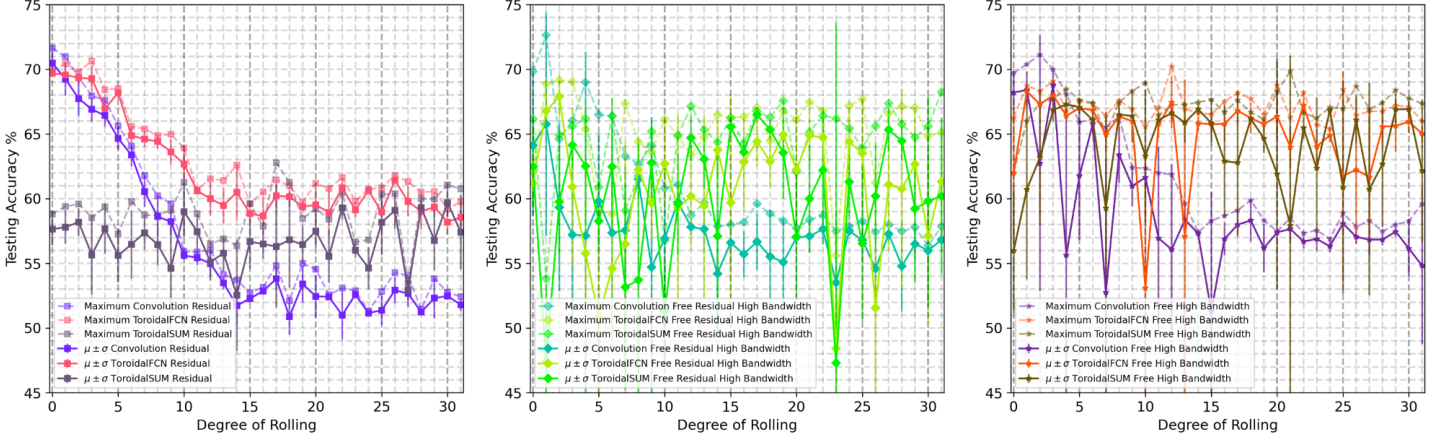


Figure 20: Shows network performance of residual networks (left), hybrid high bandwidth residual free medium extractors (centre) and high bandwidth free medium extractors (right). The hybrid network is shown to have performance between the residual network and high bandwidth network, indicating that the suggested four deficits of residual networks are correct assertions.

The sandwiched performance of the hybrid network not only directly confirms the existence of deficits two and three of residual networks, but also infers problems one and four, as the standard high bandwidth medium extractor is shown to have

generally greater performance over the standard residual network across all $\chi > 0$. This is further corroborated by *Fig. 21* showing the performances of the toroidal-sum networks collated for all χ and across all architectures.

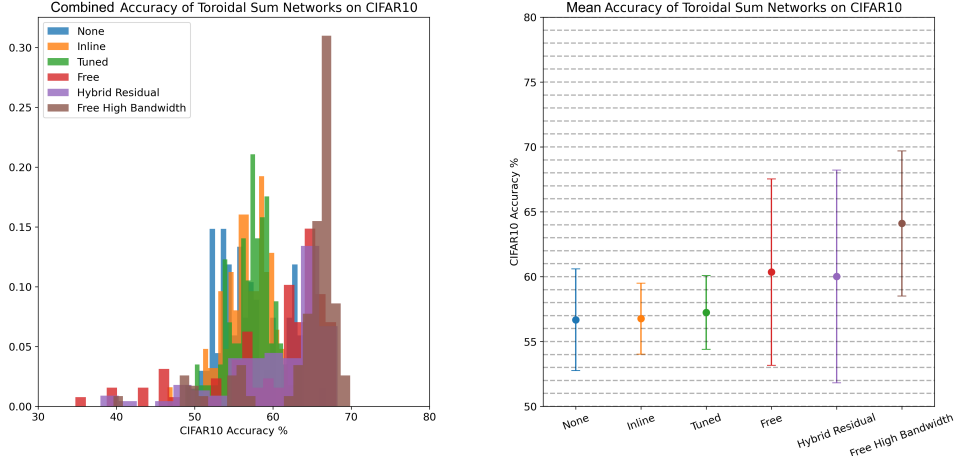


Figure 21: Shows the combined accuracies of toroidal-sum architectures across all χ . It indicates that the high bandwidth, free attention model is the optimal network for spatial invariance. The improvement of the medium extractors over the prior models helps confirm the deficits proposed in *Sec. 2.7.2*. Inline is used synonymously with residual. In addition, the best performances reached by the medium extractors infer the existence of the gradient diffusion problem.

As expected, the dynamic attention signature of progressing up increasing layers was observed during training, confirming the ground-up learning behaviour. This is shown in *Fig. 22*.

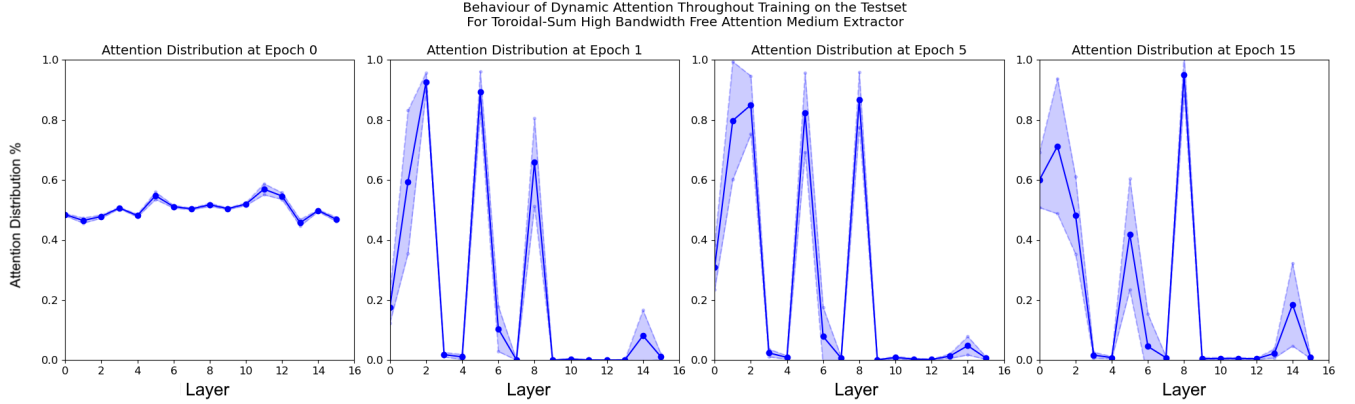


Figure 22: Shows the mean and standard deviation of attention distribution across 1250 samples of the test set, at various epochs along the training process. The results are from the high bandwidth, free attention, toroidal-sum medium extractor. It shows that before training, epoch=0, the attention is evenly distributed, it then redistributes to prioritise early layers. Once these are trained, their attention is damped whilst the next layer becomes undamped. This behaviour then progresses. It can be seen that layers 2, 5, 8 and 14, appear to have particularly important information consistently, indicating these scales have significant structures in this problem. The error bars indicate the standard deviation of attention across the samples.

It was also found that the prior instability is primarily a result of the common sigmoid saturation, as shown in *Fig. 28* in appendix D. In effect, layers are permanently damped to zero, detrimentally affecting performance. This is alleviated by a rescaling of the attention as $\epsilon + (1 - \epsilon) \sigma(x)$ for $0 \leq \epsilon \ll 1$ and sigmoid activation $\sigma(x)$, to ensure attention always remains non-zero. Preliminary results indicate this is a successful remedy, but there was insufficient time for extensive testing. The results of all networks, evaluated on the CIFAR10 dataset, are collated in *Fig. 29* in appendix D.

Therefore, it can be concluded that the high bandwidth, free attention medium extractor, using a full toroidal convolution abstraction pipeline, is the best architecture for predicting the properties of crystalline systems. Residual networks, without invariance, still have a good performance on highly standardised tasks but the broken invariance is sub-optimal for condensed matter problems. This indicates that a custom neural network approach to modelling crystalline systems is highly effective and significantly outperforms repurposed computer-vision-originating designs. It also suggests these models may have widespread implications for standard machine learning domains, however, more testing, such as on ImageNet, is required to determine whether they are truly state-of-the-art. The problems proposed earlier in the project were also isolated to confirm their existence and demonstrate the detriment. This may also have a wider impact on other domains of machine learning.

3.3 Machine Learning applied to Condensed Matter Physics

Finally, the accuracy of network architectures developed in *Secs.* 2.3 and 2.4.1 are benchmarked using the datasets developed in *Sec.* 3.1. The results for the unperturbed dataset are tabulated as confusion matrices in *Tabs.* 3 through 5. Each data point represents ten repeats of identical architectures with different initialisation, trained over 25 epochs. The average and uncertainty of each network's accuracy over these ten repeats are displayed.

		Training Set Classification (%)			Testing Set Classification (%)		
		Trivial	Topological	Weyl SM.	Trivial	Topological	Weyl SM.
Small Fully Connected Prediction	Trivial Topological Weyl SM.	100.0 \pm 0.1	0.0 \pm 0.0	47.1 \pm 29.4	100.0 \pm 0.1	0.0 \pm 0.0	55.5 \pm 29.1
		0.0 \pm 0.1	99.7 \pm 0.5	43.4 \pm 31.7	0.0 \pm 0.1	99.6 \pm 0.8	34.5 \pm 30.5
		0.0 \pm 0.0	0.3 \pm 0.5	9.5 \pm 10.5	0.0 \pm 0.0	0.4 \pm 0.8	10.0 \pm 10.6

Table 3: Confusion matrices for accuracy of the small fully connected network presented in *Sec.* 2.3 on the unperturbed training and testing dataset of *Sec.* 3.1.

		Training Set Classification (%)			Testing Set Classification (%)		
		Trivial	Topological	Weyl SM.	Trivial	Topological	Weyl SM.
Large Fully Connected Prediction	Trivial Topological Weyl SM.	99.7 \pm 0.7	0.5 \pm 1.3	36.3 \pm 42.3	99.7 \pm 0.7	0.7 \pm 1.9	38.2 \pm 42.9
		0.1 \pm 0.3	97.6 \pm 3.4	24.1 \pm 32.3	0.1 \pm 0.2	96.9 \pm 4.2	21.8 \pm 31.1
		0.2 \pm 0.4	1.9 \pm 2.4	39.7 \pm 33.5	0.2 \pm 0.5	2.4 \pm 3.0	40.0 \pm 34.6

Table 4: Confusion matrices for accuracy of the large fully connected network presented in *Sec.* 2.3 on the unperturbed training and testing dataset of *Sec.* 3.1.

		Training Set Classification (%)			Testing Set Classification (%)		
		Trivial	Topological	Weyl SM.	Trivial	Topological	Weyl SM.
Novel Convolution Prediction	Trivial Topological Weyl SM.	99.7 \pm 0.4	0.7 \pm 2.0	29.5 \pm 37.6	99.8 \pm 0.3	1.0 \pm 2.6	32.6 \pm 37.9
		0.0 \pm 0.1	98.8 \pm 2.6	34.8 \pm 43.3	0.0 \pm 0.1	98.4 \pm 3.2	33.8 \pm 43.4
		0.2 \pm 0.4	0.5 \pm 0.7	35.7 \pm 35.6	0.2 \pm 0.3	0.6 \pm 0.9	33.6 \pm 33.9

Table 5: Confusion matrices for accuracy of the novel convolutional architecture presented in *Sec.* 2.4.1 on the unperturbed training and testing dataset of *Sec.* 3.1.

It can be seen that the small fully connected network performs the worst, likely due to insufficient parameters to correctly model the behaviour. Whilst both the large fully connected and novel convolution models had comparable accuracy, likely due to it being an embedding of the problem of classifying a one-dimensional line. Similar performance is also seen between the testing and training sets across all models, indicating that overfitting did not become a problem in the modelling.

The Weyl semimetal state was most often misclassified, particularly as a trivial insulator. This reflects the underlying proportions of the dataset, with trivial insulators being the most common example. This could be improved in three ways: using an alternative cost, resampling the dataset and longer training times.

The cost function used to train these networks effectively tries to improve the overall accuracy of the network, this gives a bias towards predictions classifying a material as a trivial or topological insulator. Instead, a cost function can be constructed to maximise the trace of these confusion matrices. Therefore, it prioritises correct classification even for samples which are underrepresented in the dataset, such as the Weyl semimetal.

Resampling the dataset, to include equal samples of each classification could also be performed, however, this is not ideal. Since the true classification is calculated independently for every sample, it is not possible to guess which classification it will become ahead of analysis⁹. Therefore, resampling the dataset would involve only removing information which is undesirable, as typically a larger dataset should always be prioritised.

Finally, longer training times would likely resolve the poor performance on Weyl semimetals. This is because the other two classifications have nearly 100% accuracy, therefore, the only way to continue to reduce the cost is to begin classifying Weyl semimetals correctly.

The corresponding confusion matrices for the same networks, but trained on the perturbed dataset, are shown in *Tabs.* 6 through 8.

⁹It is possible to predict the classification for the unperturbed samples, as boundaries α_1 and α_2 were found to suitably distinguish the states in the previous project [7]. However, this does not generalise to the perturbed dataset.

		Training Set Classification (%)			Testing Set Classification (%)		
		Trivial	Topological	Weyl SM.	Trivial	Topological	Weyl SM.
Small Fully Connected Prediction	Trivial Topological Weyl SM.	94.3 ± 0.9 5.7 ± 0.9 0.0 ± 0.0	25.3 ± 3.5 74.7 ± 3.5 0.0 ± 0.0	50.2 ± 8.2 49.8 ± 8.2 0.0 ± 0.0	95.8 ± 0.9 4.2 ± 0.9 0.0 ± 0.0	17.2 ± 3.6 82.8 ± 3.6 0.0 ± 0.0	52.2 ± 9.1 47.8 ± 9.1 0.0 ± 0.0

Table 6: Confusion matrices for accuracy of the small fully connected network presented in *Sec. 2.3* on the perturbed training and testing dataset of *Sec. 3.1*.

		Training Set Classification (%)			Testing Set Classification (%)		
		Trivial	Topological	Weyl SM.	Trivial	Topological	Weyl SM.
Large Fully Connected Prediction	Trivial Topological Weyl SM.	94.0 ± 1.3 6.0 ± 1.3 0.0 ± 0.0	24.1 ± 4.3 75.9 ± 4.3 0.0 ± 0.0	47.7 ± 10.4 52.3 ± 10.4 0.0 ± 0.0	95.4 ± 1.4 4.6 ± 1.4 0.0 ± 0.0	16.4 ± 4.2 83.6 ± 4.2 0.0 ± 0.0	49.3 ± 11.6 50.7 ± 11.6 0.0 ± 0.0

Table 7: Confusion matrices for accuracy of the large fully connected network presented in *Sec. 2.3* on the perturbed training and testing dataset of *Sec. 3.1*.

		Training Set Classification (%)			Testing Set Classification (%)		
		Trivial	Topological	Weyl SM.	Trivial	Topological	Weyl SM.
Novel Convolutional Prediction	Trivial Topological Weyl SM.	93.7 ± 1.3 6.3 ± 1.3 0.0 ± 0.0	23.7 ± 4.1 76.3 ± 4.1 0.0 ± 0.0	46.0 ± 9.2 54.0 ± 9.2 0.0 ± 0.0	95.2 ± 1.4 4.8 ± 1.4 0.0 ± 0.0	15.6 ± 3.9 84.4 ± 3.9 0.0 ± 0.0	47.7 ± 11.2 52.3 ± 11.2 0.0 ± 0.0

Table 8: Confusion matrices for accuracy of the novel convolutional architecture presented in *Sec. 2.4.1* on the perturbed training and testing dataset of *Sec. 3.1*.

Using this dataset, the accuracies are shown to reduce across all classifications compared to the unperturbed dataset. This is unsurprising due to the increased difficulty of the problem, as the network has to fit non-linear physical boundaries compared to the previous linear unphysical boundaries.

The trace of the testing confusion matrices are 178.6 ± 3.7 , 179.0 ± 4.4 , and 179.6 ± 4.1 for the small fully connected, large fully connected and novel convolutional networks respectively. Therefore, it suggests that the novel convolutional network is marginally better, but this is not a significant result. In all cases, the Weyl semimetal was entirely misclassified, and the network did not classify a single sample as a Weyl semimetal. This is likely primarily due to the poor choice of the cost function. Given more time, the three aforementioned methods to mitigate poor performance could be implemented.

However, the results showed that performance on the unperturbed dataset is misleading and does not reflect the network's true performance on general crystalline state classification. It is indicative of the network using a probabilistic shortcut to achieve higher accuracy, rather than having a physical understanding of the material. Therefore, in future testing, it is important to use a varied dataset, with as high as possible intrinsic dimension, to ensure an accurate benchmarking of the models is achieved.

Overall, there was some success in correctly classifying the trivial and topological states for a mechanically distorted bismuth-telluride-iodide crystal from their real space orbital overlap data. However, more fruitful results are expected from a universal network operating upon the reciprocal unit-cell. Using the latter form of input, the various forms of medium extractors can be applied with better-expected results. In addition, it would allow a universality to the modelling, where any crystal under any distortion can be inputted, which is not possible using the highly specific real-space hoppings. It is also expected that these architectures will generalise well in predicting any material property associated with the electronic band structure. Due to time constraints, these further applications could not be explored but will be in follow-up work.

4 Conclusion

The primary goal of developing a custom machine learning approach to condensed matter physics was achieved, using a multitude of methods. A novel convolutional design was developed to analyse the orbital overlaps of a BiTeI crystal, to determine its state classification. This approach had success at distinguishing trivial and topological insulators, under a range of mechanical distortions. Performing this classification required a benchmarking dataset to be developed on a well-understood crystalline system, which BiTeI fulfilled. Time-reversal symmetric perturbations were successfully added to the Hamiltonian. This expanded the range of conditions to which this machine learning model could be applied, and some success was seen in the resultant classifications. Although, further work is needed to improve its classification of semimetallic states. A gradient descent method of fine-tuning the distortions applied to crystals to yield useful behaviours, was also outlined.

Moreover, a review of several deep-learning techniques identified and defined several problems which arise in common architectures, including broken equivariance and invariance of convolutional layers, the homogenous and inhomogeneous gradient diffusion problems, four deficits of residual networks and the broken nesting caused by pooling operations. Each of these was isolated and proven to be detrimental to the network trained on a standardised dataset. The resolution of these problems was crucial for progress in a machine learning architecture, custom designed for modelling crystalline systems.

This architecture was shown to be universally applicable to all crystalline systems, by performing analysis on the reciprocal-space such as the electronic band structure of the valence and conductive bands. It is expected that this network will have a good performance in predicting many properties of crystalline systems. Preliminary results also indicated that the spatial invariant forms of this architecture were highly successful, and may be better suited to condensed matter physics than the repurposed computer-vision architectures. These new architectures are very distinct when compared to other approaches found in the literature. Unfortunately, there was insufficient time to both compile a dataset for the reciprocal-space application and train the newly developed machine learning models, due to several key developments arising only in the final stages of the project. Further testing is also needed to determine whether there is widespread applicability of these architectures in the most common domains of machine learning, such as computer vision. We propose that extensive analysis of the models on the ImageNet dataset may be most appropriate.

Overall, this project was a resounding success, with nine problems newly identified, proven and resolved, one novel technique for fine-tuning mechanical distortions applied to crystalline systems, one novel technique of transferring physical symmetries into representational symmetries, a novel technique for analysing spatial invariance, and sixteen new architectures developed purposely for condensed matter physics. It is hoped that this work will generate further avenues of research to explore and experimentally validate, alongside applications of the methods to determine the properties of condensed matter systems with increased accuracy and with the appropriate physical symmetries considered.

References

- [1] A. S. Fuhr and B. G. Sumpter, “Deep generative models for materials discovery and machine learning-accelerated innovation,” *Frontiers in Materials*, vol. 9, 2022.
- [2] C. Yue, S. Jiang, H. Zhu, L. Chen, Q. Sun, and D. W. Zhang, “Device applications of synthetic topological insulator nanostructures,” *Electronics*, vol. 7, no. 10, 2018.
- [3] M. He, H. Sun, and Q. L. He, “Topological insulator: Spintronics and quantum computations,” *Frontiers of Physics*, vol. 14, p. 43401, May 2019.
- [4] X. Liu, Y. Si, K. Li, Y. Xu, Z. Zhao, C. Li, Y. Fu, and D. Li, “Exploring sodium storage mechanism of topological insulator bi_2te_3 nanosheets encapsulated in conductive polymer,” *Energy Storage Materials*, vol. 41, pp. 255–263, 2021.
- [5] C. Beenakker, “Search for majorana fermions in superconductors,” *Annual Review of Condensed Matter Physics*, vol. 4, no. 1, pp. 113–136, 2013.
- [6] S.-M. Huang, S.-Y. Xu, I. Belopolski, C.-C. Lee, G. Chang, B. Wang, N. Alidoust, G. Bian, M. Neupane, C. Zhang, S. Jia, A. Bansil, H. Lin, and M. Z. Hasan, “A weyl fermion semimetal with surface fermi arcs in the transition metal monopnictide taas class,” *Nature Communications*, vol. 6, p. 7373, Jun 2015.
- [7] G. Bird, “Developing a robust material classification dataset for application to machine learning.” <https://github.com/GeorgeBird1/AcademicWork/blob/main/Masters%20Thesis%20Semester%201.pdf>, Nov 2022.
- [8] K. Ishizaka, M. S. Bahramy, H. Murakawa, M. Sakano, T. Shimojima, T. Sonobe, K. Koizumi, S. Shin, H. Miyahara, A. Kimura, K. Miyamoto, T. Okuda, H. Namatame, M. Taniguchi, R. Arita, N. Nagaosa, K. Kobayashi, Y. Murakami, R. Kumai, Y. Kaneko, Y. Onose, and Y. Tokura, “Giant rashba-type spin splitting in bulk btei,” *Nature Materials*, vol. 10, pp. 521–526, Jul 2011.
- [9] J. Vamathevan, D. Clark, P. Czodrowski, I. Dunham, E. Ferran, G. Lee, B. Li, A. Madabhushi, P. Shah, M. Spitzer, and S. Zhao, “Applications of machine learning in drug discovery and development,” *Nature Reviews Drug Discovery*, vol. 18, pp. 463–477, Jun 2019.
- [10] J. Carrasquilla and R. G. Melko, “Machine learning phases of matter,” *Nature Physics*, vol. 13, pp. 431–434, May 2017.
- [11] Y. Zhang and E.-A. Kim, “Quantum loop topography for machine learning,” *Physical Review Letters*, vol. 118, may 2017.
- [12] T. Konno, H. Kurokawa, F. Nabeshima, Y. Sakishita, R. Ogawa, I. Hosako, and A. Maeda, “Deep learning model for finding new superconductors,” *Physical Review B*, vol. 103, no. 1, p. 014509, 2021.
- [13] N. Sun, J. Yi, P. Zhang, H. Shen, and H. Zhai, “Deep learning topological invariants of band insulators,” *Physical Review B*, vol. 98, aug 2018.
- [14] J. F. Rodriguez-Nieva and M. S. Scheurer, “Identifying topological order through unsupervised machine learning,” *Nature Physics*, vol. 15, pp. 790–795, Aug 2019.
- [15] J. Ding, H.-K. Tang, and W. C. Yu, “Rapid detection of phase transitions from monte carlo samples before equilibrium,” *SciPost Physics*, vol. 13, sep 2022.
- [16] Y. LeCun and C. Cortes, “MNIST handwritten digit database,” 2010.
- [17] A. Krizhevsky, G. Hinton, *et al.*, “Learning multiple layers of features from tiny images,” 2009.
- [18] K. O’Shea and R. Nash, “An introduction to convolutional neural networks,” 2015.
- [19] A. Vaswani, N. Shazeer, N. Parmar, J. Uszkoreit, L. Jones, A. N. Gomez, L. Kaiser, and I. Polosukhin, “Attention is all you need,” 2017.
- [20] S. Murakami, “Phase transition between the quantum spin hall and insulator phases in 3d: emergence of a topological gapless phase,” *New Journal of Physics*, vol. 9, pp. 356–356, sep 2007.
- [21] S. Murakami and S. ichi Kuga, “Universal phase diagrams for the quantum spin hall systems,” *Physical Review B*, vol. 78, oct 2008.
- [22] X. Ying, “An overview of overfitting and its solutions,” in *Journal of physics: Conference series*, vol. 1168, p. 022022, IOP Publishing, 2019.

- [23] E. W. Weisstein, “n-torus.”
- [24] P. Hohenberg and W. Kohn, “Inhomogeneous electron gas,” *Phys. Rev.*, vol. 136, pp. B864–B871, Nov 1964.
- [25] T. Mikolov *et al.*, “Statistical language models based on neural networks,” *Presentation at Google, Mountain View, 2nd April*, vol. 80, no. 26, 2012.
- [26] G. Bird, “Bird’s convention for diagrammatic neural networks.” <https://github.com/GeorgeBird1/Diagrammatic-Neural-Networks>, Nov 2022.
- [27] R. E. Bellman, *Dynamic programming*. Princeton university press, 2010.
- [28] K. Koutroumbas and S. Theodoridis, *Pattern recognition*. Academic Press, 2008.
- [29] D. Harris and S. L. Harris, *Digital design and computer architecture*. Morgan Kaufmann, 2010.
- [30] K. He, X. Zhang, S. Ren, and J. Sun, “Deep residual learning for image recognition,” 2015.
- [31] J. Li and D. Liu, “Information bottleneck theory on convolutional neural networks,” 2021.
- [32] A. Einstein, “The Foundation of the General Theory of Relativity,” *Annalen Phys.*, vol. 49, no. 7, pp. 769–822, 1916.
- [33] A. Odena, V. Dumoulin, and C. Olah, “Deconvolution and checkerboard artifacts,” *Distill*, 2016.
- [34] H. Gholamalinezhad and H. Khosravi, “Pooling methods in deep neural networks, a review,” 2020.
- [35] Y. Bengio, P. Simard, and P. Frasconi, “Learning long-term dependencies with gradient descent is difficult,” *IEEE transactions on neural networks / a publication of the IEEE Neural Networks Council*, vol. 5, pp. 157–66, 02 1994.
- [36] R. Pascanu, T. Mikolov, and Y. Bengio, “On the difficulty of training recurrent neural networks,” 2013.
- [37] A. L. Maas, A. Y. Hannun, A. Y. Ng, *et al.*, “Rectifier nonlinearities improve neural network acoustic models,” in *Proc. icml*, vol. 30, p. 3, Atlanta, Georgia, USA, 2013.
- [38] S. Ioffe and C. Szegedy, “Batch normalization: Accelerating deep network training by reducing internal covariate shift,” 2015.
- [39] “Pytorch implementation of tensor rolling.” <https://pytorch.org/docs/stable/generated/torch.roll.html>.
- [40] J. Wang, S. Valligatla, Y. Yin, L. Schwarz, M. Medina-Sánchez, S. Baunack, C. H. Lee, R. Thomale, S. Li, V. M. Fomin, L. Ma, and O. G. Schmidt, “Experimental observation of berry phases in optical möbius-strip microcavities,” *Nature Photonics*, vol. 17, pp. 120–125, Jan 2023.
- [41] G. Liu, M. Pi, L. Zhou, Z. Liu, X. Shen, X. Ye, S. Qin, X. Mi, X. Chen, L. Zhao, B. Zhou, J. Guo, X. Yu, Y. Chai, H. Weng, and Y. Long, “Physical realization of topological roman surface by spin-induced ferroelectric polarization in cubic lattice,” *Nature Communications*, vol. 13, p. 2373, May 2022.
- [42] M. V. Berry, “Quantal phase factors accompanying adiabatic changes,” *Proceedings of the Royal Society of London. A. Mathematical and Physical Sciences*, vol. 392, no. 1802, pp. 45–57, 1984.
- [43] S. Pancharatnam, “Generalized theory of interference, and its applications,” *Proceedings of the Indian Academy of Sciences - Section A*, vol. 44, pp. 247–262, Nov 1956.
- [44] A. Zhang, Z. C. Lipton, M. Li, and A. J. Smola, “8.6 residual networks - dive into deep learning,” *arXiv preprint arXiv:2106.11342*, 2021.
- [45] G. Huang, Z. Liu, and K. Q. Weinberger, “Densely connected convolutional networks,” *CoRR*, vol. abs/1608.06993, 2016.
- [46] C. Szegedy, W. Liu, Y. Jia, P. Sermanet, S. Reed, D. Anguelov, D. Erhan, V. Vanhoucke, and A. Rabinovich, “Going deeper with convolutions,” 2014.
- [47] M. Lin, Q. Chen, and S. Yan, “Network in network,” 2014.
- [48] S. Hochreiter and J. Schmidhuber, “Long short-term memory,” *Neural Comput.*, vol. 9, p. 1735–1780, nov 1997.
- [49] J. Han and C. Moraga, “The influence of the sigmoid function parameters on the speed of backpropagation learning,” in *Proceedings of the International Workshop on Artificial Neural Networks: From Natural to Artificial Neural Computation, IWANN ’96*, (Berlin, Heidelberg), p. 195–201, Springer-Verlag, 1995.

- [50] J. S. Bridle, “Probabilistic interpretation of feedforward classification network outputs, with relationships to statistical pattern recognition,” in *Neurocomputing: Algorithms, architectures and applications*, pp. 227–236, Springer, 1990.
- [51] V. Klema and A. Laub, “The singular value decomposition: Its computation and some applications,” *IEEE Transactions on automatic control*, vol. 25, no. 2, pp. 164–176, 1980.
- [52] G. E. Hinton and S. Roweis, “Stochastic neighbor embedding,” *Advances in neural information processing systems*, vol. 15, 2002.
- [53] L. van der Maaten and G. Hinton, “Visualizing data using t-sne,” *Journal of Machine Learning Research*, vol. 9, no. 86, pp. 2579–2605, 2008.
- [54] D. Ballard, “Modular learning in neural networks,” 1987.
- [55] I. J. Good, “Rational decisions,” *Journal of the Royal Statistical Society: Series B (Methodological)*, vol. 14, no. 1, pp. 107–114, 1952.
- [56] “Pytorch’s implementation of conv2d.” <https://pytorch.org/docs/stable/generated/torch.nn.Conv2d.html>.

Appendices

A Neural Architectures

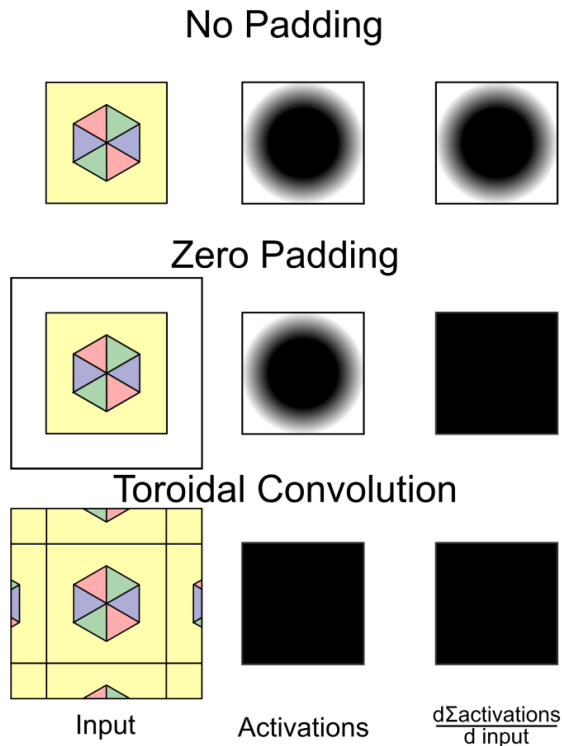


Figure 23: This figure shows how no-padding in convolution results in edge effects for both the activations and the differential between the sum of the activations with respect to the input, thus disrupting equivariance. Zero-padding alleviates the latter, by ensuring that all input elements contribute evenly to the sum of the activations, resulting in an equivariant backpropagation step. Toroidal convolution fixes both problems, with no edge effects in either the activations or the derivative of the sum of the activations. Therefore, toroidal convolution has a full global equivariance. The darkness of the activations indicates the expected generalised magnitude of activations. The darkness of the derivative column indicates the general contribution of each input pixel to the sum of the activations.

B BiTeI Dataset

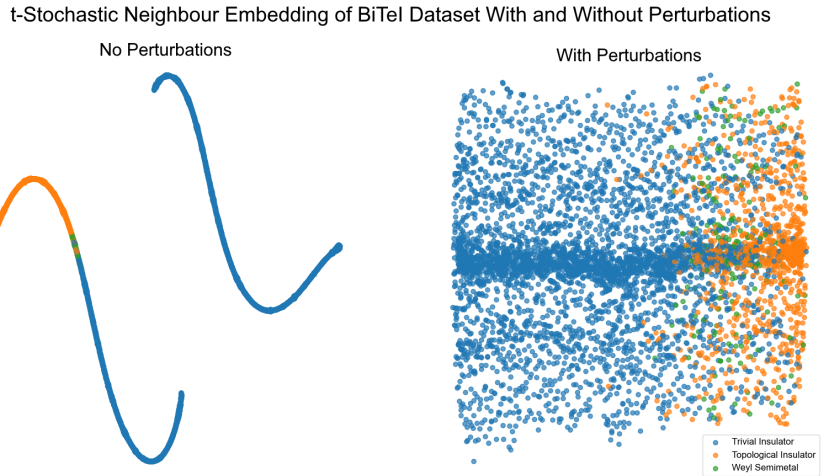


Figure 24: Shows a t-stochastic neighbour embedding of Hamiltonian samples in the unperturbed (left) and perturbed (right) datasets. The curved shape and discontinuity of the line in the left image are a result of the embedding algorithm. It can be seen that the unperturbed dataset is an embedding of a one-dimensional manifold, whereas the perturbed dataset demarcates a high-dimensional manifold's volume. The colour of the sample indicates the crystalline state.

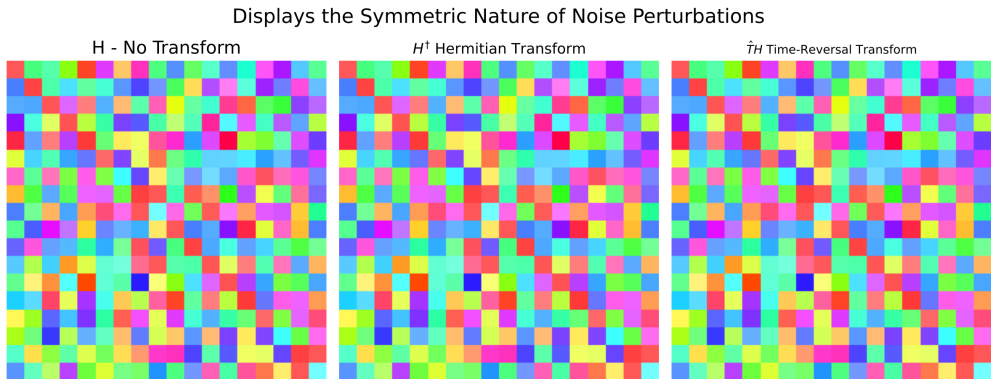


Figure 25: Shows the hopping perturbations for $\vec{A} = \vec{0}$, where the colour indicates the complex argument and the opacity indicates the absolute value. It can be seen that the hoppings are unchanged under the hermitian and time-reversal symmetry as desired. This has also been confirmed for all values of \vec{A} .

C MNIST

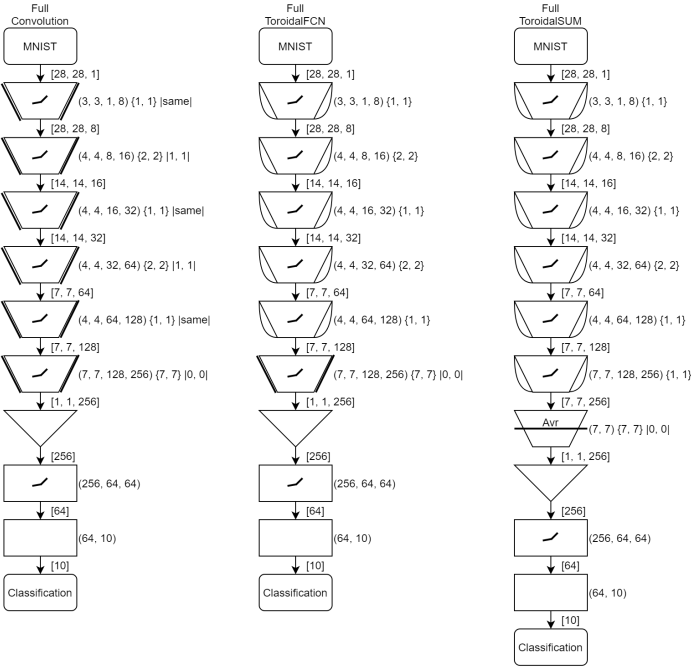


Figure 26: Shows the architectures for the "Full Convolution" (left), "Full Toroidal FCN" (middle) and "Full ToroidalSUM" (right). The Toroidal FCN network has an invariance-breaking final convolutional layer. All networks have equal numbers of parameters. |same| indicates the "SAME" padding [56].

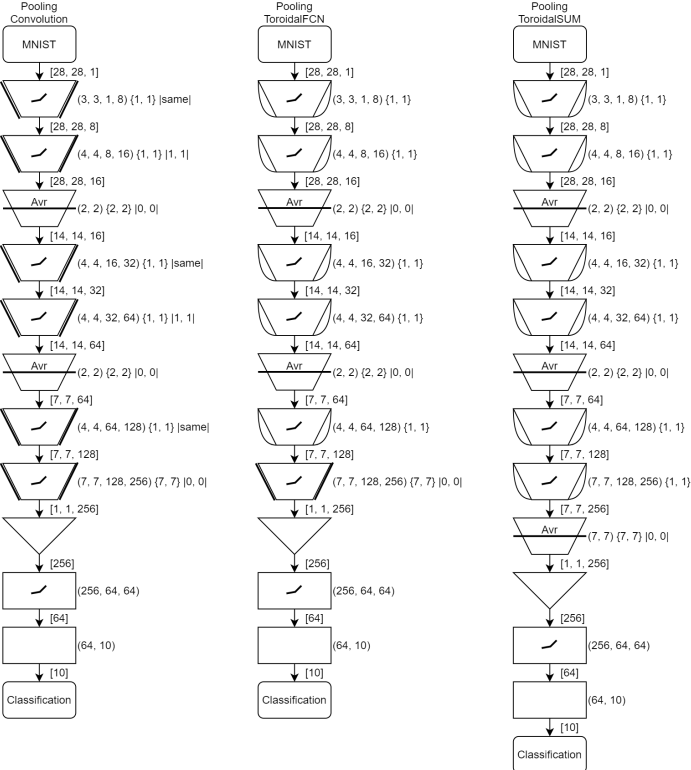


Figure 27: Shows the architectures for the "Pooling Convolution" (left), "Pooling Toroidal FCN" (middle) and "Pooling ToroidalSUM" (right).

D CIFAR10

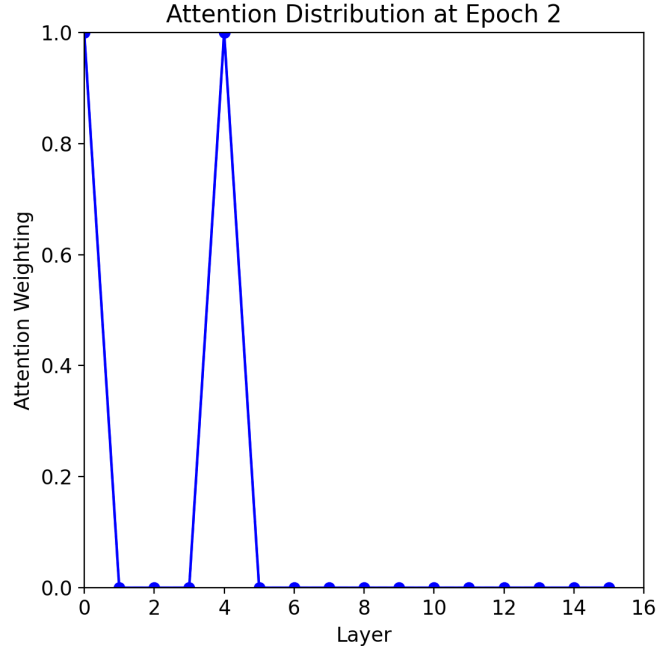


Figure 28: This figure indicates the attention distribution at epoch=2 for a network exhibiting unstable behaviour. This attention distribution shows a saturation on layers zero and four, with no dynamic behaviour between samples shown by the standard deviation of zero. This indicates that the network is unaware of the value of other layers since they are damped to zero. This in turn limits the performance. This attention distribution was found to remain constant across all future epochs.

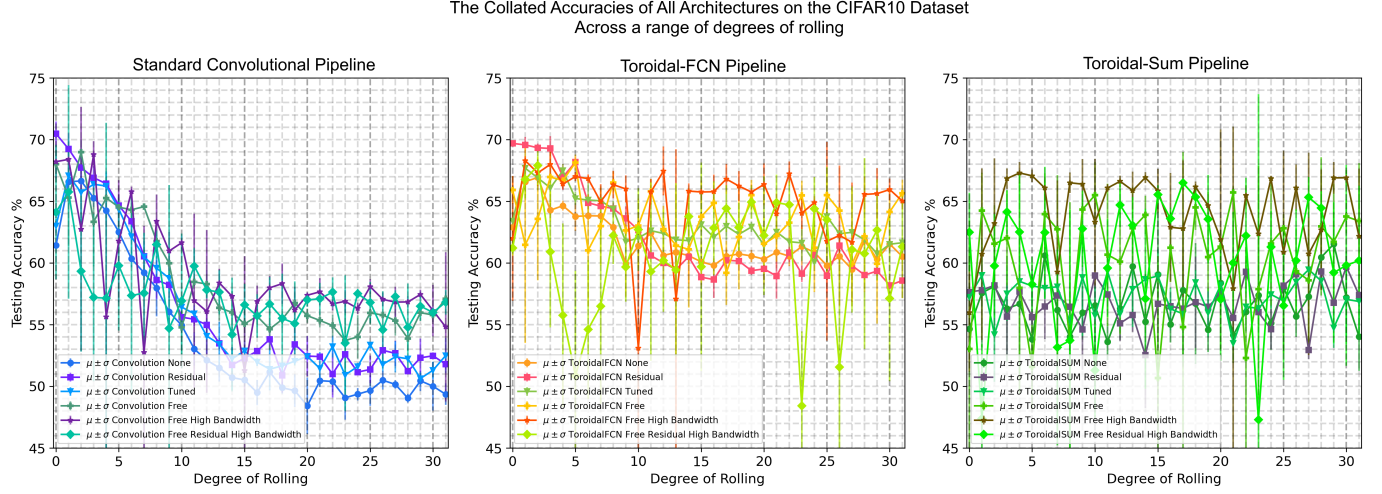


Figure 29: Shows the combined accuracies, on CIFAR10, of all tested networks against the degree-of-rolling χ , with results separated into columns of the particular pipeline architectures. Standard convolution is shown (left), Toroidal-FCN (centre) and Toroidal-Sum (right).